Search for lepton flavour violating $H \to \mu\tau$ Higgs decays at 13 TeV

Master's thesis in experimental particle physics

Simen Hellesund

Institute of Physics and Technology
University of Bergen

Supervised by
Professor Bjarne Stugu

June 1, 2016

Contents

List of Figures

List of Tables

Acknowledgements

First of all I would like to thank my supervisor, professor Bjarne Stugu, for giving me the opportunity to work on such an interesting and challenging project. I am deeply grateful for the guidance and support you have given me throughout the project, and for giving me the opportunity to work at CERN on multiple occasions.

A special thanks to Steffen Mæland. Your patience for stupid questions and willingness to help really is unparalleled. Without your encyclopedic technical knowledge I would surely not have been able to finish the project in time. I owe you a Volvic Juicy.

For providing technical assistance and proof reading I would like to acknowledge Professor Jörn Kersten, professor Anna Lipniacka, Bertrand Martin dit Latour and Inga Strümke.

I want to thank my family, Wenche, Kjell Rune, and Vegar, for their support, both emotional and fiscal.

Although maybe not directly involved in my thesis, my fellow particle physics master's students at the University of Bergen (UiB), Andreas, Are, Hans, Håkon, Magne, Martin, Nick and Lars, have made the last two years of my life much more enjoyable. I have greatly enjoyed our lively discussions and ludological pursuits.

To anyone I forget mentioning here, I sincerely apologise. Hopefully you know who you are. Any faults and errors are entirely my own.

Lastly I want to thank elevators, for bringing me up when I was down.

1 Introduction

The aim of this thesis is to explain some of the methods and tools used in experimental high energy particle physics, with emphasis on statistical analysis, as well as to describe some of the theoretical foundation of this field of study.

The Standard Model (SM) of particle physics has been wildly successful at explaining elemental particles and their interactions. However, phenomena like dark matter and baryon-asymmetry suggest that the SM is only an effective theory, valid only at certain energy scales. The SM is covered in chapter 3.

The Large Hadron Collider (LHC) at Conseil Européen pour la Recherche Nucléaire (CERN) is a 27 km circular particle accelerator, buried 100 meter underground on the France-Switzerland border outside Geneva. In it, protons and heavy ions are accelerated to extremely high energies, before colliding in one of four experiments. One of these experiments is the ATLAS detector. ATLAS works like a large camera focused on the collision point of the LHC beams. It records information about the stream of secondary particles streaming out from the interactions taking place there. Interesting physics events are separated from less interesting ones using hardware and software triggers. The data recorded is then analysed by physicists. Analyses being performed can be precision measurements, calibration of instruments, or searches for physics Beyond Standard Model (BSM). The ATLAS detector and its main components are described in chapter 2.

In 2012, the ATLAS and CMS collaborations both claimed discovery of a previously seen elementary particle, the Higgs boson[1], named after one of the physicists postulating its existence. The Higgs boson, often referred to simply as the Higgs, offers an interesting channel for BSM searches.

A Lepton Flavour Violation (LFV) process is one in which the lepton family number $L_i \, (i = e, \mu, \tau)$ is not conserved in the final state. Charged LFV is strongly suppressed in the SM. Observing a non-zero branching ratio for a Higgs LFV process would therefore be unequivocal proof of BSM physics. The branching ratio of the process $H \to \mu\tau$ is presently the least constrained of any Higgs LFV processes. The analysis in chapter 9 aims to put a limit on the expected $H \to \mu\tau$ branching ratio in data taken in 2015 using the ATLAS detector. The total integrated luminosity recorded in this period is roughly 3 fb^{-1}.

[1] Some theories postulate that the Higgs is not elementary, but rather a bound system. This is discussed briefly in chapter 4.

The detection of tau leptons in ATLAS is nontrivial. Due to their short lifetime, taus must be inferred from their decay products. Tau reconstruction and identification in ATLAS is covered by chapter 6. The presence of taus in the Higgs decay also complicates the mass reconstruction of the Higgs itself. Part of the energy in the decay is carried away by a neutrino. Neutrinos are too weakly interacting to leave a signature in the detector. All is not lost however. Summing over the transverse momenta of the decay products should yield zero, since there is no transverse momentum in the initial state protons colliding. This can be used to calculate the so-called missing transverse energy E_T^{miss}, which is assumed to be due to the neutrino.

In this thesis a novel method of mass reconstruction is explored for use in LFV searches: The Boost Method. The method exploits the fact that for a sufficiently massive particle decaying into a tau, say a Z boson or a Higgs, the direction of the visible and invisible tau decay products are assumed to be close to parallel. The CM of a Higgs or Z decaying into two leptons is found by performing a Lorentz boost such that the two leptons products are as close to back-to-back as possible. This procedure is explained in chapter 7. The method is studied in chapter 8 using a sample of simulated Z bosons decaying into a tau and a muon in the ATLAS detector at $\sqrt{s} = 13$ TeV.

2 The Experiment

2.1 CERN

The idea of a European cooperation for nuclear research was put forth in 1949 by French physicist Louis de Broglie. The European Council for Nuclear Research, CERN in French, was formed in 1952, tasked with establishing such an organization. The organization was founded by 12 member states in 1954 [1]. Although the provisional council was disbanded, the CERN acronym remained. In 2014, CERN had grown to include 21 member states, employing approximately 2500 staff as well as 13000 external users [2]. Scientists from all over the world, not just Europe, do their research at the many experiments at CERN.

The CERN laboratory is located in Meyrin, on the outskirts of Geneva, on the border between Switzerland and France. It is the largest particle physics laboratory in the world. The first particle accelerator built on the site was the 600 MeV Synchrocyclotron (SC) in 1957 followed by the 28 GeV Proton Synchrotron (PS) in 1959. The PS is still in use today, supplying particles to experiments or higher energy accelerators. The Super Proton Synchrotron (SPS) was completed in 1976, two years ahead of schedule. It has a circumference of almost seven kilometres, and reaches energies of up to 450 GeV. Like the PS, the SPS is still in use today. The 27 kilometre tunnel, roughly 100 meters under ground, excavated to make room for the Large Electron-Positron Collider (LEP), was at the time the largest European civil-engineering project ever undertaken. LEP became operational in 1989, colliding electrons and positrons at 100 GeV. The accelerator was later upgraded to reach energies of over 200 GeV. It still remains the largest e^+e^- accelerator ever constructed. LEP stayed in use for 11 years until 2000, when it was closed down to make room for the LHC in the same tunnel.

Since the founding of the organization, the accelerators and experiments at CERN has been used to make great advances in science. The first observation of antinuclei was made here in 1965 [3]. Antideuterons, which consists of one antineutron and one antiproton each, was produced in collisions between protons and beryllium ions using the PS. The first antiatoms were also observed at CERN, when a team led by Walter Oelert successfully created antihydrogen in 1995 [4]. Today, experiments at CERN like the ALPHA (Antihydrogen Laser Physics Apparatus) or AEGIS (Antimatter Experiment: Gravity, Interferometry, Spectroscopy)

are tasked with measuring the properties of antimatter. The SM specifies a lot of these properties, but unless we make an experiment to actually test that this is true, we can never be completely sure about the validity of our models. The study of antimatter is also important because it might hint as to why ordinary matter is so much more abundant in the universe than anti-matter.

In 1983 the Z and W bosons of the weak force were discovered in the UA1 and UA2 experiments at the SPS. Crucial to this discovery was the conversion of the SPS from a proton-proton collider to a proton-antiproton collider. Carlo Rubbia and Simon van der Meer received the Nobel Prize in physics for their work on the project [5].

As far as advances in technology goes, the biggest invention to come out of CERN is probably the World Wide Web (WWW). The Web was invented at CERN in 1989 by Tim Berners-Lee, and the worlds first website saw the light of day in 1990.

2.2 LHC

Two important quantities in High Energy Particle Physics (HEPP) experiments are *luminosity* $\mathcal{L}$ and *cross section* σ. Cross section is a measure of the probability of a process taking place. Take this example: A football is being kicked towards the goal. For a scoring to take place, the ball needs to hit within the area subtended by the goalposts. In the quantum world of elementary particles, this classical picture is a bit too simple, the cross section is not simply the area extended by the particle, but the principle remains. A¡ common unit for cross section is the *barn* b[1]. 1 b = 10^{-24} cm^2 = 100 fm^2.

Luminosity $\mathcal{L}$, often referred to as instantaneous luminosity, is the proportionality factor between the rate of collisions, also known as events, and the cross section:

$$\dot{N} = \mathcal{L}\sigma \tag{2.1}$$

The unit of luminosity is cm^{-2}s^{-1}. Luminosity is defined as the of events per unit cross section that take place in a single beam encounter region per unit time. take as an example a collider experiment where two bunches of particles are colliding head on, one containing N_1 particles, and the other containing N_2 particles. the bunches collide with frequency f and are both uniform over an area A. The

[1]The name barn is supposed to stem from the idiom "could not hit the broad side of a barn", and was first used amongst scientists colliding neutrons off of uranium nuclei. The joke being that the area of a uranium nuclei is a very big unit in the world of subatomic particles [6].

luminosity is then given by

$$\mathcal{L} = \frac{N_1 N_2 f}{A} \tag{2.2}$$

The picture becomes a bit more complicated in the LHC, where we have a multitude of bunches in each beam. Moreover, the beams in the LHC are not colliding head on, but rather at an angle. The distribution of protons within each bunch must also be taken into account. If each beam contains N_b bunches of particles and each bunch is Gaussian in all directions then equation 2.2 transforms into

$$\mathcal{L} = \frac{N_b N_1 N_2 f}{4\pi\sigma_x\sigma_y} S \tag{2.3}$$

where the factor S takes into account the crossing angle. σ_x and σ_y are the width of the beam density distributions in the directions transverse to the beam direction. This is still a very simplified way of calculating the luminosity. The beams might be non-Gaussian for example, or the collision might be offset from each other.

If instantaneous luminosity is integrated over the running time of the experiment in question, one obtains the *integrated luminosity*. It has dimensions of inverse area, often expressed in inverse barns. The integrated luminosity is an important measure of the performance of the detector.

Installed in the tunnel excavated for LEP, the LHC, with its 27 km circumference, is the worlds largest particle accelerator. It is a synchrotron storage ring, colliding proton or heavy ion(Lead) beams at four points along the accelerator ring. A synchrotron is a descendant of the cyclotron, invented in 1932 by Ernest Lawrence. The magnetic fields bending the beam and the radiofrequency (RF) cavities responsible for accelerating the beam are both *synchronised* to the revolution frequency of the beam. A storage ring is a type of synchrotron in which the beam energy is maintained at a constant level for extended periods of time. The LHC has a design luminosity of 10^{34} $\text{cm}^{-2}\text{s}^{-1}$. The two beams consist of 2808 bunches were each bunch consists of 1.15×10^{11} particles.

One might ask why two beams are collided head on instead of one beam impinging on a stationary target. This would increase the number of collisions. The reason for this is to be able to reach higher energies released in the collisions. The CM energy[2] in a collision of two beams of energy E is $2E$, while the same energy if one of said beams hit a stationary target of mass m is $\sqrt{2Em}$. A doubling of the beam energy will multiply the collision energy by four in a colliding beam experiment, whilst only multiplying the collision energy by $\sqrt{2}$ in the fixed beam

[2]The c.m. frame of a system is the frame in which the sum of all momenta is equal to zero. The motion of the whole system is irrelevant. it is only the energy of the particle with regards to each other that matters. The c.m. energies and momenta are therefore important.

experiment. A 1 TeV fixed target beam is equivalent of two 21.6 GeV beams colliding head on [7]. The reason for wanting to reach these high energies is simply to be able to create more massive particles in the collisions. Einstein taught the world the famous relationship between mass and energy:

$$E^2 = (mc^2)^2 + (pc)^2 \tag{2.4}$$

This simply means that by increasing the energy of the beams, more massive particles can be produced in the collisions.

The protons and ions in the LHC radiate photons due to being constantly accelerated towards the center of the accelerator. This is know as *synchrotron radiation*. The energy lost to synchrotron radiation can be approximated by the following equation:

$$-\Delta E = PT \approx \frac{4\pi e^2}{3R}\left(\frac{E}{mc^2}\right)^4 \tag{2.5}$$

R is the radius of the accelerator in question. Notice the high exponent. This means that for a light particle the synchrotron radiation will increase rapidly as the energy increases. Calculating the rate of energy loss of electrons and protons:

$$\frac{-\Delta E_e}{-\Delta E_p} \approx \left(\frac{m_p}{m_e}\right)^4 \approx 10^{13} \tag{2.6}$$

Energy lost by synchrotron radiation is limiting the energy that can be achieved in e^+e^--accelerators. At some point the energy lost to radiation is equal to the energy put into acceleration. This is why the LHC can reach much higher energies than LEP ever could, despite both accelerators having the same radius.

The LHC is the first proton accelerator where synchrotron radiation actually poses a challenge. This is not the limiting factor to the accelerator's beam energy however. The maximum obtainable energy is given by the strength of the magnets bending the beam. The beam is bent by 1232 superconducting dipole magnets cooled to 2K using a liquid helium system. The dipoles produce an 8.4 T magnetic field. Simply bending the beams is not enough though, they must also be focused. The protons or ions in the beam bunches are all positively charged, and will thus be repelling each other, defocusing the beam. The beam bending in a dipole field is analogous to a photon beam bending in a glass prism. To focus the proton beam we thus need a magnetic lens with properties analogous to that of an optical focusing lens. Sadly, no such analogue exist. Focusing, or *collimation*, is still achieved though, through a phenomenon called *strong focusing*. If focusing and defocusing lenses of equal focal lengths are alternated, a net focusing effect occurs [7]. In the LHC this is done using quadrupole magnets. A quadrupole is focusing in one plane and defocusing in the perpendicular plane. This can be seen in fig

2.1. If we imagine the beam going into the paper, protons situated along the x-axis will be pushed outward from the origin, while those along the y-axis will be pulled in. If two such magnets are placed one after the other in the accelerator, rotated 90°from one another, the beam will be focused. When the beams reach the interaction points they are "squeezed" further using higher order pole magnets. This is done to increase the luminosity. One might wonder why the LHC doesn't collide protons and antiprotons, like the SPS did in the eighties or the Tevatron in the United States. If this was the case the beams could be contained in a single beam pipe, and use one dipole field to bend the two beams. In the LHC we need separate fields for each beam. Antiprotons are more difficult to produce than protons however. The high design luminosity of the LHC excludes the use of antiprotons [8]. Having a single beam pipe would also exclude the possibility of colliding heavy ions.

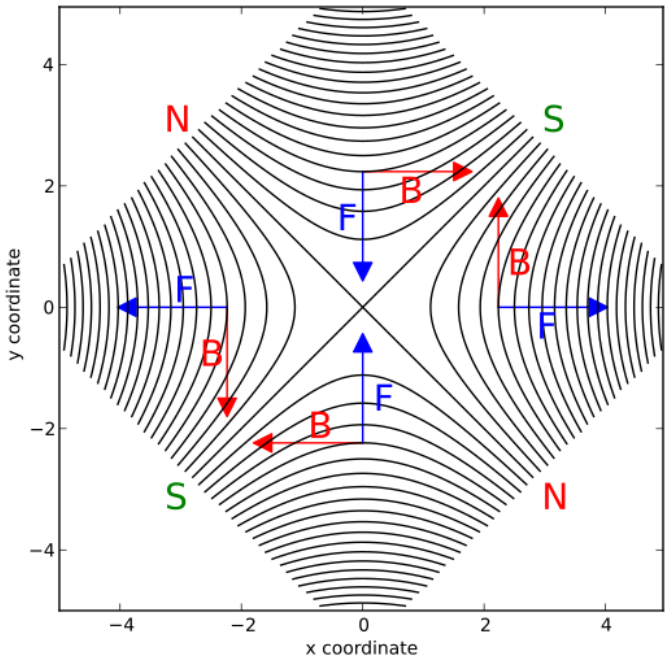

Figure 2.1: Idealized quadrupole [9]

.

The LHC is not able to accelerate protons from rest. The range in energy required from both the RF cavities and the bending magnets would be too great to handle. Instead, a range of accelerators are used at different stages to accelerate

the protons and heavy ions before injection into the LHC ring itself. Figure 2.2 shows the complete acceleration complex required to get beams into the LHC. Following is an explanation of the steps taken to accelerate protons before they are injected into the LHC: The injection chain starts with an unassuming cannister of hydrogen gas. The electrons are stripped off the protons before entering the first stage, the linear accelerator LINAC2. Here the protons are accelerated to 50 MeV before entering the second stage, the Proton Synchrotron Booster (PSB). The PSB consists of four synchrotron rings, stacked on top of each other. It is split up this way to increase the proton density before the next stage. After being accelerated to 1.6 GeV, the protons then enter the PS, mentioned earlier. Here the protons gain even more energy, up to 25 GeV, before entering the SPS. This is the final stage of the acceleration before injection into the main accelerator. The energy of the protons when they enter the LHC is 450 GeV. Up until this point the protons have all been travelling in the same direction, in one single beam pipe. Before entering the LHC this beam is split into two, one going clockwise and the other anticlockwise.

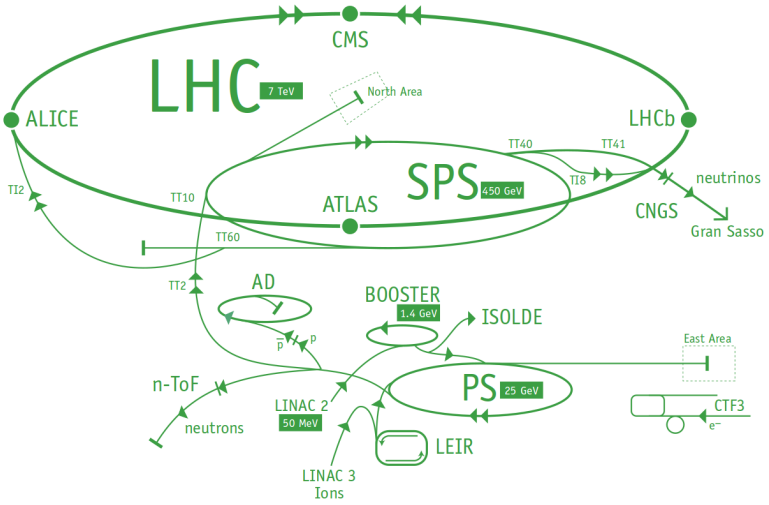

Figure 2.2: The LHC injection chain [10].

The actual acceleration of the beams in the LHC is not continuous around the ring, but happens at one point along the ring in RF cavities. The RF cavities are metallic chambers where standing electromagnetic waves are tuned to just the right frequency so as to give the beam a "push" each time it passes by, which is thousands of times a second. The fact that the same acceleration module can be used over and over to accelerate the same particles is one of the main advantages of a circular accelerator. In a linear accelerator (LINAC) the particles only pass through the accelerator once. The LHC has 16 RF cavities, housed in four cryogenic modules,

two per beam. Like the magnets, the RF cavities are working in a superconducting state. Klystrons are used to drive the cavities. A klystron is a type of electron drift tube used to amplify radio frequency signals.

The LHC started up in September 2008 but suffered a breakdown just nine days after becoming operational. A faulty connection between two magnets caused an electrical arc to develop. This arc punctured a hole in a pipe carrying liquid helium, causing a leak. This damaged a number of magnets that had to be replaced, while some had to be serviced. Steps were taken to prevent the problem from recurring and the machine was up and running again in November 2009.

The four main experiments of the LHC are: A Toroidal LHC AparatuS (ATLAS), Compact Muon Solenoid (CMS), LHCb and A Large Ion Collider Experiment (ALICE). ATLAS and CMS are multi purpose detectors. So called "discovery machines". There are two such detectors, so that they can independently verify each others results. LHCb is focused on studying CP-violation and b-physics. ALICE is dedicated to heavy ion experiments.

2.3 The ATLAS Detector

The ATLAS detector, pictured in figure 2.3, is the largest of the four main LHC experiments. Shaped like a cylinder, it is 46 meters long and its diameter is 25 meters. It weighs approximately 7000 tons[3].

The ATLAS detector is divided into subdetectors. These subdetectors are situated in layers not unlike the layers in an onion. The various layers are made for specific tasks, such as measuring the position, momentum or energy of the particles passing through them. It is important to layer the subdetectors in order of decreasing *transmissibility*, so that we minimize the number of particles interacting with the detector before it has a chance to be measured properly. The construction follows the same recipe as countless other experiments, including the other LHC detectors: Tracking detectors in an magnetic field closest to the collision point. The trackers locates the precise point of the proton collisions, as well as any potential secondary vertices, where short-lived particles, such as tau leptons, decay. The magnetic field will deflect charged particles travelling through the detector. The amount of deflection is proportional to the momentum of the particle. Measuring the path of the particle through the magnetic field thus allows us to measure its momentum. This innermost part of the detector in ATLAS is called the Inner Detector (ID). After the ID comes the *calorimeters*, dedicated to energy

[3]This might seem like a lot, but the ATLAS detector is not very dense at all. In fact, if you were able to seal it up and throw it into lake Geneva, it would float. CMS, despite being a smaller detector, weighs almost twice as much as ATLAS. This is due to very different systems designs for muon identification

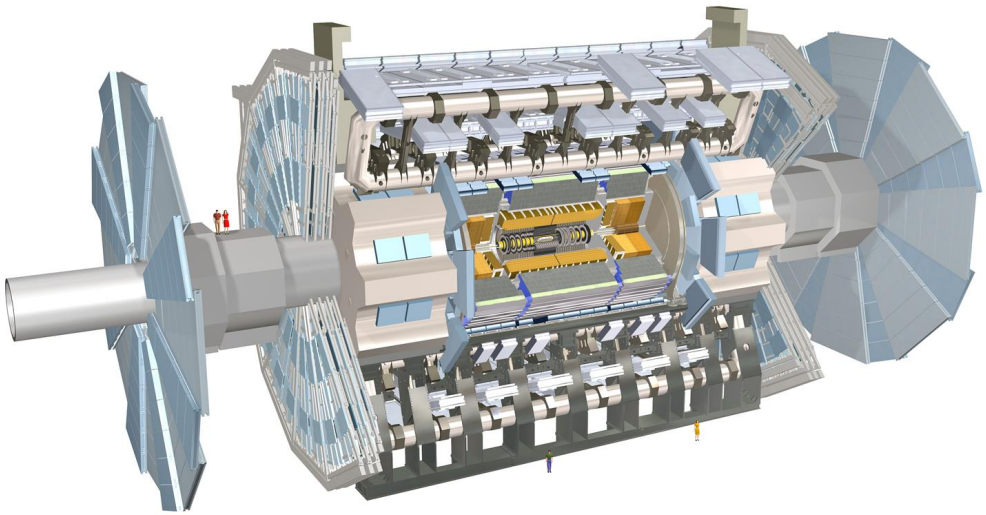

Figure 2.3: The ATLAS detector. Parts of the detector have been removed to give a view of the inner detector. Notice the tiny humans for scale [11].

measurements. These work by absorbing, or slowing down, incoming particles while measuring the amount of energy being deposited by the incoming particle in the process. The muon detectors are located on the outside of the calorimeters. Muons have a long lifetime compared to other unstable elementary particles. It is also much heavier than the electron, which means that it loses much less energy to bremsstrahlung. This, along with the fact that it doesn't interact hadronically, means that muons can penetrate a lot more material than most elementary particles. This is the reason for placing the muon detectors on the outside of the other subdetectors. Most of the particles that make it this far away from the collisions should be muons. A second magnetic field, although with a different configuration than that of the SC, allows for more momentum measurements. Following are details about the various subdetector systems in the ATLAS detector.

2.3.1 ATLAS Coordinates

The origin of the ATLAS coordinate system lies in the interaction point. The z-direction is parallel to the beam pipe, the x-axis is pointing towards the center of the LHC ring, while the y-axis is pointing upwards. The transverse plane is the

x-y plane. This plane is important because prior to any collisions, the protons in the beams have no energy or momentum in this plane. Variables with a subscript T, like p_T are measured in the transverse plane. using polar coordinates, the polar angle θ is defined as the angle from the beam pipe, while the azimuthal angle ϕ is defined in the transverse plane. Rather than using θ, the angle from the beam pipe is often described by the *pseudorapidity* η. It is defined as:

$$\eta = -\ln\left[\tan\left(\frac{\theta}{2}\right)\right] \tag{2.7}$$

Pseudorapidity is zero in the transverse plane and goes to infinity along the beam pipe (figure 2.4). Pseudorapidity is useful, because differences in pseudorapidity is invariant under Lorentz boosts along the beam pipe. It is especially important in proton-proton experiments, because the particle production as a function of η is roughly constant. To ensure that no particles escapes undetected, it is important to have coverage of a big range in η. The η coverage of the various subdetectors are listed in table 2.1. For heavy objects like jets, the rapidity is also used:

$$y = -\frac{1}{2}\ln\left[\frac{E + p_z}{E - p_z}\right] \tag{2.8}$$

Pseudorapidity is equal to rapidity if the mass of the object in question is negligible. This is usually the case at the high energies of the LHC.

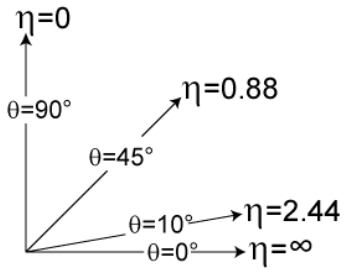

Figure 2.4: Pseudorapidity compared to θ [12].

To define the angular separation of two objects in the detector, the value ΔR is often used. It is defined as:

$$\Delta R = \sqrt{(\phi_1 - \phi_2)^2 + (\eta_1 - \eta_2)^2} \tag{2.9}$$

2.3.2 Inner Detector

The ID is housed in a cylindrical cavity, 7 meters long and with an outer radius of 1.15 meter, located in the center of the detector. It consists of three separate systems: The pixel detector, Semiconductor Tracker (SCT) and Transition Radiation

Tracker (TRT). A 2 T solenoidal magnetic field provides the bending of charged particles.

The pixel detectors are located closest to the interaction point. It consists of three layers around the beam with an additional three disks on either side. The closest pixels are located 4 cm from the colliding protons. The pixels give very precise position measurements, which is important for locating vertices. However, they also have some drawbacks: They are very expensive. They provide a limited number of measurement points per track, and put a relatively large amount of material in front of the incident particles. This is unfortunate, seeing as we want to keep the transmissibility high in this part of the detector. The proximity to the collisions also means that the pixels need to be very radiation hard. The total number of pixels is over 80 million.

The SCT is located after the pixels. It consists of four double layers of silicon microstrip detectors in cylindrical layers around the interaction point as well as 18 additional end cap disks. In each of the layers one of the strips is mounted along the beam pipe while the other is rotated 40 mrad. This provides two-dimensional information about the hit. The reason this angle is so small is to minimise the amount of fake hits in the detectors. If the strips were to be placed perpendicular to one another, n tracks would simulate n^2 hits in the reconstruction of the tracks. Placing the strips at a small angle, a method called *small-angle stereo*, reduces the number of strips overlapping, thus reducing the amount of "ghosts" in the detector [13]. The pixel detectors also play an important role in removing these fake hits in the detector, seeing as they output three dimensional hit coordinates. in total there are 61 m^2 of microstrip detectors in the SCT, with 6.2 million readout channels. In comparison, the pixel detector covers less than three meters, and has over 80 million readout channels. The microstrip and pixel detectors are both semiconductor detectors. Absorbed energy in the detectors form electron-hole pairs, which are then collected on electrodes and read out. The energy required to form such electron-hole pairs is proportional to the band gap [13].

The TRT is not as precise as the semiconductor detectors, but offers more tracking points with less material per point. It consists of many gas filled drift tube detectors called straws, mounted in parallel. The straws are 4 mm in diameter and are filled with a mixture of Xenon, CO_2 and O_2. The TRT consists of 50.000 straw in the barrel, mounted parallel to the beam pipe, as well as 320.000 straws mounted radially in the end caps. The placement of the straws in the barrel means that we cannot measure η, only the transverse position of the track. However, this is all we need to measure the transverse momentum p_T. The straw tubes work by measuring ionization. A 30 μm wire is stretched through each straw, and sets up a radial electric field inside it. When a particle passes through the straw it ionizes the Xenon gas. The liberated electrons drift towards the wire along the

electric field and creates an electric signal which can be read out at the end of the straw. The TRT registers an average of 36 hits per particle traversing the ID. In between the layers of straws there are radiators which produce transition radiation. Transition radiation can be produced when a charged particle traverse a boundary between materials with different dielectric properties. The emittance of photons is a threshold effect dependant on the relativistic velocity p/m. The presence of transition photons can thus be used for particle identification. In the TRT this is used to separate electrons from hadrons.

The complete set-up of the ID can be seen in figure 2.5. The radial placement of the various detector components can also be seen. The relative precision of the different measurement methods in the ID is similar for the three parts of the ID. This way one method doesn't dominate the overall resolution.

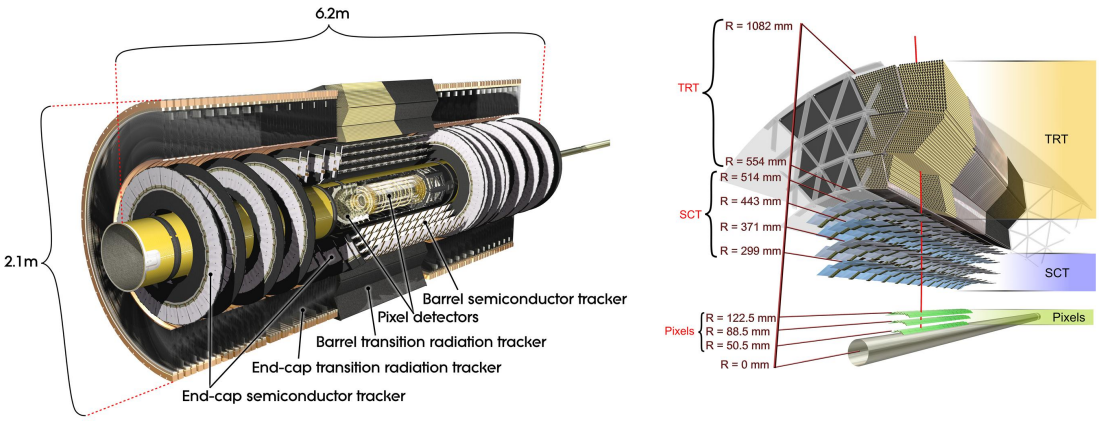

(a) The Complete ID

(b) Cross section of the ID

Figure 2.5: The ATLAS Inner Detector [14]

2.3.3 Calorimeters

Calorimeters are mainly tasked with measuring the energy of particles, but also provide position measurements and particle identification. Energy measurement is achieved by absorbing the particle energy in a bulk of material and then measuring the energy deposited in the process. High-energy photons, electrons and hadrons can interact with matter, producing secondary particles. At energies over 100 MeV, electrons lose energy primarily through the emission of bremsstrahlung, while photons lose energy through the production of electron-positron pairs. These secondary particles can then go on to create even more particles, creating a cascade of particles called a shower. Most calorimeters are designed to induce and measure

such showers [15]. There are two main types of calorimeters, electromagnetic (EM) and hadron. EM calorimeters mainly measure electrons and photons, while hadron calorimeters measure hadrons. Hadrons mostly pass through the EM calorimeter without creating nuclear interactions. The production of secondary particles in a hadron cascade is caused by inelastic hadronic processes, mainly the production of pions. The calorimeter is often divided into layers of dampening and signal layers. The dampening layers slow down the particles and create showers. Sandwiched between, or threaded through, the dampening layers are active sensing layers that registers the energy loss in the absorbers. These layers are usually scintillators, read out by *photomultipliers*, or some kind of ionizing medium, read out by registering electric pulses, like the straw tubes of the inner detector. These types of calorimeters are called *sampling calorimeters*. The calorimeters may also be constructed from a single material combining the properties of an absorber and a detector. These are called *homogeneous calorimeters*.

The calorimeter system in ATLAS, consists of two main parts: a liquid Argon (LAr) sampling calorimeter as well as a hadronic tile sampling calorimeter. Over half of the total weight of ATLAS, approximately 4000 tons, are located in the calorimeters. Pictures of the ATLAS calorimeters can be found in figure 2.6.

The ATLAS EM calorimeter is divided into three parts, a barrel as well as two end-caps. It has got plates shaped like accordions to ensure complete coverage in ϕ, without cracks. LAr makes up the active layers. The liquid argon is kept at -180°C. The Central Solenoid (CS) magnet is housed inside the EM calorimeter, in the same cryostat housing as the calorimeter. Because of its placement, it is important to keep the magnet as thin as possible, to minimize the amount of matter in front of the calorimeters. The calorimeters are preceded by a presampler to correct for the energy lost to material downstream in the detector.

The ATLAS hadron calorimeter is also divided into several parts: A scintillator tile calorimeter in the barrel as well as two LAr end-cap calorimeters. The barrel uses iron as the absorber material and plastic scintillator tiles as the active material. Photons created in the scintillators are carried away by wavelength shifting fibres and read out by photomultipliers. The iron in the barrel also acts as a magnetic flux return yoke for the CS. The hadronic LAr end-cap calorimeters are similar to the EM end-cap calorimeters, but uses copper plates instead of lead.

The end-caps also include high density forward calorimeters close to the beam pipe. These calorimeters have to handle a lot of radiation without loss of performance. This calorimeter also uses copper, as well as tungsten.

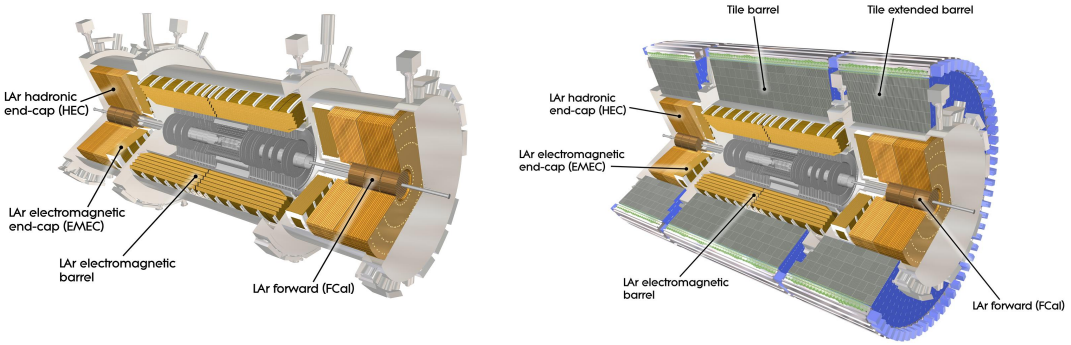

(a) The LAr and forward calorimeters [16]

(b) The complete ATLAS calorimeters [17]

Figure 2.6: The ATLAS calorimeters

2.3.4 Muon Spectrometer

The muon spectrometer, seen in figure 2.7, is the largest component of the ATLAS detector. It measures the momenta of muons by bending them in a magnetic field, just like in the ID. Muons are heavier than electrons, and interact less with the detector as they pass through it. Looking at equation 2.5 it is easy to see that electrons will lose a lot more energy than muons to bremsstrahlung. At typical production energies in the LHC, muons are minimum ionizing particles. This, combined with a long lifetime, 2.2×10^{-6} seconds [18], means that most muons will pass through the detector without decaying and without losing a lot of their energy. In fact, to absorb all the energy of a 10 GeV muon, you would need about 8 meters of lead[15]. This is why the muon detectors are the outermost parts of the detector, on the outside of the calorimeters.

The magnets in the muon spectrometer consists of three air-core toroid magnets, one in the barrel and two in the end-caps. Each toroid consists of eight superconducting coils each. The barrel coils are housed in individual cryostats, while in the end-caps all of the coils are housed in individual ones. The magnetic field deflect the muons in the R-z plane, unlike the CS, which deflects particles in the transverse plane. The strength of the magnetic field varies between 0.5 and 2 T.

The detectors in the muon spectrometer have to cover a large area, roughly 5000 m^2. Keeping the cost down while still achieving satisfactory resolution of the measurements becomes an issue. Monitored drift tubes (MDTs) and cathode strip chambers (CSCs) are used. The detectors are configured in three layers in the barrel as well as four end-cap disks at various distances from the interaction point. There are no detectors inside the end-cap cryostats, rather immediately before and after. In addition to the MDTs and CSCs, the muon trigger system

uses resistive plate chambers (RPCs) in the barrel and thin gap chambers (TGCs) in the end-caps.

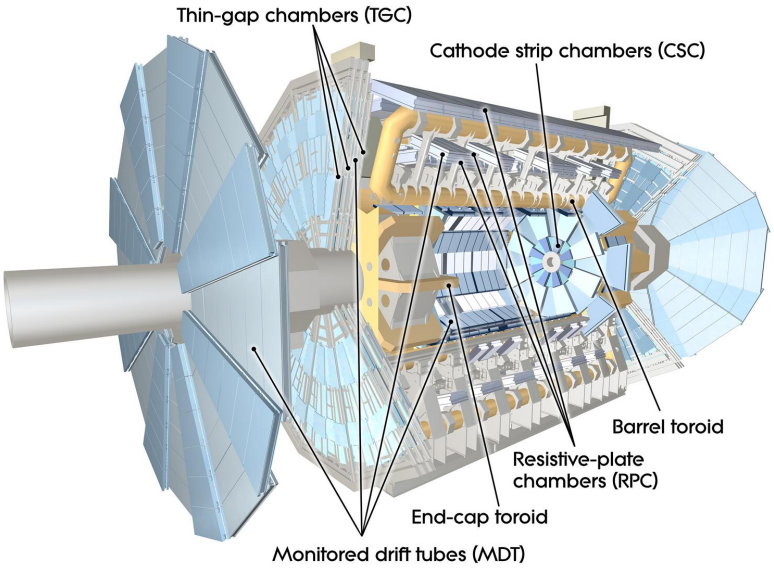

Figure 2.7: The ATLAS muon spectrometer [19]

2.3.5 Triggers and Data Acquisition (DAQ)

At design luminosity, with 25 ns bunch spacing, the bunch crossing frequency will be 40 MHz. With an estimated average of 23 events per bunch crossing the expected interaction rate in the detector is 10^9 Hz. For every collision event, approximately 1000 particles are created. This means that when storing events for later analysis, each event takes up 1 MB of storage. If every event in ATLAS were to be read out and stored, the output would be 1 petabyte (PB) per second. This would require an unheard of amount of storage space to achieve. Not all events are created equal however. Some are of more interest than others, such as those involving the Higgs boson or potential new physics. ATLAS implements a system of triggers, designed to reduce the event readout rate to a more manageable size. The triggers are hardware or software that uses limited or complete information from the detector to make quick decisions about keeping or scrapping certain events. In ATLAS this is done in three stages: The Level-1 trigger (LVL1), the Level-2 trigger (LVL2) and the Event Filter (EF). A graphical depiction of the trigger system is shown in figure 2.8.

LVL1 is a hardware trigger which uses low granularity information from the muon system and the calorimeters. It uses the RPCs and TGCs mentioned in

the previous section to select high-p_T muons. The calorimeter is used to select high-p_T electrons and photons, as well as jets and τ-leptons decaying hadronically. This is used to define Regions-of-Interest (ROIs) in the detector, which includes p_T info as well as energy sums. The latency of LVL1 is 2.0 μs. During this time the signal from the detector is stored in so-called "pipeline" memory while waiting to be accepted or rejected by the trigger. Events that pass the trigger are passed on to LVL2. LVL1 reduces the event rate to 75 kHz.

LVL2 and the EF is known collectively as the High Level Trigger (HLT). Unlike the LVL1, the HLT is a software trigger. LVL2 has access to the complete data from the detector. It focuses on the ROI's defined by LVL1 as well as other rejection criteria to further reduce the event rate down to around 3.5 kHz. Each event takes around 40 ms to process [20].

The EF has a lot more time to reach a decision, around 4 seconds, and is therefore able to implement algorithms like track and vertex reconstruction. This would require too much processing power and therefore take to long to be usable in LVL2. These algorithms are similar to those utilized in the offline analysis. The EF also includes alignment information and magnetic field maps. This final level of the trigger system reduces the rate read out to permanent storage to 200 Hz.

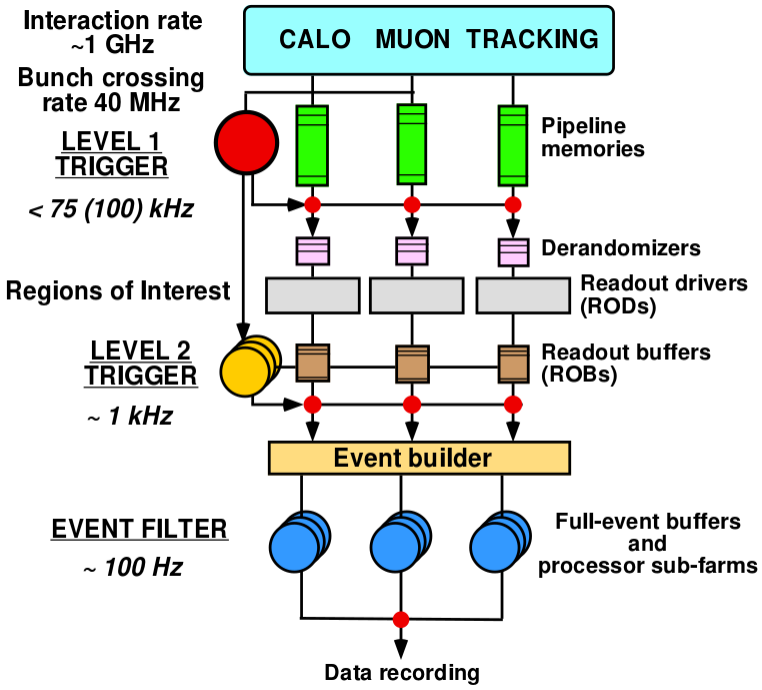

Figure 2.8: Overview of the ATLAS trigger and DAQ systems [21]

The expected η coverage and design resolutions of the ATLAS subdetectors are

listed in table 2.1.

Subdetector	η coverage	Expected resolution
ID	$\pm$ 2.5	$\sigma_{p_T}/p_T = 0.05\% \, p_T \oplus 1\%$
EM calorimeter	$\pm$ 3.2	$\sigma_E/E = 10\%/\sqrt{E} \oplus 0.7\%$
Hadronic calorimeter	$\pm$ 3.2	$\sigma_E/E = 50\%/\sqrt{E} \oplus 3\%$
Forward calorimeter	$3.1 < \lvert\eta\rvert < 4.9$	$\sigma_E/E = 100\%/\sqrt{E} \oplus 10\%$
Muon spectrometer	$\pm$ 2.7	$\sigma_{p_T}/p_T = 10\%$ at $p_T = 1$ TeV

Table 2.1: Expected resolutions and pseudorapidity coverage of the various ATLAS subdetectors [20].

2.3.6 Physics in ATLAS

The detector only measures various signals like tracks and energy deposits. We need to tie these objects observed in the detector to physical objects like electrons, photons, Higgs bosons etc. For this we need methods for particle identification. Figure 2.9 shows how a selection of common subatomic particles interact with the detector. Charged particles leave tracks and bend in the ID, while neutral particles pass through it undetected. Both charged and neutral particles leave energy depositions in the calorimeters. Electrons and photons are mostly absorbed by the EM calorimeter, while hadrons, like protons and neutrons are absorbed in the hadronic calorimeter. Muons pass through the whole detector, interacting with every subdetector along the way. Neutrinos are so weakly interacting that they leave no trace in the detector. All is not lost however. In the initial collisions the sum of the energy in the transverse plane have to be zero due to energy conservation. By summing over transverse energy we can deduce where a neutrino has passed through the detector in the transverse plane[4].

Separating particles from one another is not as trivial as it might seem. Different particles can leave similar signatures in the detector. A particle may also decay into other particles in one of the subdetectors. Photons for example, has between 10% and 50% chance of decaying into an e^+e^- pair before leaving the SCT [20]. Following is a summary of how ATLAS identifies some important physical objects.

Muon reconstruction is mainly based on track reconstruction in the ID and muon spectrometer. The ID have the best performance at low energies, while the spectrometer dominates at energies over 30 GeV.

[4]There are also several particles in BSM models, such as SUSY, where the created particles would not be directly observed in the detector. This makes the measurement of missing transverse energy even more important.

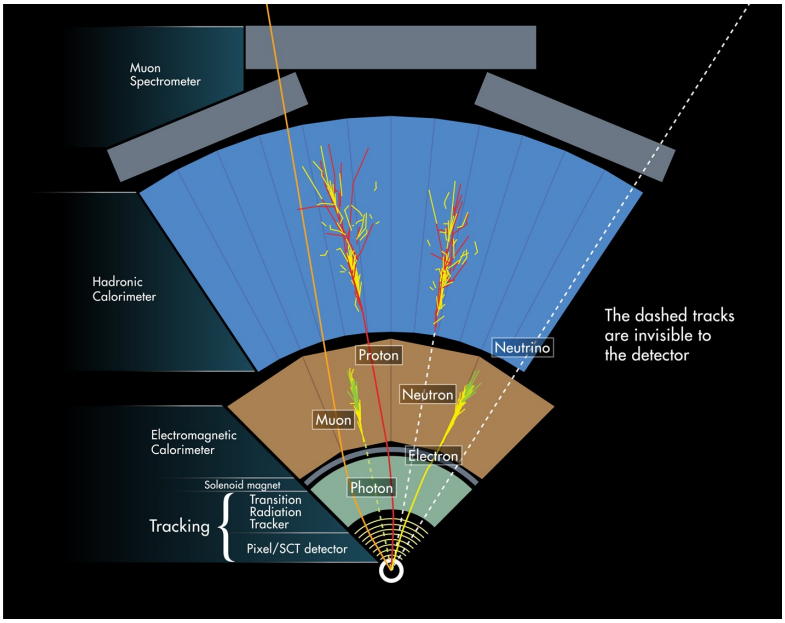

Figure 2.9: Detection of particles in ATLAS. Seen here is a cross section of the barrel region. Note that only one of three muon chambers is showing. [22]

Quarks and gluons produced in the collision will fragment into a cone of hadrons called a *jet*. Quarks and gluons have colour charge, but because of the QCD[5] phenomenon known as *confinement* more quarks are produced to form colour neutral objects, such as pions. This process is known as *hadronization*. Jets are the dominant products in the LHC. In ATLAS, information from the ID as well as the calorimeters are used to identify jets. Tau leptons decaying hadronically also form jets. When studying processes involving tau leptons decaying to hadrons it is important to separate these jets from those created in QCD processes. More about this in chapter 6.

Photons do not leave tracks in the ID. They do, however, sometimes decay into an e^+e^- pair in the ID. This is known as *photon conversion*. Such a photon can be reconstructed by finding its decay vertex in the ID. The efficiency of this goes down for large radii in the ID, because of fewer measurement points with which to reconstruct a track. A conversion can also be identified using one of the two tracks created while posing certain conditions [20]. Electrons are reconstructed using a combination of hits in the ID and energy deposits in the EM calorimeter. Several methods are in place to separate them from other physical objects. The energy of the electron divided by its momentum should be close to one. This can

[5]QCD is covered in chapter 3

be used to separate electrons from jets. Another method is to study the amount of *transition radiation* created in the TRT. This provides electron/pion separation. There are three sets of cuts in place for electrons: "loose", "medium" and "tight". The identification becomes more precise for tighter cuts, but the efficiency goes down. Electron and photons are both reconstructed in the EM calorimeter using a sliding-window algorithm. The size of the windows corresponds to 5x5 cells in the middle of the calorimeter for electrons and 3x5 for unconverted photons. The size of the calorimeter clusters used have to balance the requirement of containing as much of the EM shower as possible while minimizing noise and pileup. Electrons are required to have tracks in the ID with no conversion.

3 The Standard Model

The SM is the currently agreed upon model for explaining the basic constituents of matter and the forces with which they interact[1]. It is consistent with quantum mechanics and special relativity.

3.1 Units and Notation

In SI or SCG units, mass, length and time are natural dimensions. An alternative to this, one more commonly used in relativistic quantum mechanics, is *natural units*. In natural units mass, action and velocity are fundamental dimensions. The reduced Planck constant[2] $\hbar = h/2\pi$ is used as a unit for action and the velocity of light in a vacuum c as a unit for velocity. c=$\hbar$=1 in natural units. In natural units the momentum-energy relation becomes:

$$E^2 = m^2 + \boldsymbol{p}^2 \tag{3.1}$$

It is clear that in natural units, mass, energy and momentum have the same unit. In particle physics experiments it is customary to use electron volt (eV). One eV is the energy acquired by an electron moving across a 1 Volt potential. The energies of the particles produced at the LHC are so large that GeV[3] are more commonly used. Unless stated otherwise, natural units is used in this thesis. A comparison of common physical quantities in SI and natural units can be seen in table 3.1.

A space-time four-vector is often written as x^μ, with a Greek letter index. $\mu = 0$ denotes the time component, while the rest are the space components. The *covariant* vector x_μ is defined from the contravariant x^μ as

$$x_\mu = \sum_{\nu=0}^{3} g_{\mu\nu} x^\mu \equiv g_{\mu\nu} x^\mu \tag{3.2}$$

where $g^{\mu\nu}$ is the contravariant metric tensor. It is customary to omit writing the summation symbol. Repeated indices, one covariant and one contravariant, implies summation. The product $x^\mu x_\mu$ is invariant under Lorentz transformations.

[1] Gravity is not yet explained in the SM

[2] Plancks constant h is defined as $h \approx 4.136 \times 10^{15} eV\, s$

[3] one GeV is 10^6 eV.

Quantity	Natural Units	SI
Mass	eV	kg or eV/c^2
Time	1/eV	s
Length	1/eV	m
Velocity	c	m/s
Energy	eV	eV
Momentum	eV	eV/c

Table 3.1: Comparing SI and natural units

$p^\mu = (E, \boldsymbol{p})$, the energy-momentum vector, is a common example of such a vector. The space-time analogue to $\boldsymbol{\nabla}$ transforms like a four-vector and is defined as $\partial^\mu = (\partial/\partial t, \boldsymbol{\nabla})$.

3.2 Overview

The elementary particles of the SM are divided into two main categories: *fermions* and *bosons*. Fermions are spin[4] 1/2 particles that make up all visible matter in the universe. The fermions are named after Enrico Fermi, by Paul Dirac. There are 12 flavours of these fundamental fermions, divided into two groups, quarks and leptons. These subgroups are further divided into three "generations" or "families", ordered by rising mass of the particles in it. Every generation contains an *up-type* and a *down-type* quark of similar mass as well as a charged and a neutral lepton. A table of these particles can be found in table 3.2. For every charged fermion there exist a corresponding anti-particle. Antiparticles have the same mass as their corresponding particles, but opposite charge. Antiparticles were first predicted by Dirac in 1932 as a way to interpret negative energy solutions to the Dirac equation.

The bosons, also named by Diracm after Satyendra Nath Bose, in the SM are spin 1 particles. They are, except the Higgs boson, responsible for mediating the fundamental subatomic interactions: The weak interaction, the strong interaction and the electromagnetic interaction. Only electrically charged particles participate in electromagnetic interactions. This happens through the exchange of photons. photons are massless, and as a consequence the electromagnetic interaction has infinite range. Up-type quarks have electrical charge $+2/3e$, while the down-type quarks have charge -1/3e. The charged leptons, e, μ and τ, all have charge $+1e$. The neutrinos are neutrally charged. Analogous to electric charge, quarks

[4]Spin is a form of angular momentum. It is somewhat analogous to the angular momentum of a spinning body. For a point particle there is no macroscopic analogy, making spin a purely intrinsic quantum mechanical quantity.

	Generation 1		2		3	
Type	Name	Symbol	Name	Symbol	Name	Symbol
Quarks	Up Down	$\binom{u}{d}$	Charm Strange	$\binom{c}{s}$	Top Bottom	$\binom{t}{b}$
Leptons	Electron e-neutrino	$\binom{e}{\nu_e}$	Muon μ-neutrino	$\binom{\mu}{\nu_\mu}$	Tau τ-neutrino	$\binom{\tau}{\nu_\tau}$

Table 3.2: The elementary fermions of the standard model

also carry colour charge. The three colour charges are red, green and blue. For every colour there also exist an anti-colour. *Gluons*, mediators of the strong force, only couple to coloured objects. Unlike the electrically neutral photons, gluons are themselves coloured, which means that they can self-interact. Note that the quarks and gluons are not red, green or blue in the optical sense of the word, colour is simply a quantum number of quarks and gluons.

Quarks are never observed individually. Because of confinement, only colour neutral objects can exist in nature. A red, green and blue quark form a colour neutral baryon, while a quark anti-quark pair bind together to form a meson. Baryons and mesons form the class of particles known as hadrons.

The weak force is mediated by the neutral Z^0 boson and two charged bosons, W^- and W^+. The range of an interaction is given by the Compton wavelength of the particle transmitting it. The high mass of Z^0, W^- and W^+ means that the range of the weak interaction is of the order 10^{-3} fm. At low energies it may actually be considered a zero-range interaction [23]. This high mass also made the weak bosons elude observation for a long time. They were not discovered until 1983, years after being postulated. The final piece of the puzzle is the Higgs boson. It has zero spin and is not a force mediator like the other bosons. It is needed in our theories to give mass to the fermions and weak bosons. The Higgs is discussed more in section 3.8.

Force	Boson	Mass [GeV]	Charge [e]	Spin
Electromagnetism	photon γ	0	0	1
Weak Force	Z^0,$W^\pm$	91.2, 80.4	0,$\pm$1	1
Strong Force	gluon g	0	0	1

Table 3.3: Force carriers of the SM. W and Z mass collected from [18]

3.3 Quantum Field Theory

The concept of quantum fields can be traced back to Planck, who in 1900 postulated that emission and radiation from atoms isn't a continuous spectrum, but rather happens in discrete quanta of energy. This was done because the continuous picture was divergent at small wavelengths, leading to the absurd prediction that an ideal black body at thermal equilibrium will emit infinite power. Einstein took this interpretation one step further in 1905, when he concluded that the electromagnetic field itself is quantized. The quanta of the electromagnetic field later became known as photons. Not only did it turn out that light is made up of particles. The french physicist Louis de Broglie showed in his 1924 PhD thesis that all matter has wave properties.

Quantum Field Theory (QFT) is the mathematical framework we use to describe the fundamental particles and their interactions. It's foundations was laid by Dirac in his 1927 paper "The Quantum Theory of Emission and Absorption of Radiation" [24]. A field is an unseen entity permeating space and time. Some classical examples are electromagnetic and gravitational fields. Classical fields doesn't contain one of the fundamental properties of the real universe, it's discreteness. There is no classical analogue to the concept of a minimal piece of matter, a fundamental particle. One of the fundamental differences between classical and quantum fields is the use of operators. A classical field inputs a coordinate and outputs the value of the field in that point, while a quantum field outputs an operator. A simplistic way of picturing a quantum field is to imagine a quantum harmonic oscillator at every point in space. The ground state of each harmonic oscillator is the vacuum, with higher energy states at equidistant energy from each other. The raising and and lowering operators of the harmonic oscillator are responsible for creating and annihilating particles. Raising the energy from the vacuum to the first energy state is equivalent to creating a particle in this state. A quantum harmonic oscillator in the n'th energy state $E_n = (n + 1/2)\hbar\omega$ can be interpreted as n particles of energy $\hbar\omega$. The fact that particles are created and annihilated necessitates the use of many particle field theories over single particle wave equations. Even at energies too low to induce pair creation, perturbation theory allows for intermediate multi-particle states [25].

The action S is an important quantity in quantum field theory. It is defined as the space-time integral of the *Lagrangian* $\mathcal{L}$ over some arbitrary region of space-time. In QFT, $\mathcal{L}$ is a function of the fields and their derivatives and is defined as kinetic energy minus potential energy of the system T - V. In particle physics it

is customary to use the *Lagrangian density* $\mathcal{L}$[5]. In terms of the $\mathcal{L}$, S is:

$$S = \int d^4x \mathcal{L}(\phi, \partial_\mu \phi) \tag{3.3}$$

Hamilton's principle of least action states states that the classical trajectory taken by a particle in space-time is such that S is stationary. This can be used to find the equations of motion of the system:

$$\begin{aligned} \delta S &= \int d^4x \left\{ \frac{\partial \mathcal{L}}{\partial \phi} \delta\phi + \frac{\partial \mathcal{L}}{\partial(\partial_\mu \phi)} \delta(\partial_\mu \phi) \right\} \\ &= \int d^4x \left\{ \frac{\partial \mathcal{L}}{\partial \phi} \delta\phi + \partial_\mu \left(\frac{\partial \mathcal{L}}{\partial(\partial_\mu \phi)} \right) \delta\phi + \partial_\mu \left(\frac{\partial \mathcal{L}}{\partial(\partial_\mu \phi)} \delta\phi \right) \right\} = 0 \end{aligned} \tag{3.4}$$

The last term in the equation above can be transformed into a surface integral over the four dimensional space-time region we are considering. The fields are considered stationary on the surface, thus $\delta\phi = 0$ and the term vanishes. We are then left with the *Euler-Lagrange* equation:

$$\frac{\partial \mathcal{L}}{\partial \phi} - \partial_\mu \left(\frac{\partial \mathcal{L}}{\partial(\partial^\mu \phi)} \right) = 0 \tag{3.5}$$

Solving this equation yields the equation of motion for the field ϕ.

3.4 Symmetries and Conservation Laws

Noether's theorem states that for every continuous symmetry of the Lagrangian $\mathcal{L}$ there is a corresponding conserved quantity. A symmetry is a transformation $\phi \to \phi' = \phi + \alpha\Delta\phi$ that leaves the equations of motion invariant. The SM Lagrangian is required to be invariant under such symmetry transformations. This warrants the inclusion of additional fields, which couple to the original fields and can be interpreted as the fields of the force carrying bosons of the theory. Group theory is the mathematical tool used to describe symmetries. The symmetry groups of the SM are called *gauge transformation groups*. These groups are continuous and local, meaning space-time dependent.

[5]The Lagrangian density is far more in use in QFT than the complete Lagrangian. Physicists therefore often refer to this as the Lagrangian. Moving forward, this text will use this convention as well.

3.4.1 Group Theory

Definition 3.1 *Definition of a group G: A set of elements $g \in G$ and an operator "$\circ$" satisfying the following conditions:*

- *Closure of $\circ$: if $g, h \in G$ then $g \circ h \in G$*
- *Existence of identity element: $e \in G$ such that $e \circ g = g \circ e = g \in G$*
- *Existence of inverse: $g^{-1} \in G$ for each $g \in G$ such that $g^{-1} \circ g = g \circ g^{-1} = e$*
- *Associativity: $f, g, h \in G : (f \circ g) \circ h = f \circ (g \circ h)$*

A group is said to be *unitary* if they can be represented in terms of complex $n \times n$ unitary matrices. A $n \times n$ matrix U is unitary if it satisfies the condition

$$U^\dagger U = I_n \tag{3.6}$$

where I_n is the $n \times n$ identity matrix and $U^\dagger = U*^T$. A unitary group of order n is denoted U(n). A group is *special unitary* if it also satisfies

$$det\, U = 1 \tag{3.7}$$

In this case it is denoted as SU(n). A Lie group is a group whose elements can be written as

$$g = e^{i\alpha_i T_i}, \qquad i = 1, \ldots, n \tag{3.8}$$

where T_i is the *generators* of the group and α_i is an arbitrary real number. A group is said to be *Abelian* if all its elements commute with each other. In the SM, fields added to ensure invariance under Abelian symmetry groups do not interact with themselves, while those of a non-Abelian group does. The SM uses three symmetry groups: U(1), SU(2) and SU(3). These are what's known as internal symmetries, and will be covered in the following sections. In addition to these internal symmetries the SM Lagrangian is also invariant under transformations of the Pointcaré group. This is known as an external symmetry, and ensures conservation of energy, momentum and angular momentum. The Pointcaré group will not be covered in this text.

3.5 Quantum Electrodynamics

Quantum Electrodynamics (QED) is, as its name implies, the quantum field treatment of electrodynamics. The electric and magnetic fields $\boldsymbol{E}$ and $\boldsymbol{B}$ can be expressed in therms a vector field $\boldsymbol{A}$ and a scalar field ϕ:

$$\boldsymbol{E}(\boldsymbol{x}) = -\boldsymbol{\nabla}\phi(\boldsymbol{x}) - \frac{\partial \boldsymbol{A}(\boldsymbol{x})}{\partial t}, \qquad \boldsymbol{B}(\boldsymbol{x}) = \boldsymbol{\nabla} \times \boldsymbol{A}(\boldsymbol{x}) \tag{3.9}$$

$\boldsymbol{A}$ and ϕ can be changed without changing the observable fields $\boldsymbol{E}$ and $\boldsymbol{B}$. For any scalar function f the following transformations leave $\boldsymbol{E}$ and $\boldsymbol{B}$ unchanged:

$$\phi'(\boldsymbol{x}) = \phi(\boldsymbol{x}) - \frac{\partial f(\boldsymbol{x})}{\partial t}, \qquad \boldsymbol{A}'(\boldsymbol{x}) = \boldsymbol{A}(\boldsymbol{x}) - \boldsymbol{\nabla} f(\boldsymbol{x}) \tag{3.10}$$

This is a U(1) gauge symmetry.

Consider the free Lagrangian of a spin-1/2 fermion field ψ of mass m:

$$\mathcal{L} = \overline{\psi}(x)(i\gamma^\mu \partial_\mu - m)\psi(x) \tag{3.11}$$

This describes for example a free electron. We want to ensure invariance of the Lagrangian under U(1) transformations of the field:

$$\begin{aligned} \psi(x) \to \psi'(x) =& \psi(x)e^{-iqf(x)} \\ \overline{\psi}(x) \to \overline{\psi}'(x) =& \overline{\psi}(x)e^{iqf(x)} \end{aligned} \tag{3.12}$$

The resulting Lagrangian is not invariant, but rather has an added term $q\overline{\psi}(x)\gamma^\mu\psi(x)\partial_\mu f(x)$. All is not lost however. Invariance can be restored by adding a new field A_μ that transforms according to

$$A_\mu \to A'_\mu = A_\mu + \partial_\mu f(x) \tag{3.13}$$

Equations 3.12 and 3.13 coupled together is called a gauge transformation. Through what is known as *minimal substitution* the derivative ∂_μ is substituted by the *covariant derivative*:

$$D_\mu = \partial_\mu + iqA_\mu \tag{3.14}$$

This substitution equals adding an interaction term between A_μ and ψ in the Lagrangian, cancelling the term added by the transformations 3.12. The resulting Lagrangian is thus invariant under U(1) gauge transformations:

$$\mathcal{L} = \overline{\psi}(x)(i\gamma^\mu D_\mu - m)\psi(x) - \frac{1}{4}F^{\mu\nu}F_{\mu\nu} \tag{3.15}$$

The free Lagrangian of the field A_μ has also been included. $F^{\mu\nu}$ is the electromagnetic strength tensor and is given by:

$$F^{\mu\nu} = \partial^\nu A^\mu - \partial^\mu A^\nu \tag{3.16}$$

QED has proven to be a tremendously successful theory. It's predicted value for the magnetic moment of the electron agrees with the measured value to more than ten significant figures [26]. This is the most accurately measured property of any elementary particle. QED also correctly predicts the Lamb shift in the energy spectrum of the hydrogen atom.

3.5.1 Feynman Diagrams

A useful tool when studying QED processes are Feynman diagrams. Calculating probability amplitudes and matrix elements in QED can be cumbersome. However, these calculations can be simplified greatly by using Feynman diagrams as well as a simple set of rules called Feynman rules. Roughly speaking, Feynman diagrams describe the flow of particles in an interaction. Time runs along the x-axis, while the y-axis describes spatial movement. Lines coming in from the left describes initial state particles, while those exiting to the right are final state particles. Intermediate states run between vertices in the diagram. A simple example diagram is shown in figure 3.1. Solid lines represent fermions, while wavy lines represent photons. The arrows on the fermion lines represent particles or antiparticles. Ordinary fermions have arrows pointing towards the right, while anti-fermions have arrows pointing towards the left. This stems from Ernst Stueckelberg's interpretation of positrons as electrons running backward in time.

To calculate the matrix element of a process, draw up all the Feynman diagrams contributing to the process, up to the desired order in perturbation theory. This can then be used to calculate the matrix element using Feynman rules.

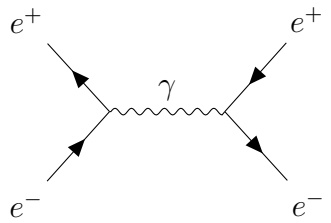

Figure 3.1: Example Feynman diagram of an e^+e^- annihilation process. Time runs along the x-axis. Feynman diagrams in this text are drawn using the tikz-Feynman latex package, developed by J. Ellis [27].

3.6 Quantum Chromodynamics

In the 1960's it was first proposed, by Gell-Mann and Zweig, and later confirmed by deep inelastic scattering experiments that hadrons are not elementary particles. They are made up of quarks, bound together by the strong nuclear force. For the valence quarks[6] inside certain hadrons to obey the Pauli exclusion principle, requiring the total wave function of the particles to be antisymmetric under exchange of particles, a new quantum number has to be introduced. This is how colour charge was found. Motivated by the success of QED, it is tempting to try to construct a similar theory describing how quarks and gluons interact. The resulting theory is named Quantum Chromodynamics (QCD), analogue to QED.

Starting from the free Lagrangian of a fermion field, equation 3.11, the free QCD is given as:

$$\mathcal{L}_0 = \overline{\Psi}^f(x)(i\gamma^\mu\partial_\mu - m_f)\Psi^f(x) \tag{3.17}$$

Unlike QED, which has a single charge, colour charge must be taken into account. The QCD spinor is given as:

$$\Psi^f = \begin{pmatrix} \psi^f_r \\ \psi^f_g \\ \psi^f_b \end{pmatrix} \tag{3.18}$$

The index f implies a sum over quark flavour (u, d, c etc.). r, g and b are the three colour charges; red, green and blue. This colour triplet is analogous to spin doublets in quantum mechanics. The approach taken to yield the QCD Lagrangian is again very similar to the one used for QED. However, where the QED Lagrangian is invariant under U(1) gauge transformations, the QCD Lagrangian is invariant under SU(3) gauge transformations. Through minimal substitution the resulting Lagrangian becomes:

$$\mathcal{L} = \overline{\Psi}^f(x)(i\gamma^\mu D_\mu - m_f)\Psi^f(x) - \frac{1}{4}G_i^{\mu\nu}G_{i\mu\nu} \tag{3.19}$$

SU(3) has eight generators, meaning that eight new fields A_i has to be added to the interaction term in the Lagrangian. Physically, this means that there are eight gluons. The free Lagrangian of the gluon fields are given as:

$$G_i^{\mu\nu}(x) \equiv F_i^{\mu\nu}(x) + g_s f_{ijk} A_j^\mu(x) A_k^\nu(x) \tag{3.20}$$

[6]The common picture of hadrons consisting of just three quarks, is a bit too simplistic. The *valence* quarks of a proton are two up quarks and a down quark, but it also contains a soup of quark-antiquark pairs continuously creating and annihilating, as well as gluons

Note the difference from free photon Lagrangian in eq. 3.15. The second term, added to make the total Lagrangian invariant, indicate that the gluons interact not only with quarks, but also with each other. This means that the gluons also carry colour charge. The tensor $F_i^{\mu\nu}(x)$ is given by:

$$F_i^{\mu\nu}(x) \equiv \partial^\nu A_i^\mu - \partial^\mu A_i^\nu \tag{3.21}$$

where i sums over the SU(3) generators(8).

So far QCD has seemed virtually analogous to QED. However, QCD describes a strong interaction, and is therefore not solvable by lowest order perturbation theory. The strong interaction is only "strong" at distances at the order of 1fm. At smaller distances, its strength wanes. This property is called " *asymptotic freedom*. This is completely opposite of the electromagnetic interaction, which increases in strength at small distances. The difference is caused by the non-Abelian[7] properties of QCD. Asymptotic freedom leads to a phenomenon known as colour confinement. Due to the fact that the strong force increases with distance, if one tries to separate out a quark from a hadron, the potential energy builds to a point where it is more energetically favourable to spontaneously create a quark-antiquark pair. As a result of this, only colour neutral objects are allowed to exist in nature. This leads to a process known as hadronization. If a quark-antiquark pair are created at the LHC, they will immediately form hadrons together with quarks created from the vacuum. In a particle detector, the resulting cascade of hadrons is called a jet.

3.7 Electroweak Theory

Pauli postulated the existence of the neutrino in 1930, to describe the missing energy in the β-decay energy spectrum. A new theory was also needed to explain the flavour changing properties of such decays. In neutron β-decay for example, a down-type quark changes flavour into an up-type quark. This is not possible to achieve through electromagnetic or strong interactions. This prompted the introduction of the weak force. The range of the weak force is very short due to its force mediators, the W^+, W^- and Z, being massive.

Experimental studies of weak processes show that only left-handed chirality leptons partake in weak interactions. The left or right handed component of a lepton state can be projected out using the chirality operators P^L and P^R:

$$\left.\begin{aligned}\psi^L(x) = P^L\psi(x) = \\ \psi^R(x) = P^R\psi(x) = \end{aligned}\right\} = \frac{1 \pm \gamma^5}{2}\psi(x) \tag{3.22}$$

[7] A group is Abelian if its members commute, and non-Abelian if they do not.

Helicity is defined as +1 when the spin of a massless particle is parallel to its momentum and -1 in the opposite case. chirality is equal to helicity for massless particles, and at relativistic energies the two are equal. Helicity is independent of reference frame, chirality is not. To construct a gauge theory of weak interaction, leptons must be assumed to be massless. The next section will introduce the mechanism that allows for them to have mass. Since only left-handed leptons interact weakly the different lepton states are grouped according to their chirality. Left handed leptons are arranged in two-component spinors:

$$\Psi_l^L(x) = \begin{pmatrix} \psi_l^L(x) \\ \psi_{\nu_l}^L(x) \end{pmatrix}, \qquad \overline{\Psi}_l^L(x) = (\overline{\psi}_l^L(x), \overline{\psi}_{\nu_l}^L(x)) \tag{3.23}$$

The index l implies summation over lepton flavour; electron, muon and tau. The free lepton Lagrangian becomes:

$$\mathcal{L}_0 = \overline{\Psi}_l^L(x) i\gamma^\mu \partial_\mu \Psi_l^L(x) + \overline{\psi}_l^R(x) i\gamma^\mu \partial_\mu \psi_l^R(x) + \overline{\psi}_{\nu_l}^R(x) i\gamma^\mu \partial_\mu \psi_{\nu_l}^R(x) \tag{3.24}$$

Requiring that this Lagrangian is invariant under SU(2) gauge transformations of the left-handed spinor yields three new conserved currents:

$$J_i^\alpha = \frac{1}{2}\overline{\Psi}_l^L(x)\gamma^\mu \sigma_i \Psi_l^L, \qquad i = 1, 2, 3 \tag{3.25}$$

where σ_i are the three generators of SU(2), the Pauli matrices. The right handed fields are singlets under this transformation. Weak isospin charge I_i, or simply weak isospin, are the conserved quantities corresponding to these currents. The third current, which is neutral, looks very similar to the electromagnetic current:

$$J_3^\alpha = \left[\overline{\psi}_{\nu_l}^L(x)\gamma^\alpha \psi_{\nu_l}^L(x) - \overline{\psi}_l^L(x)\gamma^\alpha \psi_l^L(x)\right] \tag{3.26}$$

This suggests that the weak force and the electromagnetic force can be merged together. Weinberg, Glashow and Salam developed the theory of electroweak unification in the 1960's. This unification is only seen at high energies however. At low energies, the two forces are clearly distinguishable. Combining the third weak current and the electromagnetic current yields the *weak hypercharge current*:

$$J_y^\alpha = \frac{1}{2}\overline{\Psi}_l^L(x)\gamma^\alpha \Psi_l^L(x) - \overline{\psi}_l^R(x)\gamma^\alpha \psi_l^R(x) \tag{3.27}$$

The corresponding charge is called *hypercharge* Y. It is related to electric charge and weak isospin by the Gell-Mann-Nishijima formula:

$$Q = I_3 + \frac{1}{2}Y \tag{3.28}$$

The electroweak force is said to be invariant under $\mathrm{SU}(2)_L \times \mathrm{U}(1)_Y$. To ensure this invariance, four new fields must be introduced, as well as covariant derivatives. Three of the new fields, W_i, are added due to $\mathrm{SU}(2)_L$. $B(x)$ is added due to the $\mathrm{U}(1)_Y$ transformation. W_1 and W_2 can be combined linearly such that they correspond to the charged bosons of the weak force, W^+ and W^-:

$$\begin{aligned} W_\mu(x) &= \frac{1}{\sqrt{2}}\left[W_{1\mu}(x) - iW_{2\mu}\right] \\ W^\dagger_\mu(x) &= \frac{1}{\sqrt{2}}\left[W_{1\mu}(x) + iW_{2\mu}\right] \end{aligned} \tag{3.29}$$

Similarly, W_3 and B can be expressed as a linear combination of the two fields A and Z which correspond to the photon and Z-boson fields respectively:

$$\begin{aligned} W_{3\mu}(x) &= \cos\theta_W Z_\mu(x) + \sin\theta_W A_\mu(x) \\ B_\mu(x) &= -\sin\theta_W Z_\mu(x) + \cos\theta_W A_\mu(x) \end{aligned} \tag{3.30}$$

θ_W is known as the Weinberg angle, or the weak mixing angle.

The electroweak Lagrangian, for massless leptons, now looks like:

$$\mathcal{L} = i\left[\overline{\Psi}^L_l(x)\gamma_\mu D^\mu \Psi^L_l(x) + \overline{\psi}^L_l(x)\gamma_\mu D^\mu \psi^L_l + \overline{\psi}^R_{\nu_l}(x)\gamma_\mu D^\mu \psi^R_{\nu_l}(x)\right] \tag{3.31}$$

The covariant derivatives are different depending on which field it operates on:

$$\begin{aligned} D^\mu \Psi^L_l(x) &= \left[\partial^\mu + ig\delta_j W^\mu_j(x)/2 - ig' B^\mu(x)/2\right]\Psi^L_l(x) \\ D^\mu \psi^R_l(x) &= \left[\partial^\mu - ig' B^\mu(x)\right]\psi^R_l(x) \\ D^\mu \psi^R_{\nu_l}(x) &= \partial^\mu \psi^R_{\nu_l}(x) \end{aligned} \tag{3.32}$$

Quarks also interact weakly. Left handed quark fields are arranged in two-component spinors like the leptons and neutrinos. Each of the three quark generation, with an up-type and a down-type, make up one of these spinors. Weak interactions are not limited within each doublet. For example, an up type quark may transform into any down-type quark through the emission of a W^+. The mixing between the quark generations is governed by the Cabbibo-Kobayashi-Maskawa (CKM) matrix. The various quark and lepton doublets are shown in table 3.2.

3.8 The Higgs Mechanism

In the last section a gauge invariant model for the electromagnetic and weak interactions was developed. However, for its gauge invariance to be preserved, all gauge bosons and lepton masses had to be set equal to zero. For these particles to regain their mass, the electroweak $SU(2)_L \times U(1)_Y$ symmetry has to be broken at low energies, separating the electromagnetic and weak forces. This will allow the weak gauge bosons, as well as the leptons, to gain mass, while photons remain massless. This phenomenon is called spontaneous symmetry breaking. A macroscopic example of spontaneous symmetry breaking can be found in ferromagnets. At room temperature there is no magnetisation in the metal, there is no preferred direction in space. If the metal is cooled down, the spins of the atoms inside the magnet align, making the metal magnetised. A clear directional preference emerges. The spatial symmetry of the system is spontaneously broken. The direction of this alignment is random.

The simplest quantum field theory exhibiting spontaneous symmetry breaking is the Goldstone Model. The Lagrangian of this model is

$$\mathcal{L} = \partial^\mu \phi^*(x) \partial_\mu \phi(x) - \mu^2 |\phi(x)|^2 - \lambda |\phi(x)|^4 \tag{3.33}$$

where $\phi(x)$ is an arbitrary complex scalar field:

$$\phi(x) = \frac{1}{\sqrt{2}} \left[\phi_1(x) + i\phi_2(x)\right] \tag{3.34}$$

The last two terms of eq. 3.33 are the potential energy of the field. This Lagrangian is invariant under global U(1) transformations. The potential energy terms must be bounded from below. This means that λ must be a positive number. μ^2 can take any value. Plotting the two potential terms as a function of ϕ_1 and ϕ_2 yields two different surfaces for positive or negative values of μ^2. For positive values of μ^2, the potential has a unique minimum for $\phi = 0$. This means that spontaneous symmetry breaking is not possible. If μ^2 is negative, however, the potential changes. It famously takes a shape reminiscent of a Mexican sombrero or the bottom of a wine bottle. This potential can be seen in figure 3.2. In this configuration, the minimum of the potential is degenerate. "Choosing" one of the minima to represent the vacuum ground state breaks the U(1) symmetry of the system. The ring of minima is located at

$$\phi_0 = \left(\frac{-\mu^2}{2\lambda}\right)^{1/2} e^{i\theta} \tag{3.35}$$

where θ defines an angle in the complex ϕ-plane. Setting θ to zero yields the

following vacuum expectation value:

$$\phi_0 = \left(\frac{-\mu^2}{2\lambda}\right)^{1/2} = \frac{v}{\sqrt{2}} \tag{3.36}$$

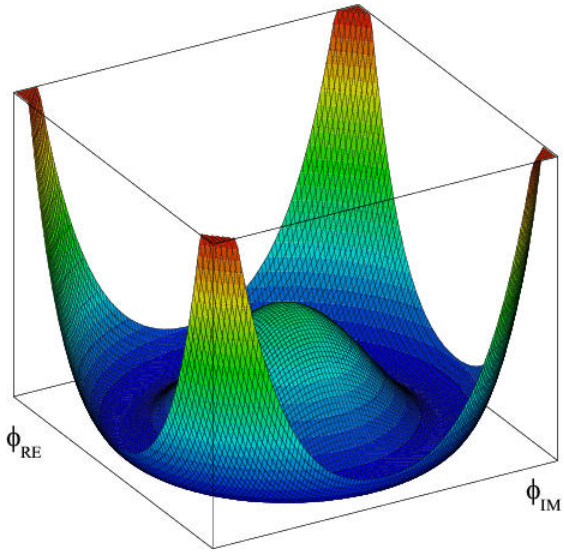

Figure 3.2: Goldstone Potential [28]

ϕ may be rewritten as

$$\phi(x) = \frac{1}{\sqrt{2}}\left[v + \sigma(x) + i\eta(x)\right] \tag{3.37}$$

which corresponds to expanding around the minimum. The real fields η and σ are suitable for quantization, as they correspond to real particles. Putting eq. 3.37 into eq. 3.33 yields the following Lagrangian:

$$\begin{aligned}\mathcal{L} = &\frac{1}{2}\partial^\mu\sigma(x)\partial_\mu\sigma(x)\frac{1}{2}\partial^\mu\eta(x)\partial_\mu\eta(x) - \lambda v^2\sigma^2(x) \\ &- \frac{1}{4}\lambda\left(\sigma^2(x) + \eta^2(x)\right)^2 - \lambda v\sigma(x)\left(\sigma(x)^2 + \eta(x)^2\right)\end{aligned} \tag{3.38}$$

The first two terms are kinematic terms, while the two last term are interaction terms. $-\lambda v^2\sigma^2(x)$ is a mass term for the σ particle. There is no such term for the η particle, and it must therefore be massless. Such massless particles are called Goldstone bosons. This causes a problem with the theory, as no such particles has ever been observed.

The *Higgs mechanism*[8] is introduced to solve the conundrum of the massless Goldstone bosons. It can be illustrated using the same fields and Lagrangian as the Goldstone model. This time however, the U(1) symmetry is promoted from a global symmetry, to a gauge (local) symmetry. A gauge boson field A^μ is introduced, and the partial derivative ∂^μ is replaced by the covariant derivative D^μ. Including the term for the free boson field, the Goldstone Lagrangian is now given as

$$\mathcal{L} = D^\mu \phi^*(x) D_\mu \phi(x) - \mu^2 |\phi(x)|^2 - \lambda |\phi(x)|^4 - \frac{1}{4} F_{\mu\nu} F^{\mu\nu} \tag{3.39}$$

If one tries to express ϕ as variations around the minimum, like in eq. 3.37 , a problem arises: The term $gvA^\mu \partial_\mu \eta$ appears in the Lagrangian. It means that A^{mu} and η cannot be interpreted as separate fields. The way around this problem is to exploit the properties of gauge invariance. The field ϕ can also be expressed as

$$\phi(x) = \frac{1}{\sqrt{2}} \left(v + H(x)\right) e^{ig\theta(x)/v} = \phi'(x) e^{ig\theta(x)/v} \tag{3.40}$$

The field $H(x)$ corresponds to radial variations, and $\theta(x)$ to variations along the ring of minima. This looks suspiciously like a gauge transformation. It is if the gauge field A^μ transforms like

$$A^\mu \equiv A'^\mu - \frac{\partial^\mu \theta(x)}{v} \tag{3.41}$$

The gauge chosen by the transformation $\phi \to \phi'$ and $A^\mu \to A'^\mu$ is called the *unitary gauge*. In this gauge, the Lagrangian becomes (omitting the prime in ϕ' and A'^μ)

$$\begin{aligned} \mathcal{L} =& \partial^\mu H(x) \partial_\mu H(x) - \frac{1}{4} F_{\mu\nu} F^{\mu\nu} - \lambda v^2 H^2 + \frac{1}{2} (gv)^2 A_\mu A^\mu \\ & - \lambda v H^3 - \frac{1}{4} \lambda H^4 - \frac{1}{2} v g^2 A_\mu A^\mu H \end{aligned} \tag{3.42}$$

The first line is the free Lagrangian. It contains mass terms for both the $H(x)$ and the A^μ fields. The second line of contain the various interaction terms. The $H(x)$ field, known as the Higgs field, interacts both with itself and the gauge field A^μ. The massless Goldstone bosons are now gone completely, a quite remarkable result. The unphysical degree of freedom, η, has been "eaten" by A^μ. It now corresponds to a longitudinal polarization of the gauge boson.

To break the $\mathrm{SU}(2)_L \times \mathrm{U}(1)_Y$ symmetry of the electroweak theory, the field ϕ must upgraded to a weak isospin doublet. The rest of the process is very similar to

[8] The Higgs mechanism is sometimes known as the Brout-Englert-Higgs mechanism, after the most instrumental scientist behind its inception.

that above. More information can be found in [23]. A consequence of adding this symmetry breaking doublet, is that mass terms appear in the SM Lagrangian for the leptons. A new particle is also gained: The Higgs boson. A particle consistent with the SM Higgs boson was experimentally verified by both the ATLAS and CMS experiments in 2012. The discovery earned Peter Higgs and François Englert the Nobel Prize in physics.

3.8.1 Higgs Production in ATLAS

The two main mechanisms producing Higgs bosons in the ATLAS detector are called gluon-gluon fusion (ggF) and vector boson fusion (VBF). A third mechanism, called associated production is also theoretically possible, but this has not been observed in any experiments. ggF is the dominant Higgs production mechanism at the LHC. It involves two gluons fusing together and through a so-called top loop, radiate a Higgs. A top loop consists of three top quarks connected at three vertices. In principle, all fermions could partake in the process, but the top quark couples much more strongly to the Higgs than the other fermions. In VBF two quarks each radiate a W or a Z boson. The two bosons fuse together to create a Higgs. Leading order Feynman diagrams for both ggF and VBF Higgs production are shown in figure 3.3.

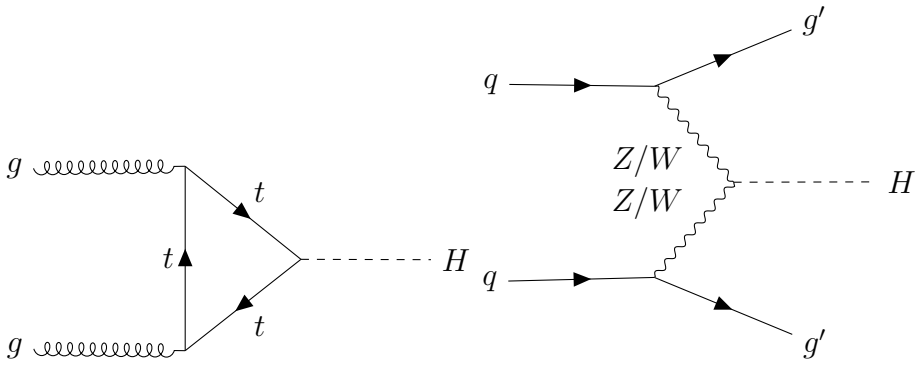

(a) Gluon-Gluon Fusion (b) Vector Boson Fusion

Figure 3.3: Higgs boson production at the LHC

3.9 Shortcomings of the Standard Model

In 1894, the American Physicist Albert A. Michelson, of Michelson and Morley fame, said about the state of physics that "[...] most of the grand underlying principles have been firmly established[...]". Michelson was implying that all that

remained was precise measurement of physical phenomenon. In hindsight, after monumental discoveries of the 20th century, this sentiment might seem laughable. The SM is an extremely successful theory, being in excellent agreement with theoretical predictions. Yet, one must not fall into the same trap Michelson fell into. The SM is far from a complete theory about life, the universe and everything. Listed below are some of the shortcomings of the SM.

Free Parameters

There are a lot of free parameters in the SM. These cannot be predicted theoretically, but must rather be measured experimentally. These free parameters include things like the lepton and heavy boson masses, the Weinberg angle and the various coupling constants.

Baryon Asymmetry

Matter and antimatter are created in roughly equal amount in subatomic interactions. Exactly equal, had it not been for the process known as CP-violation. Performing a charge conjugation and parity transformation that takes a particle to its antiparticle is not symmetric in weak interactions. The ratio of matter to antimatter in the universe after the big bang should have been equal. Something kept the matter and antimatter of the early universe from annihilating. Today there is an abundance ordinary matter in the universe. The effect of CP-violation is not enough to explain this asymmetry.

Gravity

Physicists have yet to come up with a renormalizable quantum field theory of gravity. Marrying Einstein's general relativity and quantum mechanics has yet to succeed.

Generation Problem

It seems completely arbitrary that there should be exactly three fermion generations.

Dark Matter

Astronomical measurements show that ordinary matter, often referred to as baryonic matter, only make up around 4% of the total mass energy in the universe. Around two thirds is dark or vacuum energy while the rest, around 30%, is called *dark matter* [29]. The name dark matter stems from the fact that it does not seem to interact electromagnetically, or at least not very strongly, so that it doesn't give off any light like baryonic matter does. The existence of dark matter is inferred for example when measuring the rotation of galaxies compared to their distribution of luminous matter. We do not yet

know what kind of particle or particles make up dark matter. If SUperSYmmetry (SUSY) is discovered, then the lightest flavours of supersymmetric particles might be good dark matter candidates.

Hierarchy Problem

Also known as the fine tuning problem. The mass of the Higgs boson has been measured to be around 125 GeV. The bare mass of the Higgs is given in eq. 3.42 as $m_H = 2v^2\lambda$. The Higgs mass squared is subject to radiative quantum corrections up to some cutoff energy scale where the SM loses its validity. All the elementary particles interacting with the Higgs boson adds to these corrections. If the cutoff scale is set equal to the Planck Mass scale[9] quantum corrections due to the contribution from fermions are 30 orders of magnitude greater than the bare Higgs mass. Contributions from bosons are of the same magnitude. The fermionic and bosonic contributions seem to cancel each other completely. This requires extreme fine tuning of the masses of the SM particles, which is problematic [30].

Grand Unification

The SM is only assumed to be an effective theory, valid up to a certain energy scale. The coupling constants of the strong force, weak force, and electromagnetism are not really constants at all. They are all dependent on energy scale. Extrapolating to extremely high energies seem to suggest that the coupling constants meet at a single point. Like electroweak theory, all three forces may be unified into a *Grand Unified Theory*. such a unification of coupling constants would not only be aesthetically pleasing, but also reduce the number of free parameters in the SM.

[9]The Planck Mass is defined as $\sqrt{\frac{\hbar c}{G}} \approx 10^{19} GeV$

4 Lepton Flavour Violation

A LFV process is any subatomic process in which $L - \overline{L}$ changes between the initial and final state. The quantum number $L = L_e + L_\mu + L_\tau$ is called the *lepton number* of a particle. $L_{e,\mu,\tau}$ is its lepton family number. The electron and electron neutrino, has electron family number $L_e = 1$. Antileptons and antineutrinos have opposite lepton family numbers. Flavour changing processes in general are not forbidden in the SM; The weak force does not conserve quark flavour in charged current interactions. The quark mixing is governed by the CKM matrix.

The Nobel Prize in physics for 2015 was awarded jointly to Takaaki Kajita and Arthur McDonald for the discovery of neutrino oscillations. This discovery had two major consequences. Firstly, that neutrinos have mass, and second, that lepton numbers are not conserved. This is direct evidence of the existence of LFV. Before the discovery of neutrino mass, the SM did not allow for lepton flavour violating processes at all. The different lepton generations were completely decoupled [31]. Today, neutrino mixing is considered part of the SM. So far, only neutral leptons are shown to violate lepton flavour conservation. Charged Lepton Flavour Violation (CLFV)[1] is heavily suppressed in the SM. This strong suppression of LFV is in part due to the lack of tree level diagrams (simplest diagram in perturbation theory) of any LFV processes, and the fact that higher order diagrams give very small contributions. The latter is due to a process analogous to the Glashow-Iliopoulos-Maiani (GIM) Mechanism[2] [33]. A Feynman diagram of the LFV process $\mu \to e\gamma$ is shown in figure 4.1. A muon converts into a a muon neutrino by radiating a W boson. The muon neutrino then oscillates into an electron neutrino before absorbing the W and emitting an electron. To ensure conservation of momentum, the W radiates a photon. The branching ratio of LFV processes in the SM are of the order $O(10^{-52})$ [34], which are experimentally inaccessible. This makes searches for such processes extremely sensitive to new physics. Detection would be unambiguous proof of BSM physics. conversely, no observation of LFV would constrain the parameters of new physics theories.

[1] From this point, CLFV will be referred to in the text as LFV. Neutrino oscillations will not be discussed further.

[2] The GIM mechanism was developed in 1970 by S. L. Glashow, J. Iliopoulos and L. Maiani. It helped explain the Flavour Changing Neutral Current (FCNC) suppression observed in experiments. Glashow, Iliopoulos and Maiani postulated the existence of the fourth quark, the charm quark, before it was experimentally verified [32] for quarks.

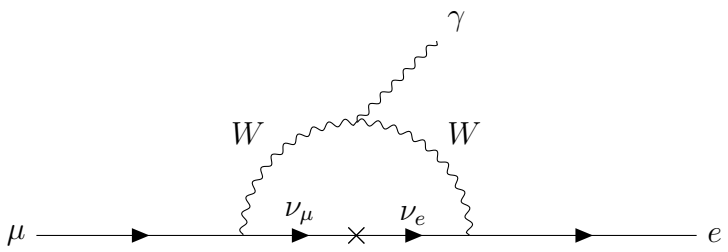

Figure 4.1: Feynman diagram of $\mu \to e\gamma$ decay. This process is allowed to happen in the SM with massive neutrinos, but is strongly suppressed.

The Higgs sector is interesting when it comes to BSM searches. Because of its recent discovery, its properties have not yet been fully tested. Searching for LFV in the Higgs sector is also a way to determine whether or not the Higgs boson discovered is consistent with the SM Higgs. Flavour changing terms in a BSM theory Lagrangian could be of the form

$$\mathcal{L} = -\frac{c_{ij}}{\sqrt{2}} h \bar{l}_L^i l_R^j + h.c., \qquad i,j = e,\mu,\tau \tag{4.1}$$

where h is the Higgs field introduced in the last chapter, while l_L and l_R are left and right handed lepton fields respectively. In the SM the coefficient c_{ij} is given by $c_{ij}^{SM} = \delta_{ij}\sqrt{2} m_i m_j / v$. v is the vacuum expectation value described in section 3.8. It is measured to be 246 GeV. Such couplings would yield flavour changing neutral currents. The form of coupling described in eq. 4.1 are called *Yukawa couplings*. The branching ratio of the process $H \to e\mu$ is strongly constrained by searches for $\mu \to e\gamma$. The current limit of this process is of the order $O(10^{-12})$ [35]. This limit constrains the $e\mu$ coupling constant $c_{e\mu}$, meaning that the $H \to e\mu$ branching ratio must be small as well. $c_{\mu\tau}$ and $c_{e\tau}$ are much less constrained. The $\mu \to e\mu$ bound also limits the products $|c_{\tau\mu}c_{e\tau}|$ and$|c_{\mu\tau}c_{\tau e}|$. This means that if the branching ratio of one of the processes $H \to \tau + \mu$ or $H \to \tau e$ is significantly larger than zero, the branching ratio of the other process will be practically zero. The analysis in chapter 9 searches for $H \to \mu\tau$. The muon should in principle give better separation from the background. A negative result would not reveal any information about the $H \to e\tau$ branching ratio, but a positive result would limit it significantly.

The search for LFV is far from a new frontier in high energy physics. The search for, and lack of positive results, $\mu \to e\gamma$ decays in the 1940's, helped confirm the belief that the muon is a separate particle, and not an excited electron state. The MEGA experiment in the United States, the COMET experiment in Japan, and the MEG experiment in Switzerland, all three focusing on $\mu \to e\gamma$ decay, are three of the most prominent LFV experiments in operation today. The now closed

SINDRUM experiment searched for $\mu \to ee^+e^-$ decays. The branching ratios set for some LFV processes involving muons and taus are shown in figure 4.2[31]. The LHC is so far the only accelerator operating at energies high enough to search for Higgs boson LFV decays.

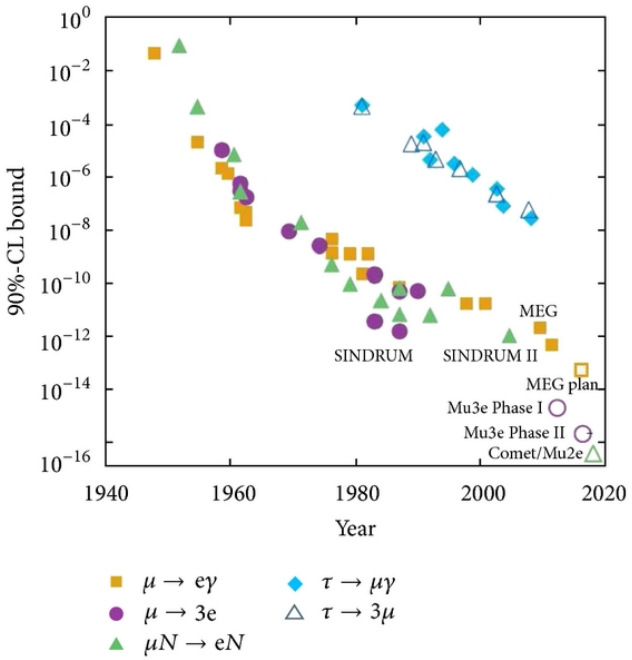

Figure 4.2: Experimental limits of branching ratios in selected muon and tau LFV processes [31]

.

4.1 Supersymmetry

The previous chapter illuminated some of the shortcomings of the SM. SUSY is one of the more prominent theories expanding the SM to solve some of these issues. Much like the theories of the SM, SUSY is based on symmetry. A symmetry between bosons and fermions to be precise. In other word, a SUSY operator Q will convert a bosonic state into a fermionic state and vice versa:

$$Q\,|boson\rangle = |fermion\rangle\,, \qquad Q\,|fermion\rangle = |boson\rangle \tag{4.2}$$

The particles of the theory are arranged into chiral or gauge so-called *supermultiplets*, containing both boson and fermion states. These states are called superpartners. Superpartners have the same electric charge, weak isospin, colour charge and

mass. Being fermions and bosons, they obviously have different spin. It can be shown that all the superpartners of the SM particles are new particles, there is no way to arrange existing fermions and bosons in supermultiplets without introducing a host of phenomenological problems. The Minimal Supersymmetric Standard Model (MSSM) is the SM extension introducing the least amount of new particles. The supersymmetric partners of the fermions are named after their SM partners, prepending an "s" for "scalar" to their name. The spin-0 superpartner of the top quark and the electron for example, are called the stop and selectron. Similarly, SUSY fermions are named by appending "-ino" to the names of their boson SM partners. SUSY particles, or sparticles, are written like their superpartners, but with an added tilde over their symbol. The only odd ball in the MSSM is the Higgs boson. It is not enough to introduce one supermultiplet for the Higgs. Two must be introduced, one up-type and one down-type.

SUSY proves an elegant solution to the hierarchy problem introduced in the previous chapter. Since the Higgs mass loop corrections for fermions and bosons are of opposite sign, the superpartners cancels each others contributions exactly.

It is stated above that the sparticles have exactly the same mass as their SM superpartners. This cannot be the case, as such particles would have been discovered already. SUSY must therefore be a broken symmetry. The masses of the sparticles are in principle free parameters. However, for SUSY to provide a solution to the hierarchy problem, these masses cannot be much greater than the electroweak scale. The mass of the lightest superpartners are often estimated to be on the TeV scale. The mechanism for breaking SUSY is required to be so-called *soft* symmetry breaking to not destroy the solution to the hierarchy problem [30]. SUSY breaking is considered to be broken in a so-called hidden sector of particles, with no direct coupling to the sparticles. The particles of the hidden sector are either singlets under the SM symmetry groups, or too heavy to be detected in experiments. So-called messenger fields are responsible for communicating the symmetry breaking to the MSSM.

The nature of dark matter may also be hiding within SUSY. The lightest sparticle may be stable, and is thus a candidate for dark matter. These should obviously not interact through the electromagnetic interaction. Direct dark matter searches also suggest that they should not interact via the strong interaction. These particles are often called Weakly Interacting Massive Particles (WIMPs). SUSY also suggests a solution to the problem of matter/antimatter asymmetry in the universe. Breaking SUSY can introduce additional CP-violating phases other than those already present in the SM.

4.1.1 LFV in SUSY

SUSY theories in which the principle of Grand Unification is applied, meaning that the running coupling constants of the forces meet at some large energy scale, are called SUSY-GUTs. In some SUSY theories, especially SUSY-GUTs, the slepton mass matrix is made diagonal in flavour space at the GUT-scale. This is done to avoid too large LFV. Radiative corrections introduce off-diagonal terms when going from the GUT-scale to the electroweak mass scale. These terms greatly increase the expected branching ratio of LFV processes. The strength of the LFV branching ratios are heavily dependent on which SUSY theory is applied. The Feynman diagram of $\mu \to e\gamma$ in a SUSY-GUT model based on a SU(5) symmetry is shown in figure 4.3. The diagram looks similar to that of the SM diagram in figure 4.1, but with the intermediate states being sparticles. In this theory only right handed sleptons, the superpartners of leptons, are subject to flavour mixing. In general, left-handed sleptons may also mix flavours. It is important to note that that the handedness of the selectron $\tilde{e}_R$ and smuon $\tilde{\mu}_R$ does not refer to their own chirality, but rather that of their SM superpartners. The expected branching ratio of $\mu \to e\gamma$ in one such SUSY-GUT model has been calculated to lie between $\times 10^{-13}$ and $\times 10^{-15}$ [31].

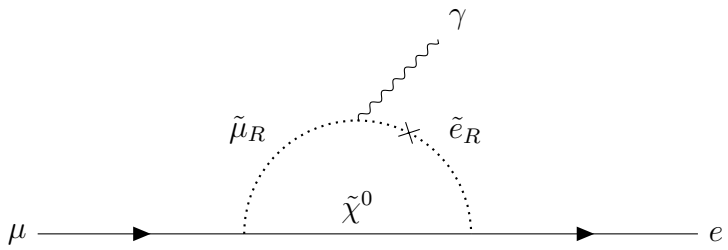

Figure 4.3: Feynman diagram of $\mu \to e\gamma$ decay in a SUSY-GUT model.

SUSY models not only introduce LFV, the rates of LFV processes are often unacceptably large. This problem is called the *flavour problem* in SUSY, and can be solved by introducing a new symmetry called *R-parity*. The R-parity of a particle is defined as

$$R \equiv (-q)^{3(B-L)+2s} \tag{4.3}$$

L is lepton number, B is baryon number and s is the spin of the particle. Standard model particles and sparticles have R-parity R=1 and R=-1 respectively. R-parity ensures that there is no mixing between SM particles and SUSY particles. Other flavour issues, like unstable protons, also emerge, but are not solved by introducing R-parity.

As far as Higgs LFV decays goes, the most promising decay channel seems to be $H \to \tau\mu$. With a total integrated luminosity of 100 fb^{-1} as much as 5×10^2 such events could be produced [36]. This is achievable through so-called slepton mixing.

4.2 Other Theories

SUSY might be the most well known theory predicting detectable branching ratios of LFV decays, but it is not the only one. Some alternate BSM theories and mechanisms are listed below.

Froggatt-Nielsen mechanism

The Froggatt-Nielsen mechanism was introduced to explain the mass hierarchy of quarks and charged leptons. In it, the lepton generations are symmetric under a global U(1) flavour symmetry. This symmetry is broken, much like in the Higgs mechanism, by a flavour field gaining a vacuum expectation value (VEV). This mechanism has some interesting features: It may help explain the matter/antimatter asymmetry in the universe by introducing so-called leptogenesis. It may also give a significant contribution to the branching ratio of LFV processes [37].

Composite Higgs Models

Composite Higgs models postulates that the newly discovered Higgs boson is not an elementary particle. Rather it is comprised of smaller particles, like the quarks in hadrons. Like SUSY, Composite Higgs models provides a solution to the Hierarchy Problem. The Higgs boson is thought to be analogous to a bound QCD system. The Hierarchy Problem disappear in QCD because of asymptotic freedom. Composite Higgs models predicts the existence of excited Higgs states at around 1 TeV, which could be discovered at the LHC. In Composite Higgs models, couplings between the Higgs constituents and fermions could increase LFV branching ratios [38].

The Randall-Sundrum scenario

Some BSM models try to solve the Hierarchy Problem by introducing the existence of higher dimensions. The Randall-Sundrum model introduces an extra dimension compactified into an *orbifold*[3]. This dimension has two 4D boundaries. At one boundary the visible 4D universe is located. Gravity is located on the other. Introduced in the theory is a new scalar particle called the *radion*. The radion may have LFV decays on at least one loop level in

[3]From "orbit-manifold". An orbifold is the generalization of a manifold, a topological space.

some SM extensions. The branching ratio of these decays may be as high as order $O(10^{-}8)$ [39].

5 Simulation and Computation Tools

This chapter aims to give an introduction to some of the software tools used when analysing data from the ATLAS detector, and to detail the various steps taken when simulating physics processes in the detector.

5.1 Monte Carlo Simulations

The output from the ATLAS detector would only be of limited use if we didn't have simulated datasets to compare it to. The signals observed in the detector can be identified as specific processes by matching them to simulations. These simulations can be used to estimate errors, and determine efficiencies and sensitivities of the tools used in the analysis. By comparing different event selection criteria for signal and background simulations, the signal to background ratio of our analysis can be improved. To simulate the physical processes inside particle colliders we often need to perform complex multi-dimensional numerical integrals. Monte Carlo (MC) is first and foremost a numerical integration tool. It is in essence a generalization of area calculation. Take as a simple example the task of calculating the area of a country on a map: Make a random point on the map and ask if the point is outside or inside of the border of the country. Repeat this procedure a number of times. By the Law of Large Numbers, the number of points inside the border, divided by the number of points on the map tends towards the area of the country. This can be generalized to higher dimensions. When applied to particle physics, the random numbers represents quantum mechanical "choices" of the system. One of the main advantages of using the Monte Carlo method rather than other methods of numerical integration is that the error of MC is proportional to the reciprocal of the square root of N, the number of trials. This is better than any other method in large dimensions. MC can be further improved by not generating random points in space uniformly, but rather one that more closely follows the function being generated. This requires some knowledge of said function of course, which we do not always have.

5.1.1 Event Generators

The software programs responsible for creating MC simulations are called *event generators*. Event generators are used not only to calculate the hard, perturbative processes in the detector, but also soft processes, like hadronization. There are a lot of event generators to chose from, and they are often specialized to generate specific tasks or steps in the simulation process. These steps are illustrated in figure 5.1

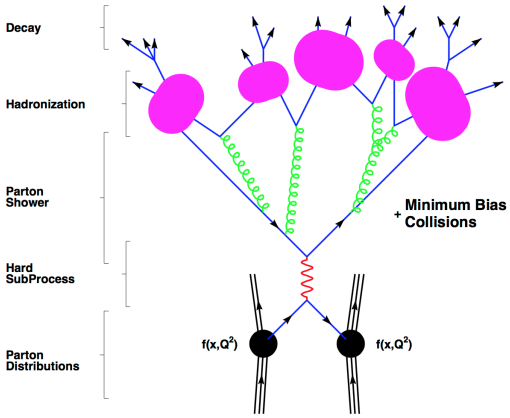

Figure 5.1: The basic structure of a generator event, including showering and hadronization [40]

When simulating a proton-proton collision, one starts with the hard scattering process between two partons in the protons. this can be between two gluons or a quark/antiquark-pair. The probability of the different partons to take part in the process is determied by Parton Distribution Functions (PDFs). PDFs define the probability density of finding a particle in a given momentum interval at a given resolution. PDFs cannot be predicted theoretically, but has to be determined experimentally. The outgoing particles from the initial scattering are then split into parton showers. These showers then hadronize to form colour neutral hadrons. If these hadrons are unstable on the detector scale, they are decayed further. In addition to the hard process, so-called underlying structures of the event are generated. The partons interacting in the central process only carry a fraction of the total proton momentum. The coloured *beam remnants* are simulated. They will in most cases travel parallel to the beam pipe and hadronize downstream. beam remnants and their interactions are called the underlying event. In real colliders, the protons does not arrive at the interaction point in neat pairs, but rather in bunches of a several billion protons at a time. At every bunch crossing in the LHC, there are on average 20 collision events. The events that occur, other than

the one being studied, are called minimum bias events, or pileup, and must also be included in simulations. It is also possible that more than one pair of partons in the colliding protons interact. This is called multiple parton interactions.

5.1.2 Detector Simulation and Event Reconstruction

Event generators output energy, momentum and various quantum numbers of the particles generated in the event. This is of limited use in analysis however. We need to simulate the response of the detector when the generated particles pass through it, and the physics objects put out by the ATLAS reconstruction algorithms. The simulation must accurately describe detector occupancy and background. The simulation should ideally be able to handle particle energies as low as 10 eV, which is the ionizing potential of the active gas in various gaseous detectors. This is impractical however, so the actual energy range used are between 10 keV and 10 TeV.

The software tool used to simulate the detector response is Geant4 (G4) [41]. A complete and accurate 3D model of the ATLAS detector, with information about the materials used, is constructed in G4. The response of the various subdetectors as various particles flow through the detector is simulated. This includes deflection in magnetic fields, scattering with detector material, cascading in calorimeters, charge carriers freed in semiconductor detectors, and more. Expected energy deposits in the calorimeters and hits in the tracking detectors are registered. Through a process known as *digitization*, these hits are converted into the output format of the detector, so that it can be reconstructed like real detector measurements.

The reconstruction algorithms work in two stages: First, standalone reconstruction is performed in the various subdetectors. Second, the information from all the subsystems are gathered and used to reconstruct the final measurements and to identify the various physical objects [42].

Detector simulation is very time consuming. Some times, to achieve the required amount of events to do a proper statistical analysis, it is not possible to do a full detector simulation in G4. In such cases we want to give up some accuracy in exchange for faster running time. It could also be desirable to only do a full simulation in certain regions, or for certain particles. To mimic the effects of the simulation process and the effects of digitization, one can take the four-momenta put out by the event generator, and apply a smearing. The resolution of this smearing must be determined in experiments. Atlfast-II is a software package created to perform this task. Almost 80% of the full simulation time, is spent modelling particle showers in the calorimeters. Atlfast-II decreases the simulation running time by an order of magnitude by using the calorimeter simulation tool FastCaloSim [43].

A schematic representation of the various steps in the ATLAS Monte Carlo production chain can be seen in figure 5.2.

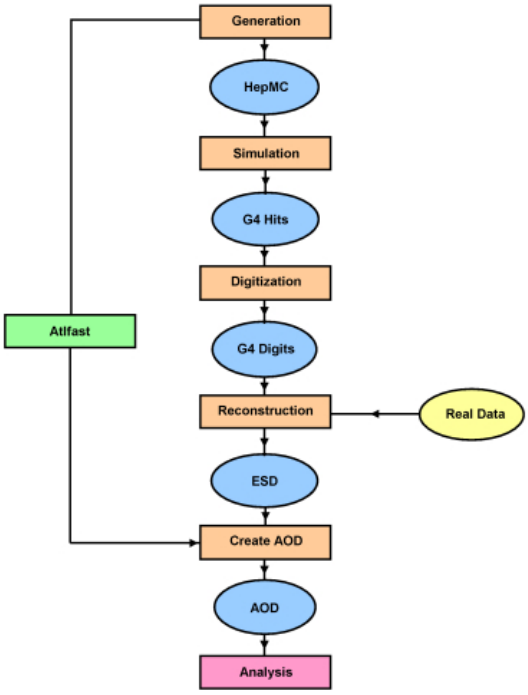

Figure 5.2: ATLAS Monte Carlo production chain [44].

5.2 The Grid

In chapter 2 we mentioned the large amount of data recorded at the LHC. Even with the reduction in rate achieved using the trigger system, there is still a lot of data generated to be stored and analysed. The LHC Worldwide Computing Grid, often called simply the Grid, was created in 2002 to perform these tasks. The Grid is a global network of computers and storage systems. It is made up of 170 computer centres in 42 countries around the world, making it the largest computing network of it's kind. There are a lot of advantages to distributing the computing efforts like this. Datasets can be stored in multiple locations around the globe, ensuring easy access for scientists independent of their geographic location. Risk is minimized when there is more than one single point of failure. Data becoming corrupted at one site, or the site going offline for a period, does not shut the down Grid activity as a whole. There are also a host of practical and sociological reasons for distributing the LHC computational systems in this way [45].

Grid users upload their computational tasks to the grid in the form of Grid jobs. These jobs can be moving datasets between storage, performing analyses, slimming large datasets to suit their needs, or any other tasks needed. Tasks requiring large amounts of processing power can be split up into several jobs, utilizing the power of parallel processing to reduce running time significantly.

5.3 The Athena Framework

A software framework is a set of skeleton software that provides the most needed functionalities for the task at hand. It prevents a lot of code to be rewritten at the start of every new project. Having a common approach simplifies cooperation on projects with a lot of collaborators, and makes it easier to get aquainted with the code when joining a project. The Athena[1] framework is used by the ATLAS to perform simulation and analysis. Athena interfaces the various steps in the ATLAS production chain(figure 5.2), and simplifies the MC simulation process. Athena is controlled using so-called job options, python scripts that pass instructions about what algorithms to run, specifies output and input files and so on.

5.4 Simulated $H \to \tau\mu$ Samples

For this thesis, to study the $H \to \tau\mu$ process, lacking central ATLAS MC productions, a small set of MC samples were generated. The process was also used as training exercise for the author to get familiar with Athena and the Grid. Events were generated for both of the two main production mechanisms for Higgs bosons in ATLAS, ggF and VBF. Mass of the Higgs bosons generated was set to 125 GeV. The hard event was generated using the event generator Powheg. Showering and hadronization was performed using Pythia. To conserve time, Atlfast-II was chosen over Geant4 for the detector simulation. Though this decreased the simulation running time significantly, generating even a modest number of events still required running the production on the Grid. Minimum-bias events were added to simulate pileup in the detector.

5.5 C++ and Python

The two programming languages Python and C++ are ubiquitous in high energy particle physics and is what is used in this thesis as well. C++ is a compiled programming language based on C. A C++ script has to be compiled by a compiler

[1] Athena is the greek goddess of wisdom, war, the arts, industry, justice and skill. She was born fully grown from Zeus' forhead.

every time the code changes, but it also runs very fast once compiled. With low level functionality such as direct memory manipulation, C++ is flexible and robust, but has a somewhat steep learning curve. C++ includes object-oriented programming features, such as inheritance. Unlike C++, Python is a more high level programming language, making it more user friendly. Python is an interpreted language, meaning that it doesn't need to be compiled. This makes Python code a bit slower than C++ code, making it less suited for computationally intensive tasks. The Athena framework is scripted in Python.

5.6 ROOT

ROOT is an object-oriented framework developed at CERN by René Brun and Fons Rademakers at CERN in the 90's [46]. Based on C++, it has built in tools for statistics, mathematics and plotting. ROOT consists of two parts, the ROOT libraries and the CINT interpreter. CINT makes it possible to run root scripts without compiling. The ROOT libraries contain tools to facilitate physics analysis, like tools for big data processing, plotting and statistical analysis.

PyROOT is a Python module that enables the Python interpreter to interact with the ROOT libraries. It can be a useful tool for user less familiar with the syntax of C++.

6 The Tau Lepton

Reconstruction and identification of muons in the ATLAS detector is straight forward. Long lifetime and high penetration of detector material give them a very distinct signature. Tau identification is more involved. Because of its high mass, 1777 GeV, the tau has a very short lifetime. The tau decay length, 87 μm, lies inside the LHC beam pipe. Direct observation of taus are therefore impossible, and it must be inferred from its decay products. The sensitivity of many physics processes depend on the quality of tau reconstruction. This chapter covers some of the methods used to reconstruct and correctly identify taus in the ATLAS detector.

6.1 Tau Decay and Topology

Due to its high mass, the tau is the only charged lepton able to decay hadronically, meaning that it decays into a final state of quarks. Hadronic decays make up approximately 65 % of the total tau decay width. When taus decay hadronically, they produce jets. Separating these jets from the QCD multijet background of the LHC poses a challenge. There is a lot more QCD background than tau jets from interesting physics processes present at the LHC. The ubiquitous presence of neutrinos in tau decay further complicate the process of reconstruction.

The most common tau decay modes are listed in table 6.1. Leptonic decay modes, in which the tau decay to a muon or an electron, are common, making up around 35 % of the total decays. Identifying taus decaying leptonically is challenging because of the short tau decay length. Charged leptons produced in the original proton collision or from secondary tau decays are hard to separate. The analysis in chapter 9 only considers hadronic tau decays, often denoted τ_{had}.

As can be read of table 6.1, most of the tau decay modes have low multiplicity of charged particles, usually one or three. Decays with one charged track is called a one-prong decay, while those with three tracks are called three-prong decays. Five prong decays occur, but in less than one percent hadronic tau decays. Even numbers of charged tracks are of course impossible due to charge conservation. A lot of the tau decay final states contain neutral pions π^0. 98.8 % of the time[18], neutral pions decay to a pair of photons. This gives tau jets a strong electromagnetic component. In one prong decays, neutral pions carry more of the total jet energy than in three prong decays. The electromagnetic component is therefore

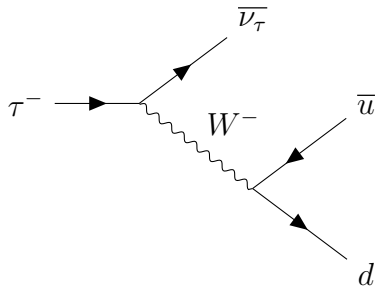

Figure 6.1: Feynman diagram of one prong hadronic tau decay. The d and $\overline{u}$ form a π^-

larger in one prong decays. Tau jets are also characteristically narrow.

An example Feynman diagram of a hadronic tau decay can be seen in fig 6.1. A negatively charged tau converts into an anti-tau neutrino through radiating a W^- boson. The W then decay into a quark/antiquark pair, forming a negative pion π^-.

Decay mode	Branching Fraction [%]
$\pi^\pm\pi^0\nu_\tau$	25.51 ± 0.09
$e\nu_e\nu_\tau$	17.85 ± 0.05
$\mu\nu_\mu\nu_\tau$	17.36 ± 0.05
$\pi^\pm\nu_\tau$	10.91 ± 0.07
$\pi^\pm 2\pi^0\nu_\tau$	9.29 ± 0.11
$3\pi^\pm\nu_\tau$	9.00 ± 0.06
$3\pi^\pm\pi^0\nu_\tau$	2.70 ± 0.08
$h^\pm\omega\nu_\tau$	1.99 ± 0.08
$\pi^\pm 3\pi^0\nu_\tau$	1.04 ± 0.07
others	≈ 6

Table 6.1: Tau branching ratios [18]. $h^\pm$ denotes any charged boson(π^+, K^- etc.)

6.2 Reconstruction and Identification

The first step of reconstructing a tau is simply recognizing the jet itself in the detector. This is achieved using the anti-k_t algorithm [47]. These jets are then used as "seeds" for the tau identification algorithms. A jet being considered as a tau is called a tau candidate. To be considered a tau candidate a jet must have a transverse momentum of over 10 GeV and fall within $|\eta| < 2.5$ in the ATLAS tracking system.

Three different methods for tau identification are used in ALTAS: Cut-based selection, projected likelihood identification and identification using Boosted Decision Trees (BDTs). Projected likelihood methods are not discussed further. Each method separates the candidates passing the identification requirement into three categories: Loose, medium and tight. These categories correspond to signal efficiencies of approximately 60%, 45% and 30%, respectively [48]. The variables used to discriminate tau jets from QCD background are listed below [49]. They quantify the properties of tau jets covered above.

Electromagnetic Radius

The width of the tau jet in the electromagnetic calorimeter, weighted by transverse energy. Defined as

$$R_{EM} = \frac{\sum_{i=1}^{\Delta R<0.4} E_{T_i} \Delta R_i}{\sum_{i=1}^{\Delta R<0.4} E_{T_i}} \tag{6.1}$$

i runs over cells in the three first layers of the EM calorimeter. E_{T_i} is the transverse energy measured in cell i. ΔR is defined as

$$\Delta R = \sqrt{(\eta - \eta_{cluster})^2 + (\phi - \phi_{cluster})} \tag{6.2}$$

η and ϕ are the coordinates of the calorimeter cell in question. $\eta_{cluster}$ and $\phi_{cluster}$ are the calorimeter cell defining the center axis of the tau cluster.

Track radius

The width of the jet weighted by track p_T. Defined as

$$R_{track} = \frac{\sum_{i}^{\Delta R_i<0.4} p_{Ti} \Delta R_i}{\sum_{i}^{\Delta R_i<0.4} p_{Ti}} \tag{6.3}$$

Like for the EM radius, ΔR is measured from the tau seed axis.

Number of Isolation Tracks

The *core* of the tau candidate jet is defined as $\Delta R < 0.2$ from the jet axis. Charged tracks within the jet core determine if the tau decay is one- or three-pronged. The range $0.2 < \Delta R < 0.4$ from the jet axis is known as the jet isolation annulus. The number of charged tracks in this cone N_{track}^{iso} is used as a background discrimination variable.

Leading Track Momentum Fraction

How much of the total transverse momentum of the tau jet carried by the most energetic charged track.

$$f_{track} = \frac{p_T^{track}}{p_T^{\tau}} \tag{6.4}$$

Core Energy Fraction
Fraction of the total transverse energy of the tau candidate contained within $\Delta R < 0.1$ of the jet axis.

$$f_{core} = \frac{\sum_i^{\Delta R_i<0.1} E_{Ti}}{\sum_i^{\Delta R_i<0.4} E_{Ti}} \tag{6.5}$$

EM fraction
The fraction of transverse energy measured in the EM calorimeter. This is interesting because of the strong electromagnetic component of tau jets mentioned earlier.

$$f_{EM} = \frac{\sum_i^{\Delta R<0.4} E_{Ti}^{EM}}{\sum_i^{\Delta R<0.4} E_{Ti}} \tag{6.6}$$

Cluster Mass
The invariant mass computed from the calorimeter clusters of the tau jet.

Track Mass
Invariant mass computed from the tracks of the tau jet.

Transverse Flight Path Significance
The significance of the transverse decay length to the secondary vertex(where the tau decayed).

$$S_T = \frac{L_T}{\delta L_T} \tag{6.7}$$

L_T is the length in the transverse plane to the secondary vertex, while δL_T is its estimated uncertainty.

Leading Track Path Significance
The significance of the transverse distance of closest approach from the reconstructed primary vertex.

$$S_T^{track} = \frac{d_0}{\delta d_0} \tag{6.8}$$

Corrected Cluster Isolation Energy The transverse energy of isolated clusters in the calorimeter. Isolated means that the clusters lie in the range $0.2 < \Delta R < 0.4$ from the jet axis.

$$E_{T,corr}^{iso} = E_T^{iso} - \delta E_T^{iso} \tag{6.9}$$

The term δE_T^{iso} is added to correct for pileup effects. It is defined as

$$\delta E_T^{iso} = (1 - JVF) \times \sum p_{T.track} \tag{6.10}$$

JVF is the jet vertex fraction of the tau candidate and $\sum p_{T.track}$ is the sum of transverse momentum of the tracks associated with that jet.

6.2.1 Cut-Based Identification

The simplest approach to tau identification is a cut-based approach. This method recognizes taus by cutting on R_{EM}, R_{track}, f_{track}, N_{track}^{iso}, $E_{T,corr}^{iso}$ and S_T^{flight}. "Cutting" means to discard a candidate that does not meet some requirement on one or more of its variables. The cuts vary based on the multiplicity of tracks in the jet and its transverse momentum. Tighter cuts on R_{EM} and R_{track} can be applied for higher momentum jets. This is due to the so-called *shrinking cone effect*, stating that the jet becomes more collimated at higher energies. The cuts applied are different for one- or three-pronged candidates.

6.2.2 Boosted Decision Trees

If a tau candidate fails one of the cuts of the cut-based method, it is classified as background. However, many events do not have all the characteristics of either signal or background. For example, a true tau may not pass some criteria due to a measurement error, or a background event may closely mimic a tau jet by pure chance. A BDT method does not immediately discard candidates that fail a cut. The BDT method is based on binary decision trees, an example of which can be seen in fig. 6.2. The tree applies cuts in a recursive manner. The candidate starts at the "root" of the tree, and depending on whether or not it meets some criteria, is sent down one of two possible "branches" to a new node. At the new node a new cut is made on some other discriminating variable. This is repeated until some stopping criteria is met. The tau candidates are now arranged into "leaves". The amount of signal and background candidates in each leaf determines whether or not it is a signal or background leaf. This must be determined by studying CM generated events, so that the true tau candidates are known. Leaves should ideally be pure signal or pure background.

What makes the decision tree "boosted", or weighted, is the recursive method used to build them. Start with unweighed events and a decision tree. If an event is misidentified, a signal event ending up in a background leaf, it gains a weight. After all the events has been classified a new decision tree is constructed using the weights from the first run. This recursive procedure is known as "training" the BDT. One must be careful not to overtrain the BDT. No two distributions are

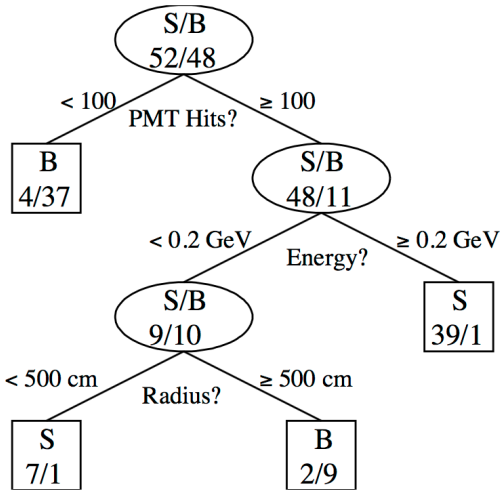

Figure 6.2: Example decision tree[50].

the same. If the method is trained to much it picks up too much of the statistical fluctuations of the training sample. A lot of trees may be built this way. The jets fed into the BDT algorithm is passed through all the trees. When the candidates end up on a signal leaf it is given a score of +1(signal-like) and when it ends up on a background leaf it is given a score of -1(background-like). The renormalized sum of these events, possibly weighted, is used as the final score [50].

The discriminating variables used for BDT tau identification method in ATLAS is all the variables mentioned in the previous section, except N_{track}^{iso}. One- and three-prong tau decays have different training of the decision trees. A comparison of the efficiency and misidentification percentage of the cut-based and the BDT method can be seen in table 6.2. The cut-based approach seems to be slightly more efficient. however, the misidentification rate is rather high compared to the BDT method. In the analysis in chapter 9, taus are identified using the BDT method.

Tau ID Method	Efficiency	Mis-ID Probability
Cut-Based Loose	$0.87 \pm 0.02 \pm 0.02$	0.221 ± 0.008
Cut-Based Medium	$0.79 \pm 0.02 \pm 0.03$	0.081 ± 0.007
Cut-Based Tight	$0.65 \pm 0.02 \pm 0.03$	0.025 ± 0.006
BDT Loose	$0.81 \pm 0.02 \pm 0.03$	0.085 ± 0.008
BDT Medium	$0.63 \pm 0.02 \pm 0.03$	0.029 ± 0.006
BDT Tight	$0.42 \pm 0.01 \pm 0.03$	0.012 ± 0.004

Table 6.2: Efficiency and misidentification probability for cut-based and BDT-based tau identification methods [48]. The statistical uncertainty is given first, followed by the systematic uncertainty in the efficiency. Only statistical uncertainty is given for the misidentification probability.

7 The Boost Method

This chapter detail a method of reconstructing the CM of heavy resonances whose decays involves taus. Because of their high mass, around 1.78 GeV, τs decay very rapidly. They can therefore not be measured directly in detectors, but must be inferred from its decay products. This is non-trivial however, because of the presence of one or more neutrinos, depending on the final state, in the decay process. Neutrinos are too weakly interacting to be detected in ATLAS. Detection of neutrinos requires huge, purpose built detectors. Thus, to reconstruct the mass frame of a Higgs boson decaying into a pair of τs, one must take the visible decay products measured in the detector and use some kind of estimation process to adjust for the information lost due to the neutrinos.

7.1 Other Existing Methods

7.1.1 Visible Mass

The simplest mass variable to calculate, is the *visible mass* of the system. The visible mass is calculated by taking the invariant mass of the visible decay products. Invariant mass is the same in all reference frames, and is a characteristic of the energy and momentum in a system. For a system of n particles it is defined as:

$$M = \sqrt{\left(\sum_{i}^{n} E\right)^2 - \left(\sum_{i}^{n} \boldsymbol{p}\right)^2} \tag{7.1}$$

In the systems rest frame invariant mass is simply equal to its energy. If the system is moving the momentum has to be subtracted. Between two particles, invariant mass is found by calculating the product of their four-momentum vectors.

Visible mass has quite a broad distribution. The sensitivity of so-called "bump-hunting" methods in mass distributions depends strongly on how narrow the mass distribution is compared to the background. Simply studying the visible mass might therefore not be enough to find a weak signal, like any LFV process is likely to be.

7.1.2 Collinear Approximation

The *Collinear Approximation* is an improvement to simply plotting the invariant mass of the visible decay products. This method also uses the information about missing transverse energy, E_T^{miss}, and is used to calculate the invariant mass of systems decaying into two taus. The method relies on the assumption that the tau decay products are *collinear* with the tau itself, meaning that they travel in the same direction. Using this assumption, as well as information about E_T^{miss}, the four-momentum of the mother taus can be calculated. Deconstructing the mother tau momenta into its visible and invisible components yields:

$$P_1^\tau = P_1^{jet} + P_1^{miss} \tag{7.2}$$
$$P_2^\tau = P_2^{jet} + P_2^{miss} \tag{7.3}$$

The assumption that E_T^{miss} is collinear with the tau jet means that P^{miss} is equal to P^{jet} times some constant:

$$P_1^{miss} = c_1 P_1^{jet} \tag{7.4}$$
$$P_2^{miss} = c_2 P_2^{jet} \tag{7.5}$$

Furthermore, if we assume that E_T^{miss} is only due to neutrinos P_1^{miss} and P_2^{miss} have to satisfy

$$P_T^{miss}1 + P_T^{miss}2 = E_T^{miss} \tag{7.6}$$

Substituting 7.5 into 7.6 and dividing E_T^{miss} into its x- and y-components yields two equations with two unknown constants c_1 and c_2 to be determined:

$$c_1 P_{1x}^{jet} + c_2 P_{2x}^{jet} = E_{Tx}^{miss} \tag{7.7}$$
$$c_1 P_{1y}^{jet} + c_2 P_{2y}^{jet} = E_{Ty}^{miss} \tag{7.8}$$

Solving for c_1 and c_2 yields:

$$c_1 = \frac{E_{Ty}^{miss} P_{1x}^{jet} - E_{Tx}^{miss} P_{1y}^{jet}}{P_{2y}^{jet} P_{1x}^{jet} - P_{2x}^{jet} P_{1y}^{jet}} \tag{7.9}$$
$$c_2 = \frac{E_{Ty}^{miss} P_{2x}^{jet} - E_{Tx}^{miss} P_{2y}^{jet}}{P_{1y}^{jet} P_{2x}^{jet} - P_{1x}^{jet} P_{2y}^{jet}} \tag{7.10}$$

Substituting this into 7.3 and calculating the invariant mass of P_1^τ and P_1^τ gives the approximate mass of the original resonance, for example a Higgs, that decayed into the two taus.

The Collinear Approximation has some drawbacks. For instance, it is not applicable to all events. If the two tau jets are back-to-back, the method fails. This is due to the fact that E_T^{miss} cannot be projected onto two vectors lying on the same line. This means that there are no unique solutions to c_1 and c_2. In these cases the missing energy from the neutrinos cancels each other out. To use the Collinear Approximation one thus has to eliminate events with such a back-to-back configuration of the taus.

In the $H \to \mu + \tau$ case, there is only one neutrino involved in the decay. In this case the Collinear Approximation simplifies quite a bit. To reconstruct the mass, simply project the missing transverse energy onto the visible tau products and take the invariant mass of the resulting four vector and the muon. The equation for the four-momentum of the tau becomes

$$P^\tau = P^{jet} + E_T^{miss} / \cos\theta \tag{7.11}$$

where θ is the angle between the tau jet and the transverse plane.

7.1.3 Transverse Mass

Another mass reconstruction method is to reconstruct the *Transverse Mass*. Transverse mass is defined as the invariant mass of the visible decay products and E_T^{miss} of a process. For a H decaying into a $\tau^+\tau^-$ pair, transverse mass is defined as

$$\begin{aligned} M^2 &= m_{\tau_1}^2 + m_{\tau_2}^2 + 2\sqrt{m_{\tau_1}^2 + P_{\tau_1}^2}\sqrt{m_{\tau_2}^2 + P_{\tau_2}^2} \\ &+2E_T^{miss}\sqrt{m_{\tau_1}^2 + P_{\tau_1}^2} + 2E_T^{miss}\sqrt{m_{\tau_2}^2 + P_{\tau_2}^2} - 2\left(\boldsymbol{P_{\tau_1}} \cdot \boldsymbol{P_{\tau_2}} + \boldsymbol{P_{\tau_1}} \cdot \boldsymbol{E_T^{miss}} + \boldsymbol{P_{\tau_1}} \cdot \boldsymbol{E_T^{miss}}\right) \end{aligned} \tag{7.12}$$

where P_{τ_1} and P_{τ_2} are the momenta of the visible tau decay products, and m_{τ_1} and m_{τ_2} are their masses. The transverse mass offers good separation from QCD backgrounds with fake tau signatures. Unlike the Collinear Approximation, transverse mass can be calculated for all events. If E_T^{miss} is omitted from the calculation, the resulting quantity is called *reduced mass*.

7.1.4 Effective Mass

Another mass variable used for tau pairs is called effective mass. It is defined as the invariant mass of the taus and missing transverse energy:

$$M_{eff} = \sqrt{(p_\tau^1 + p_\tau^2 + p_T^{miss})^2} \tag{7.13}$$

where p_T^{miss} is the four vector of the missing transverse energy.

7.1.5 Missing Mass Calculator

The Missing Mass Calculator (MMC) is a sophisticated method for mass reconstruction. Unlike the Collinear Approximation, which assumes that the neutrinos in the tau decays are collinear with the tau decay products, the MMC makes no assumptions on the direction of the neutrinos in the decay. This increases the number of unknowns required to solve for to reconstruct the event increases from two to between six and eight, depending on the decay mode of the taus. The system now becomes under-constrained. However, not every solution to the problem is equally probable. Additional knowledge about τ decay kinematics can be used to separate the more likely solutions from the less likely ones. This informations is supplied in the form of probability density functions [51].

The MMC eliminates the long tail at high energies that appears in the Collinear Approximation. This can be seen in figure 7.1. One drawback of using the MMC is that the method has to be trained to the specific process being studied. The MMC probability density functions used to study $H \to \tau^+\tau^-$ decays at 8 TeV at the LHC can not be applied to the same process at 13 TeV. The MMC can also be modified to account for just one tau in the boson decay. This has been done for the LFV analysis studying run-1 LHC data, but is not yet tuned for the Run 2 collision energy.

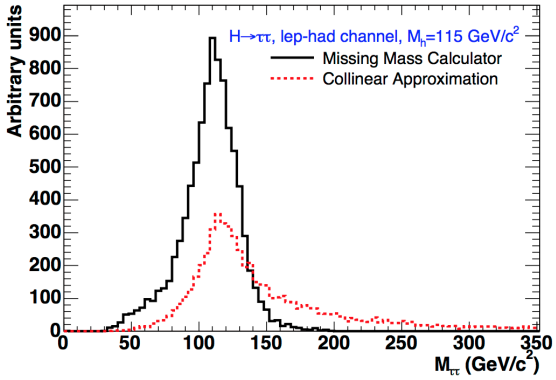

Figure 7.1: Performance of the MMC.[51]

7.2 The Boost Method

Take as an example a Higgs boson decaying into a $\tau^+\tau^-$-pair. As mentioned previously, reconstructing the rest frame of the Higgs is in principle not possible. There is however, a reasonable assumption we can do, that gives us some information about the undetectable neutrinos: For a sufficiently massive particle decaying, such as the Higgs, the direction of the visible tau decay products, the tau jets, are expected to be close to that of the tau itself. This is the same assumption made for the Collinear Approximation. We define the *acollinearity* of the two taus as the angular deviation from being back-to-back. Thus, if we Lorentz boost[1] the taus such as to minimize the acollinearity, this Lorentz boost should be a good approximation of the mass frame of the Higgs, the frame in which the Higgs is at rest.

At the LHC, Zs and Higgses produced through the ggF mechanism have a high boost along the beam direction, also known as the z-direction in the ATLAS coordinate system. In a lot of cases the transverse Lorentz boost of the Higgs can therefore be assumed to be small. The H rest frame can be be estimated by finding the boost that minimizes the acollinearity between the tau jets along the z-direction. This method of only Lorentz boosting along the z-axis will be referred to as the Z-method. The Z-method does not need information about the direction of the H, and thus does not use E_T^{miss}.

If one has information about the direction of the H before decaying one can search for the transverse component of the boost as well. The direction of the H is found by summing up the missing transverse energy, E_T^{miss}, of the event as well as the four-momenta of the tau jets. In this case on first determines the boost along

[1] A Lorentz boost is a linear coordinate transformation between two reference frame moving at a constant velocity relative to each other.

the beam axis, followed by a new minimization procedure along the transverse direction of the H. This method of of Lorentz boosting in both the longitudinal and transverse directions will be referred to as the XYZ-method. The acollinearity has unique minima for both the longitudinal and the transverse boost. Since the direction of the taus are expected to be close to parallel to the beam pipe, except for in VBF production, the XYZ-method is only expected to perform slightly better than the Z-method.

The Boost Method was developed at the University of Bergen, and the case of a Z or Higgs decaying to a $\tau^+\tau^-$-pair is explained in detail in [52].

Unlike the other methods mentioned so far in this chapter, the Boost Method is not strictly speaking a method for mass reconstruction, but rather one of CM-reconstruction. Once the rest frame is found the task of finding the mass of the particle still remains. For the $H \to \tau\tau$ process mentioned previously, the invariant mass of the two taus will naturally peak below the true H mass, due to the energy lost to neutrinos. However, if one plots twice the energy of the leading tau, there seem to be a kinematic edge in the invariant mass distribution, around the H mass. This kinematic edge can be seen in figure 7.2. This is not unexpected; due to conservation of momentum, each tau will carry away half of the Higgs' energy. In the LFV case, the muon will be *monochromatic* in the Higgs CM, meaning that they are all expected to have the same energy. A distinct peak should be seen by plotting twice the energy of the muon in the CM. This peak should coincide with the mass of the Higgs, as the muon is carrying half the Higgs energy.

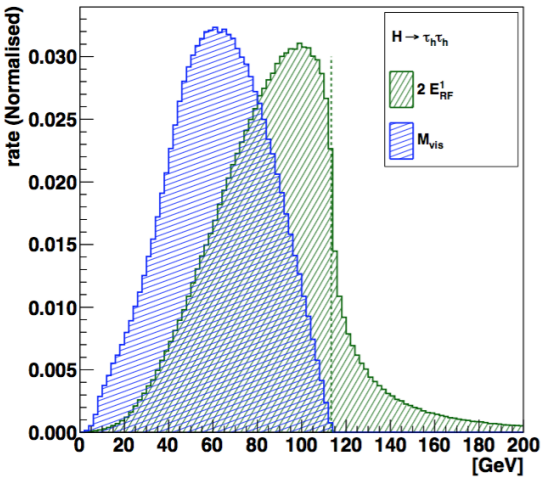

Figure 7.2: 2E of leading energy tau in the H rest frame.[52]

One benefit of using the Z-method, is that it doesn't require E_T^{miss}. This makes it useful in cases when E_T^{miss} isn't well known. When plotting the Boost Method

against the visible mass, which can be seen in figure 7.3, the two variables does not seem to be strongly correlated. The method is showing promise as a complimentary method for mass reconstruction of events involving neutrinos. In the next chapter the Boost Method is put to the test using a simulated $Z \to \tau + \mu$ events.

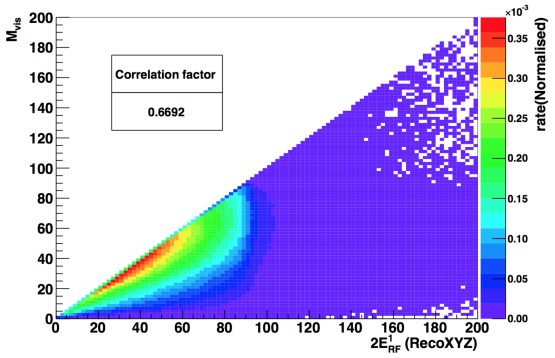

Figure 7.3: Mass reconstructed using the XYZ-method (Boost Mass) plotted against the visible mass in simulated $Z^0 \to \tau^+ + \tau^-$ events.[52]

7.2.1 Spin

Due to conservation of momentum, the energy spectra of two taus in the CM frame of the decaying particle will be different depending on its spin. This effect can be seen when plotting the energy correlation between the visible tau energies of a $H \to \tau\tau$ and a $Z \to \tau\tau$ sample in the rest frame reconstructed using the Boost Method (figure 7.4).

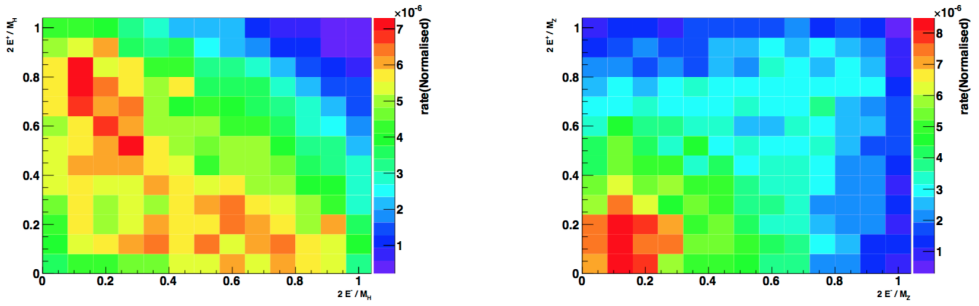

(a) Spin 0 (H sample). (b) Spin 1 (Z^0 sample).

Figure 7.4: Comparing energy correlation in the CM frame reconstructed using the XYZ-method for a $H \to \tau\tau$ and a $Z \to \tau\tau$ sample [52]

This information could be useful for background separation in an analysis involving

Higgs bosons. The background of the LFV $H \to \mu\tau$ analysis in chapter 9 has significant background from Zs.

8 Z $\rightarrow \mu\tau$ Mass Reconstruction Study

in this chapter the Boost Method is compared to other mass reconstruction methods. This is done to determine its usefulness in an LFV search. Various methods for mass reconstruction are considered, and background separation strategies are explored. The reason for studying Z bosons over Higgs bosons is due to a lack of $s = \sqrt{13}$ TeV MC simulation samples at the time of the study.

8.1 Samples

The dataset used to test the method is Monte Carlo simulations of proton-proton collisions at $s = \sqrt{13}$ TeV, producing Z bosons, which decay into a muon and a tau, violating lepton flavour conservation. The taus decays hadronically in the simulation. 13 TeV is the current collision energy at the LHC. The samples, containing just under 190 000 events, were produced by the ATLAS production team using the techniques detailed in chapter 5. The event generators used are Pythia8 and EvtGen, and full G4 detector simulation is performed.

The background samples used in section 8.5 are produced in the same production campaign as the signal sample, *mc15*. Events generators used are Powheg, Pythia8, EvtGen and Photospp. Full G4 detector simulation is perfomed. In the $Z \rightarrow \tau\tau$ events, one of the hadrons are required to decay hadronically, while the other decay leptonically.

The samples are stored in Derived Analysis Object Data (DAOD) files. This file format contains the reconstructed physics objects from the ATLAS detector. Using a framework like Athena, one can do phyiscs analysis on DAOD files directly. however, the files can be rather large and cumbersome, as they contain a lot of variables. For this study it is more convenient to trim the files down to size a bit, discarding some of the unnecessary variables. This is done using the xTauFrameWork (xTauFW), developed by the ATLAS HLeptons group. The xTauFW run over the DAOD-files, producing ROOT files known as *n-tuples*. The physics objects in the n-tuples are stored as floats in lists known as trees. Histograms of the variables can be studied quickly using a ROOT TBrowser.

8.2 Boostmethod

In the $H \to \tau^+\tau^-$ case of the previous chapter, one of the methods proposed for reconstructing the H mass was to plot twice the energy the leading energy tau, followed by determining the position of a kinematic edge in the plot (Figure 7.2). If we plot the same for the LFV Z-sample (Figure 8.1), the distribution looks much different. Instead of a sharp drop around the mass of the Z, the distribution peaks around the Z mass, and displays a rather long tail at high energy. The distributions are fitted with a simple Gaussian distribution in a mass window 15 GeV over and under the Z mass of 91 GeV.

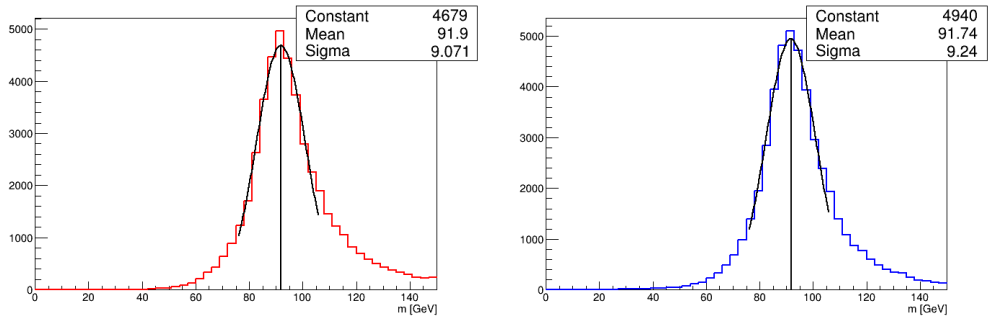

(a) Z-method (b) XYZ-method

Figure 8.1: Two times the leading energy lepton in the Z CM. The Z-method refers to the direction of the Lorentz boost used in the Boostmethod, and not the Z boson.

An alternative mass variable, mentioned in the previous chapter, is to take twice the energy of the muon in the Z CM as the Z mass. If the CM was reconstructed correctly, the muon carries away half the Z energy. These distributions, seen in figure 8.2, seem to peak slightly below the true Z mass. The method does away with the large tail at high mass of the previous method, but seems to underestimate the mass, and has a slightly wider distribution.

Figure 8.3 show the invariant mass of the muon and tau in the Z CM with E_T^{miss} projected onto the tau jet before boosting. Like for the method plotting twice the muon energy, this distribution seem to underestimate the Z mass. It also has the widest distribution of the Boost Method mass variables considered.

FWHM is a common measure of the width of a peak in a distribution. It is defined, as the name suggests, as the width of the distribution at half the height of the peak. For a gaussian distribution, FWHM is given as $2\sqrt{2\log 2}\sigma \approx 2.36\sigma$, where σ is the standard deviation of the distribution. To give ouselves the best possible chance of separating the LFV signal from background the mass

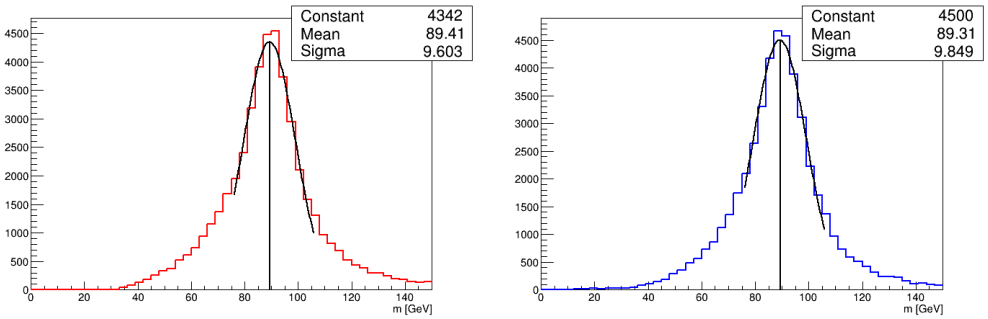

(a) Z-method (b) XYZ-method

Figure 8.2: Two times the muon energy in the Z CM.

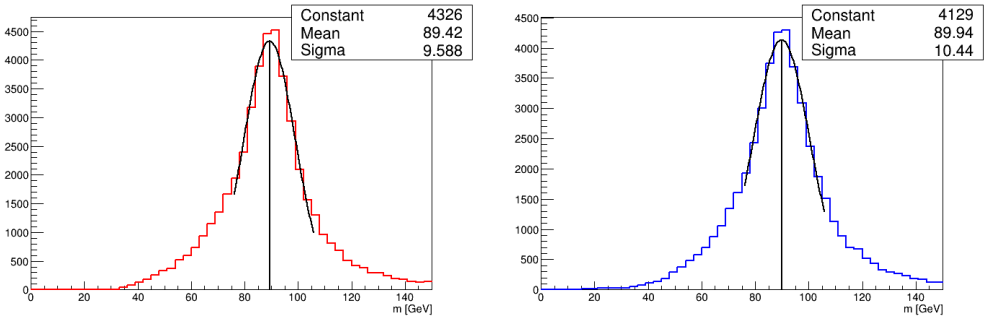

(a) Z-method (b) XYZ-method

Figure 8.3: Invariant mass of muon and tau in Z CM. E_T^{miss} projected onto tau four-momentum before boosting.

peak should be as narrow as possible. FWHM for the mass discriminant methods suggested in this section are listed in table 8.1. The method taking twice the energy of the leading energy lepton in the CM as the Z mass seem to have the best performance, despite its high energy tail. Note that the Z-method seems to be performing better than the XYZ-method. This seems counterintuitive. Section 8.3 tries to investigate why this is the case.

In figure 8.4, the Boost Method is compared to some of the mass reconstruction variables mentioned in the previous chapter. The effective mass, defined in the previous chapter, does not seem to work very well at all.

If two methods of mass reconstruction are not strongly correlated, one should be able to combine them in a way that improves overall mass resolution. This was attempted using the Boost Method and the (modified) Collinear Approximation, mentioned in the previous chapter. The resulting mass distribution can be seen in figure 8.5. The boostmass is taken as twice the leading energy lepton in the Z

	FWHM Z-Method	FWHM XYZ-Method
Leading Energy	21.4	21.8
2 Times Muon Energy	22.6	23.2
Invariant Mass	22.6	24.6
Hybrid Method	-	22.6

Table 8.1: FWHM of the fitted mass distributions. FWHM = 2.36σ, where σ are standard deviations of the gaussian fits to the mass distributions.

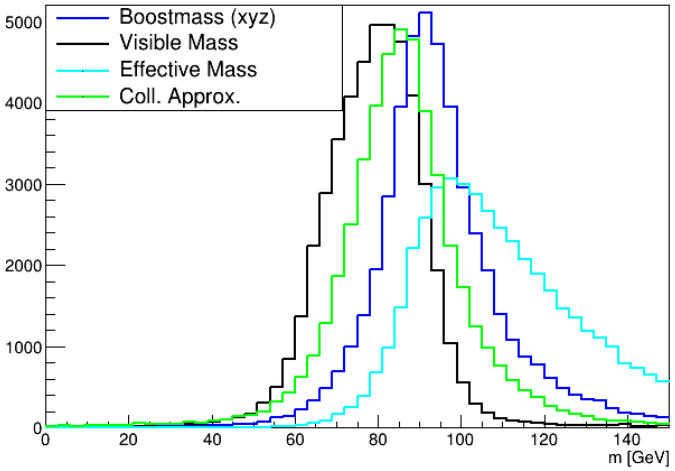

Figure 8.4: Boost Metod Z mass compared to other mass reconstruction methods.

CM, found using the XYZ-Method. Like in the previous section, the distribution is fitted with a gaussian. FWHM is measured as 22.6. This is worse than the Boost Method alone. This widening is probably due to the difference in mass the two variables predict. The collinear approximation seems to underestimate the Z mass slightly (figure 8.4). This method does do away with the high mass tails seen in some of the previous plots. Although it does not have the narrowest distribution, the peak of the hybrid method is significantly higher than for the other methods. The FWHM test is not good at reflecting this.

Last chapter a claim was made that the Boost Method mass is not strongly correlated to visible mass. This is checked by plotting the two variables against each other (figure 8.6).

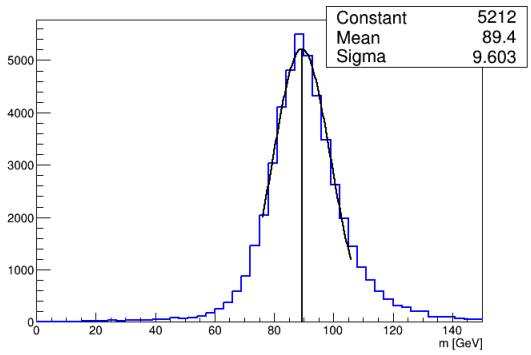

Figure 8.5: Mean of Collinear Approximation and Boost Method

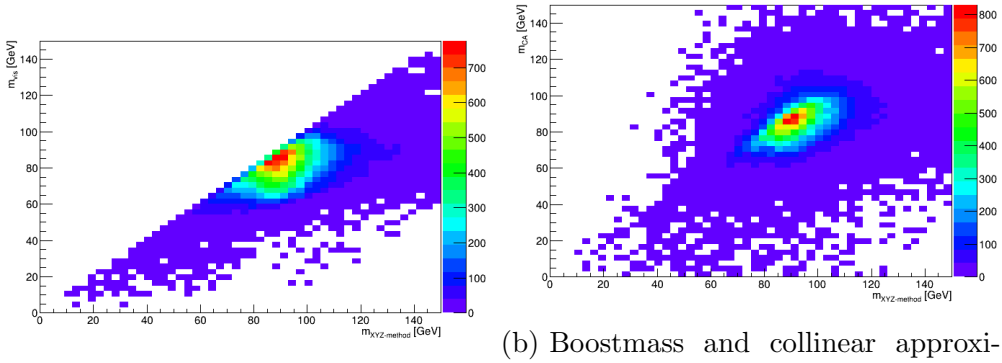

(a) Boostmass and visible mass

(b) Boostmass and collinear approximation mass

Figure 8.6: Boost Method Z mass plotted against visible mass and Collinear Approximation mass.

8.3 Kinematics and Topology

This section aims to study the kinematics and topology of the Z samples to determine if there are selections that can be made to improve the mass resolution using the Boost Method. Since it was shown to have the narrowest distributions, the mass is taken as twice the leading lepton energy.

The plots shown in this section are so-called profile plots. Profile plots are an alternative to two-dimensional scatter plots. The plots are displayed as a normal histogram, where the height of the bins are the mean of the distribution in the Y-direction. Error bars are the standard deviation of the mean, $s_i/\sqrt{n_i}$ (s_i is the standard deviation of bin i, and n_i is the number of events in said bin).

Plotting the Z mass against the magnitude of the boost vector used in the Boost Method(figure 8.8) and the polar angle of said vector (figure 8.7), there does not

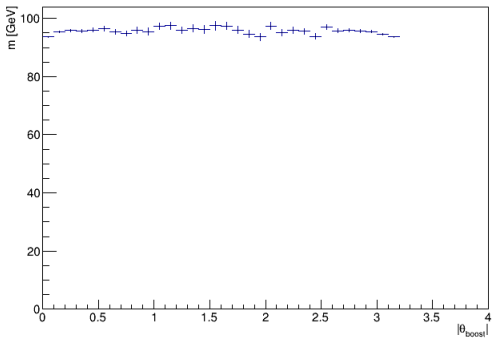

Figure 8.7: Z mass as a function of boost polar angle.

seem to be any noticeable dependency.

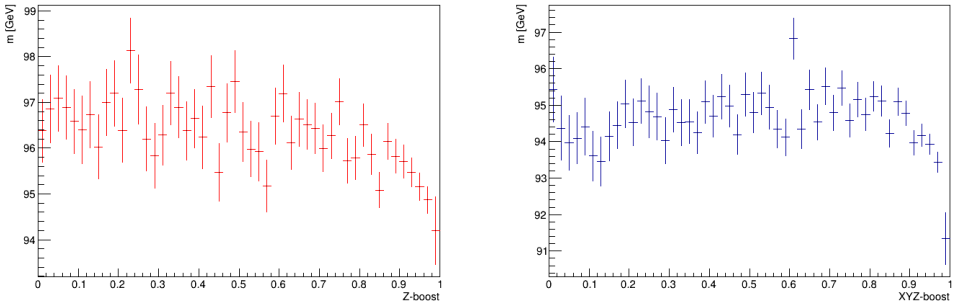

(a) Z-method (b) XYZ-method

Figure 8.8: Z mass as a function of boost magnitude

Comparing the Z mass with the kinematics of the event, a strong dependence on the transverse momentum p_T of the muon and tau emerges (figure 8.9 and 8.10). This is maybe not surprising, considering how the mass is estimated. This proportionality seem to taper off for large values of p_T for the XYZ-method.

Good angular separation between the tau and muon is a reasonable requirement to make. Overlapping objects can cause problems with measurements and reconstruction. From figure 8.11 it is clear that the Boost Method Breaks down for small values of ΔR.

The magnitude of E_T^{miss} (figure 8.12) is not expected to have an impact on the Z-method, as this is not used to calculate the boost along the z-direction. There seem to be a dependence on E_T^{miss} for the XYZ-method however. This could be due to the direction of E_T^{miss} being hard to determine at low values.

The Z- and XYZ-method both seem to break down when the separation between

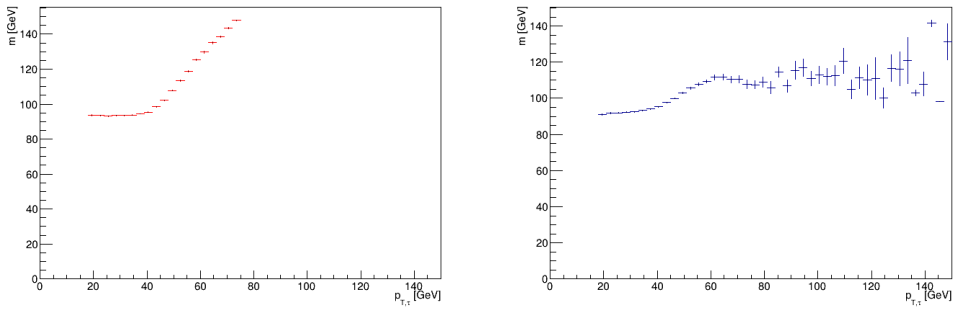

(a) Z-method (b) XYZ-method

Figure 8.9: Z mass as a function of tau p_T

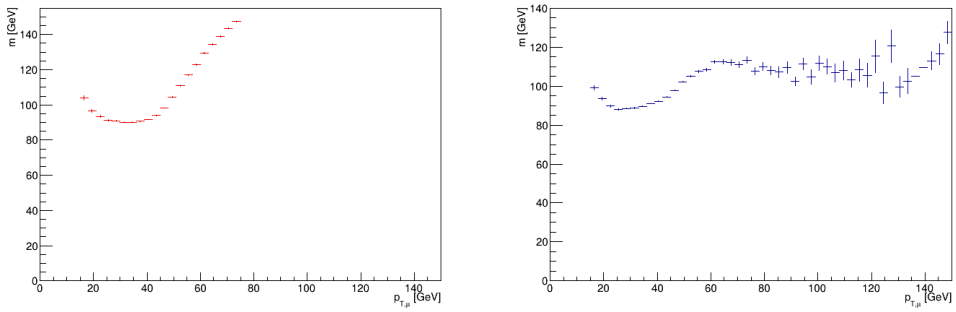

(a) Z-method (b) XYZ-method

Figure 8.10: Z mass as a function of muon p_T

the muon and tau becomes greater than 2. This is apparent from figure 8.13.

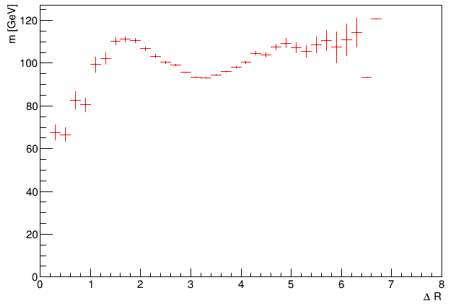

(a) Z-method

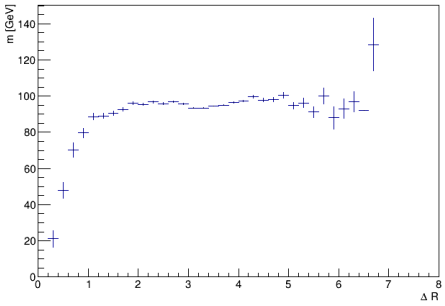

(b) XYZ-method

Figure 8.11: Z mass as a function of ΔR

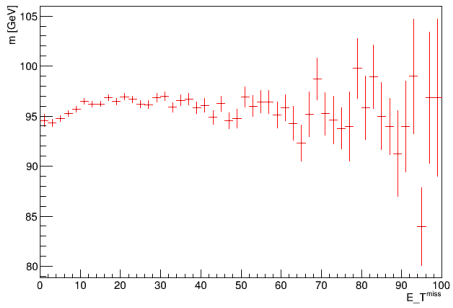

(a) Z-method

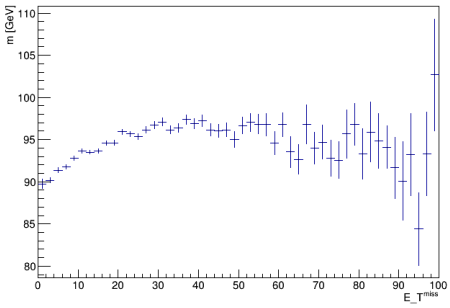

(b) XYZ-method

Figure 8.12: Z mass as a function of E_T^{miss}

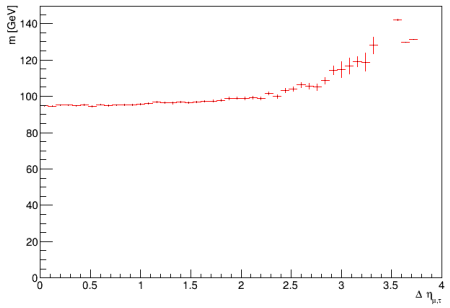

(a) Z-method

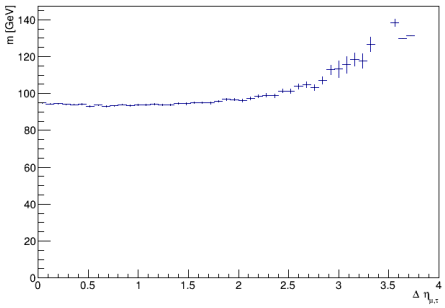

(b) XYZ-method

Figure 8.13: Z mass as a function of $\Delta\eta_{\mu,\tau}$

8.4 Improving Transverse Boost Component of XYZ-method

The XYZ-method for determining the Z CM is shown above to be worse than that for the Z-method. Something fails in the calculation of the transverse component of the Lorentz boost to the CM. Results from the previous section suggest that this is due to the direction E_T^{miss} being poorly defined at low values.

One solution may be to simply omit the direction of E_T^{miss} when determining the direction of the transverse boost component. The resulting mass distributions are shown in figure 8.14. The FWHM values for these distributions are listed in table 8.2. The E_T^{miss} dependence seen before are now completely gone, but the Z mass is somewhat underestimated.

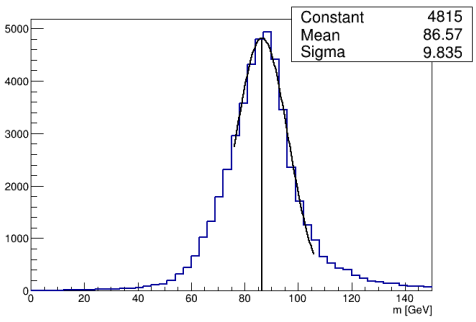

(a) Leading energy

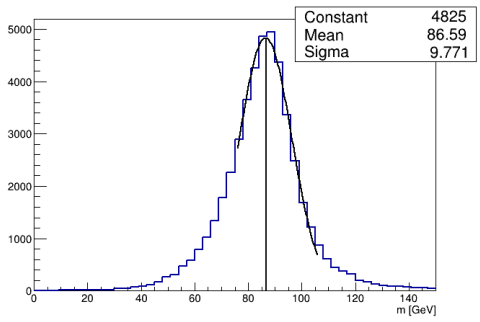

(b) Two times muon energy

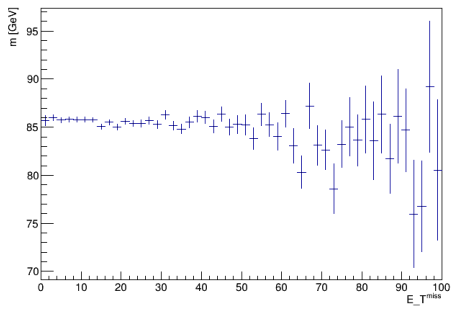

(c) Z mass as a function of E_T^{miss}

Figure 8.14: Removing E_T^{miss} from transverse boost direction calculation.

Alternatively, since the direction of E_T^{miss} is assumed to be poorly defined at low values, the E_T^{miss} momentum vector could be rotated such that it is parallel to the transverse component of the tau jet momentum vector. This may be a reasonable thing to do. After all, for the Boost Method to be valid at all, the tau and the neutrino are assumed to be approximately parallel. The transverse

boost component is then calculated as before. The resulting mass distributions are shown in figure 8.15. The E_T^{miss} dependence in the Z mass remains, and the Z mass is now overestimated.

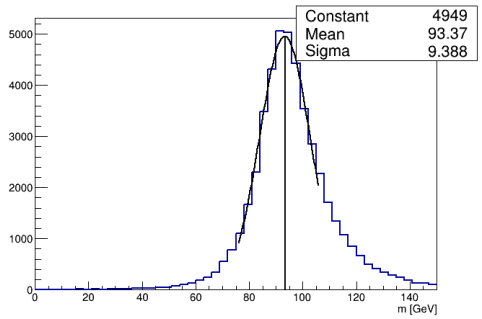

(a) Leading energy

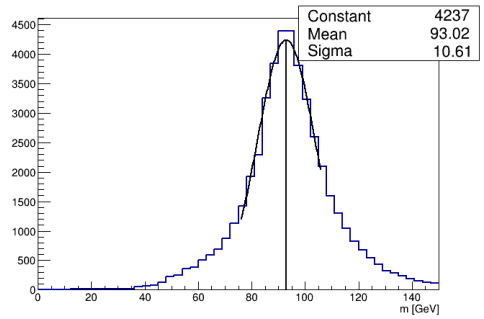

(b) Two times muon energy

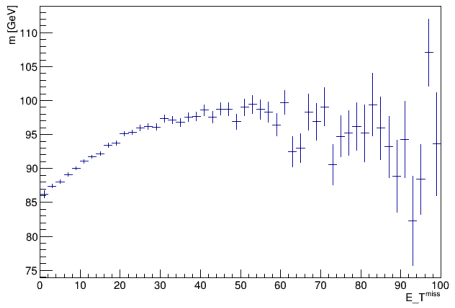

(c) Z mass as a function of E_T^{miss}

Figure 8.15: Rotating E_T^{miss} parallel to tau jet direction before calculating transverse boost direction.

Another proposed improvement is to introduce some E_T^{miss} dependent correction terms in the mass calculation. A second order polynomial correction term would take the form:

$$M_{Z,corr}^{boost} = M_Z^{boost} + A + BE_T^{miss} + C(E_T^{miss})^2 \tag{8.1}$$

Setting the parameters by eye to $A = 3$, $B = -0.3$ and $C = 0.003$ does away with the E_T^{miss} dependence in Z mass. This kind of tuning to known kinematic effects is similar to the approach taken by the MMC, mentioned in the previous chapter. Improved tuning could probably increase the resolution, but overall the corrections does not seem to have too large of an effect on the FWHM.

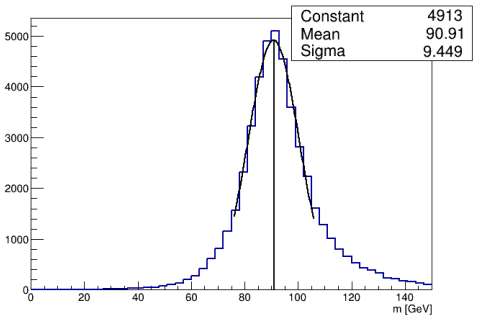

(a) Leading energy

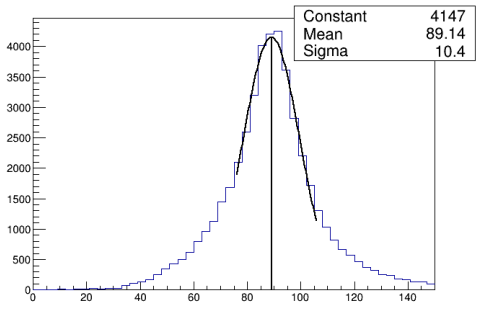

(b) Two times muon energy

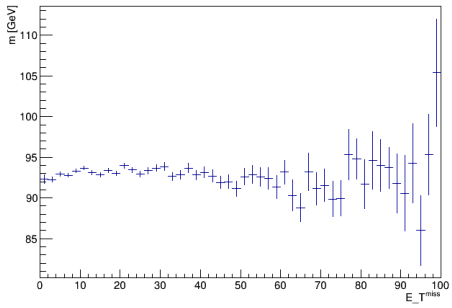

(c) Z mass plotted against E_T^{miss}

Figure 8.16: Boostmass corrected for E_T^{miss} effects

	FWHM 2 x Muon E	FWHM Leading Energy
Remove E_T^{miss}	23.0	23.2
Rotate E_T^{miss}	25.0	22.1
E_T^{miss} correction	24.5	22.3

Table 8.2: FWHM of suggested improvement methods.

8.5 Background

The limit of the $Z \to \mu\tau$ branching ratio was measured in the ATLAS detector to be 1.7×10^{-5} [53]. For such a rare process, separating the signal from the background processes is of the utmost importance. The processes $Z \to \tau\tau$ and $Z \to \mu\mu$ are expected to contribute significantly to the background. The $Z \to \tau\tau$ process might mimic the signal if one of the taus decay hadronically while the other decay leptonically into a muon. The short tau decay length makes it hard to determine if the muon originated from the original decay or from a secondary decay vertex. In the $Z \to \mu\mu$ case, one of the muons may combine with a pileup jet or a jet from the underlying event to mimic the signal. Other processes also contribute to the background, the production of a W boson plus one or more jets, or QCD multijet background for example, but these are not covered in this study.

Two methods for background separation are proposed here, both taking advantage of the fact that if all the missing transverse energy in the event is due to the neutrino from the tau decay, E_T^{miss} should be more or less parallel to the transverse direction of the tau jet. The first method is to cut on the transverse mass obtained by combining the tau and E_T^{miss} or the muon and E_T^{miss}. The distributions of these variables are plotted against each other in figure 8.17. Calculating the transverse mass is covered in the previous chapter. The signal events are concentrated at low values of $m_T(\tau, E_T^{miss})$ and between 40 and 50 GeV in $m_T(\mu, E_T^{miss})$. By cutting around this region, a lot of the $Z \to \tau\tau$ and $Z \to \mu\mu$ background can be eliminated.

In the signal sample, missing energy is expected to be close to parallel to the tau jet. Plotting the azimuthal angle between the tau jet and E_T^{miss}, and between the muon and E_T^{miss}(figure 8.18), this seems to be the case. In the background distributions however, the missing energy is sometimes parallel to the muon candidate. This happens especially often in the $Z \to \tau\tau$ case. The background can thus be reduced by requiring the angle between the transverse component of the tau and E_T^{miss} to be small.

The distributions in figures 8.17 and 9.5 are suspected to be strongly correlated. The $\Delta\eta$ correlation plots are therefore remade, while imposing a cut on the transverse masses. It can be seen from plot (c) in figure 8.17 that selecting events with $M_T(\mu, E_T^{miss}) > 30$ GeV and $M_T(\tau, E_T^{miss}) < 20$ GeV will keep most of the signal and discard a significant fraction of the background. The resulting plots can be seen in figure 8.19. From looking at these plots it is apparent that using one method of background rejection will remove most of the events that would have been removed by the other. Using both methods in unison will yield diminishing returns in terms of background rejection.

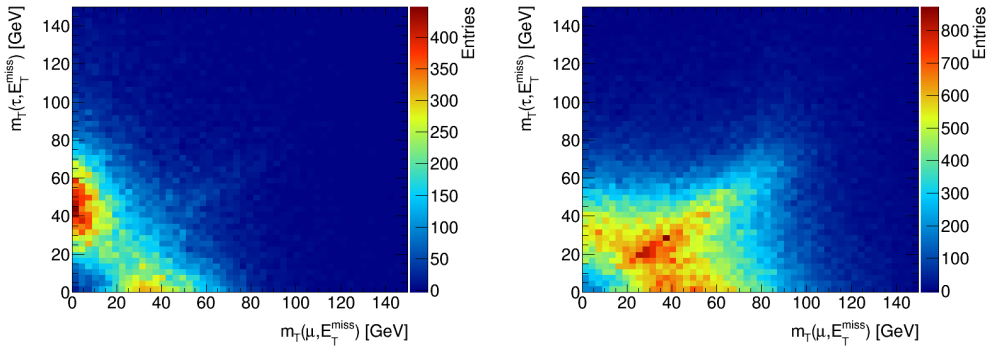

(a) $Z \to \tau\tau$ Background

(b) $Z \to \mu\mu$ Background

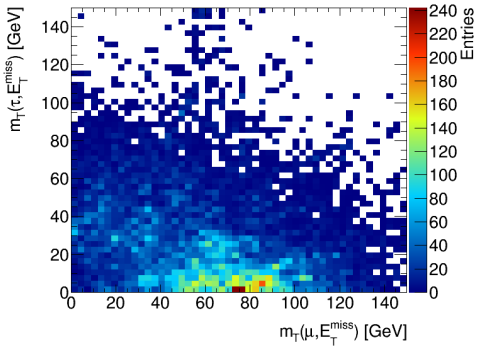

(c) $Z \to \mu\tau$ Signal

Figure 8.17: Two-dimensional scatter plots of $\tau + E_T^{miss}$ and $\mu + E_T^{miss}$ transverse mass distributions.

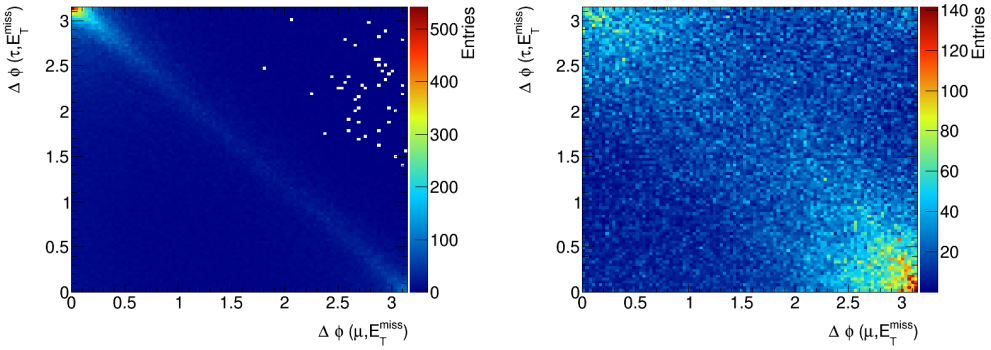

(a) $Z \to \tau\tau$ Background (b) $Z \to \mu\mu$ Background

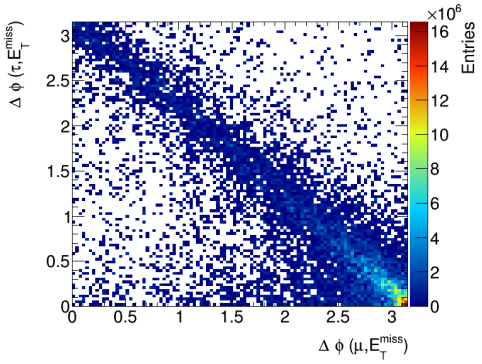

(c) $Z \to \mu\tau$ Signal

Figure 8.18: Two-dimensional scatter plots of the azimuthal angle between the muon and E_T^{miss}, and between tau and E_T^{miss}.

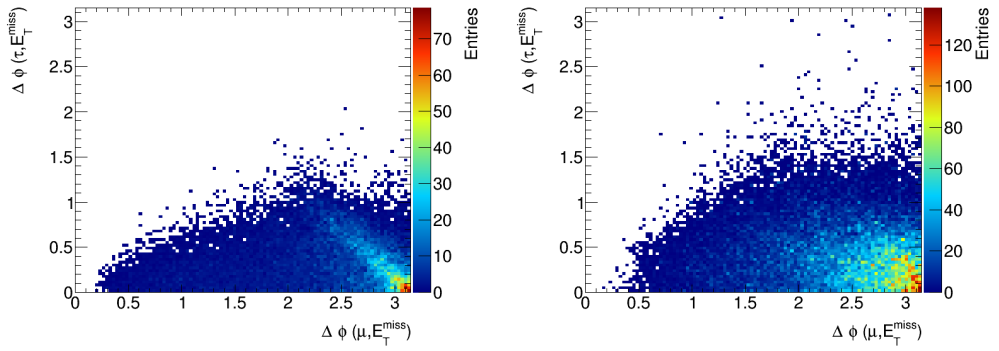

(a) $Z \to \tau\tau$ Background

(b) $Z \to \mu\mu$ Background

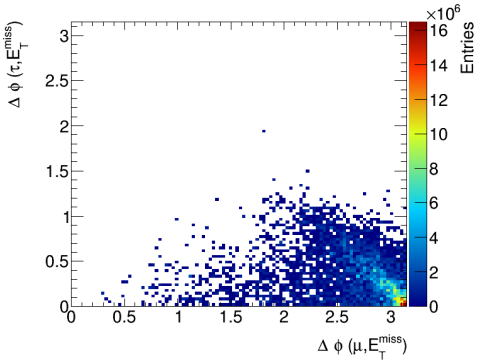

(c) $Z \to \mu\tau$ Signal

Figure 8.19: Two-dimensional scatter plots of the azimuthal angle between the muon and E_T^{miss}, and between tau and E_T^{miss}. Imposing cuts in the transverse mass distributions shown in figure 8.17. Cutting on the transverse mass assures that the angular separation between the tau and E_T^{miss} is small.

8.6 Summary and Outlook

Compared to the mass reconstruction variables mentioned in the previous chapter, the Boost Method seems to be able to compete in terms of mass resolution. For the LFV process $Z \to \mu\tau_{had}$ at 13 TeV, using the Z-method, and taking twice the energy of the most energetic muon in the CM as the Z mass, seems to give the best resolution. This is slightly unexpected, as the XYZ-method is naively thought to give a more precise reconstruction of the CM. The difference could be due to the tendency of Z bosons to be produced with a largely longitudinal boost, making the transverse boost of the XYZ-method less relevant. It is also seen that poor E_T^{miss} resolution at low values deteriorates the performance of the XYZ-method.

The Boostmass was checked in various kinematic regions of the decay to get a better hold on the Boost Method Performance. Some method for background rejection of the $Z \to \mu\tau_{had}$ samples were also examined.

Going forward, it would be of interest to compare the Boost Method to the currently used mass discriminant for tau analyses in ATLAS, the MMC. A similar study should also be made using Higgs MC samples, as this is the process of interest in the analysis in the next chapter. The E_T^{miss} corrections considered in section 8.4 could be treated in a more rigorous way to improve the XYZ-Methods performance at low E_T^{miss}. However, the limited increase in the performance gained correcting by sight may suggest that such an approach is a dead end. It would also be of interest to get some handle on the uncertainty on the CM reconstruction. On how accurate is the method at actually finding the true CM of the Z.

9 $H \to \mu\tau$ analysis

This chapter aims to put a limit on the expected branching ratio of the process $H \to \mu\tau_{had}$. The analysis is modelled after the one made by the ATLAS collaboration in [53].

As the author will be continuing work on the $H \to \mu\tau_{had}$ analysis with the ATLAS collaboration after finishing this thesis, data will not be unblinded to calculate an observed branching ratio. This is done to avoid bias.

The final discriminant used is the Boostmass, twice the leading energy lepton in the Higgs CM, calculated using the XYZ-method described in chapter 7.

9.1 Data, Signal and Background Samples

9.1.1 Signal

At the time of writing, no official ATLAS production signal samples existed compatible with the software frameworks used in the analysis. The private productions mentioned in chapter 5 were therefore used as signal samples. The boostmass of the ggF and VBF samples are plotted in 9.1. In the previous chapter, the Z-method seemed to give the best resolution. From looking at the mass distribution in the Higgs signal samples, this does not seem to be the case. This is probably due to the fact that Z bosons are predominantly produced at large pseudorapidity at the LHC. Higgs bosons on the other hand, especially those produced through VBF, are much more transverse. This should weaken the performance of the Z-method. The final discriminant of this analysis is therefore selected to be the boostmass calculated using the XYZ-method. Note that the mass distributions in figure 9.1 are not well understood. As the author expected to have access to official signal samples for the analysis, the private productions have not been debugged.

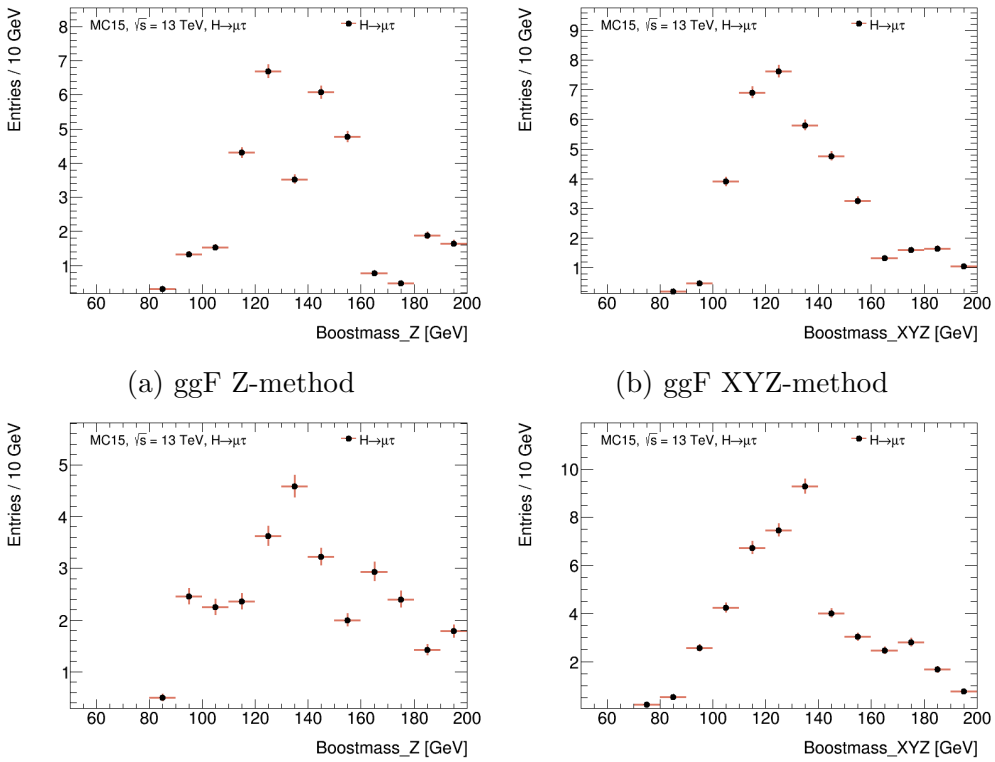

(a) ggF Z-method

(b) ggF XYZ-method

(c) VBF Z-method

(d) VBF XYZ-method

Figure 9.1: Boostmass of $H \to \mu\tau_{had}$ signal samples

9.1.2 Background

Samples for the following background categories were used for this analysis:

Z

The processes contributing to the Z boson background are $Z \to \tau\tau$ and $Z \to \mu\mu$. The event generator MadGraph, interfaced with Pythia8, was used to produce the samples.

W + jets

This background category includes the processes $W \to l\,\nu$, where l may be a tau, muon or electron. Event generators used to produce these samples were PowHeg and Pythia8.

Diboson

The diboson background category contains processes of the form $VV \to \mu\tau_{had} + X$, where V can be Z or W boson, and X are any uninteresting residuals in the decay. The processes considered in this category were $Z \to qq\,Z \to l^+l^-$ and $W \to qq\,Z \to l^+l^-$, both generated using Sherpa.

Top

The top background includes contributions from both single and pairs of top quarks. PowHeg and Pythia8 were used to generate the samples.

Higgs

The Higgs background is the process $H \to \tau\tau$. Higgs events are generated using PowHeg to simulate the Higgs production and Pythia8 to modell its decay.

Multijet

The QCD multijet category only background process not estimated using MC. A data driven method is used to estimate the multijet background, covered in section 9.3.

The MC samples contain pileup events corresponding to the detector conditions at the period of data taking. The beam energy in the MC is $\sqrt{s} = 13$ TeV.

9.1.3 Data

The data was collected in proton-proton collisions at the ATLAS detector in 2015 at $\sqrt{s} = 13$ TeV. The data is required to be part of a so-called Good Run List (GRL), which contain information about which data-taking periods are fit for physics analysis. The GRL used for this analysis is:

data15_13TeV.periodAllYear_DetStatus-v75-repro20-01_DQDefects-00-02-02_PHYS_StandardGRL_All_Good_25ns.xml

Using the ATLAS Luminocity Calculator [54], the total integrated luminosity collected in 2015 was found to be 3193±67 pb^{-1}. To avoid bias, the discriminant variable for the analysis, the Boostmass, is blinded in the Higgs mass region, between 100 and 140 GeV. Being blinded in this context means that events falling within the blinded region are not plotted. All other kinematic variables are unblinded.

9.2 Event Selection

The $H \to \mu\tau_{had}$ events are characterised by exactly one energetic muon as well as a hadronic tau jet of opposite sign. In addition there are some amount of E_T^{miss} present, all of which is due to the neutrino from the tau decay. E_T^{miss} should be closely aligned with the tau jet direction. A simple preselection is applied to the samples to clean out events that obviously don't satisfy these characteristics. The object definitions are the same as those made in the ALTAS search for $H \to \tau\tau$ events in [55].

Taus identified using the BDT method described in chapter 6 are required to have medium tightness. The tau jets are required to be one- or three-pronged, and to have a charge of +1 or -1. An electron veto rejects fake tau candidates from electrons. Muons are only required to satisfy loose identification criteria. The *isMuon* identification requirement is also applied. Minimum requirements for p_T and $|\eta|$ are set for both muons and taus. Muons can be softer, as they are easier to identify at low momentum than taus. Events are required to fire the trigger HLT_mu20_iloose_L1MU15. The preselection criteria is listed in table 9.1. There is no isolation requirement made for the muon.

Some kind of selection is also required to separate signal from background. Plotting the correlation between the transverse mass for tau + E_T^{miss} and muon + E_T^{miss} seemed promising for the Z samples in the previous chapter. Reproducing the plots for the most important processes of this analysis (fig 9.2) suggests the same. The Signal Region (SR) selection requirements are set to $M_T(\mu, E_T^{miss}) > 40$ GeV and $M_T(\tau, E_T^{miss}) < 30$ GeV.

The top quark (t) decay most often into a W boson and a bottom quark (b). b jets have a particular signature that distinguish them from other jets in the detector. Due to the relative high mass of the b compared to the lighter quark generations, b jets have high transverse momentum. The b also has a relatively long lifetime, giving it time to travel some distance before decaying. Jets displaying these characteristics are known as *b-tagged* jets; jets with a high probability of being b jets. As a means to separate the signal from t background, a so-called b veto is required for the SR. No b-tagged jets are selected.

Variable	Selection
Tau BDT ID	Medium
Tau p_T	>20 GeV
Tau Tracks	1 or 3
Tau η	<|2.47 |
Tau Charge	$\pm$ 1
Tau e Veto	Yes
Muon ID	Loose
Muon p_T	>10 GeV
Muon η	<|2.5 |
Trigger	HLT_mu20_iloose_L1MU15

Table 9.1: Preselection

In the previous chapter the Boost Method was shown to break down for separation in pseudorapidity between the tau and muon of over 2. Events are therefore required to have separation less than 2. It was shown in [53] that 99% of the signal survives this selection. The SR requirements are listed in table 9.2, along with the selections for the Control Regions (CRs), which will be covered in a later section.

	Signal Region	QCD CR	Z CR
$M_T(\mu E_T^{miss})$	$>$ 40 GeV	-	$<$ 30 GeV
$M_T(\tau E_T^{miss})$	$<$ 30 GeV	-	$>$ 20 GeV
$p_T(\tau)$	$>$ 40 GeV	-	-
$p_T(\mu)$	>40 GeV	-	-
$\Delta\eta(\mu,\tau)$	$<$ 2	$>$ 2	<2
b Veto	Yes	Yes	Yes

Table 9.2: Signal and control region definitions

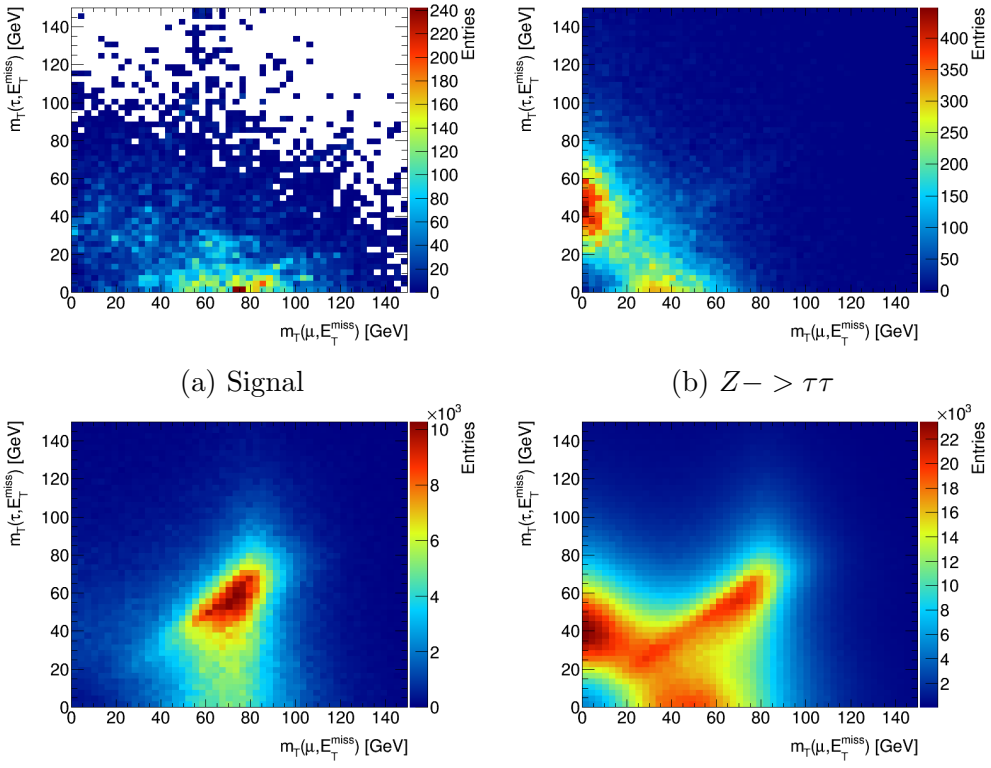

(a) Signal

(b) $Z->\tau\tau$

(c) W + jets

(d) Data

Figure 9.2: Correlation plots between $M_T(\mu, E_T^{miss})$ and $M_T(\tau, E_T^{miss}$ for the signal, data, $Z->\tau\tau$ background, and W + jets background.

9.2.1 Spin

In chapter 7 the possibility of separating Higgs from Z background using differences in the tau/muon energy spectra. This difference being due to the different spin of the Higgs and Z. In practice however, this does not seem feasible at this stage. Too much information is lost at low energies due to trigger and p_T requirements. The energy correlation plots from chapter 7 are recreated in figure 9.3 for the Higgs signal samples and the Z samples used in the previous chapter to illustrate this. The different structures for the spin 1 and 0 distributions are all but lost.

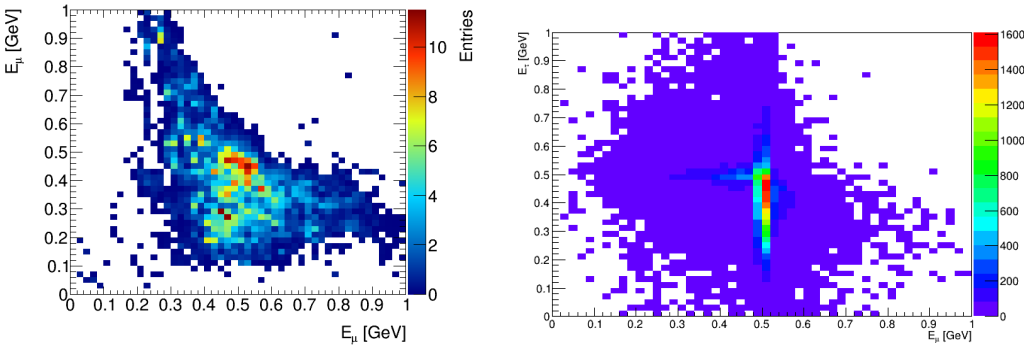

(a) $H \to \mu$ (Spin 0) (b) $Z \to \mu\tau$ (Spin 1)

Figure 9.3: Energy correlation plots for the tau and muon in different LFV samples. Energy plotten in the Higgs (Z) rest frame, calculated using the XYZ-Method, normalised to the Higgs (Z) mass.

9.3 Background Estimation

9.3.1 Background Categories

The $H \to \mu\tau_{had}$ background can be divided into the following categories:

- Events with true muon and hadronic tau signatures. The $Z \to \tau_{mu}\tau_{had}$ background dominates this category. τ_μ indicates a tau decaying leptonically, to a muon. Diboson ($VV \to \mu + \tau_{had} + X, \quad V = Z, W$), t and $H \to \tau_\mu\tau_{had}$ also contributes.

- Events where QCD jets fake a tau jet. This category is dominated by the W+jets and multijet background, with additional diboson and t contributions. The angular deviation between the tau and E_T^{miss} is larger for events with misidentified taus. This is exploited to suppress this background category.

- Events where a muon fake a tau jet. This category is mostly populated by $Z \to \mu\mu$ events.

The first and third of these background categories are strongly charge correlated: $N_{OS} >> N_{SS}$, where N_{OS} (N_{SS}) is the number of events in the category where the charge of the leptons have the same sign (SS) (opposite sign (OS)).

9.3.2 Background Modelling

The MC samples are all scaled to the integrated luminosity $\mathcal{L}_{int}$ in the data samples. This scale factor is calculated by:

$$MC_{scale} = \frac{\sigma \mathcal{L}_{int}}{N} \tag{9.1}$$

where σ and N is the cross section and total number of events in MC sample.

The background modelling is based on that performed in [55]. The QCD multijet background is estimated from data. It is assumed to have the same distribution for SS and OS events. This assumption was verified by [55]. The multijet modelling considers all SS data events part of the multijet background. Even though there are a lot more OS than SS events in the background, some of the data SS events will be due to other background processes. To account for this, same sign event are removed from the other background processes. The fraction of OS to SS events in the multijet background estimated by fitting background to data, and is measured to be:

$$r_{QCD} = \frac{N^{OS}_{QCD}}{N^{SS}_{QCD}} = 1.11 \pm 0.02 \tag{9.2}$$

which is consistent with the results found in [55]. The number of OS background events in each bin can be obtained according to the following formula:

$$\begin{aligned} N^{bgr}_{OS} &= r_{QCD} \times N^{data}_{SS} + N^{Z\to\tau\tau}_{OS-SS} + N^{Z\to\mu\mu}_{OS-SS} \\ &+ N^{W+jets}_{OS-SS} + N^{t/tt}_{OS-SS} + N^{VV}_{OS-SS} + N^{H\to\tau\tau}_{OS-SS} \end{aligned} \tag{9.3}$$

where $N^{bgr}_{OS-SS} = N^{bgr}_{OS} - r_{QCD} \times N^{bgr}_{SS}$ are the background processes with OS selection and SS subtracted.

The background was fitted to the variable $\Delta\eta_{\mu,\tau_{had}}$, the separation in pseudorapidity of the muon and tau jet. To test the multijet scaling, a control region, QCD CR in table 9.2, is defined. QCD CR flips the $\Delta\eta$ requirement of the SR, and rejects any b-tagged jets. In this region the background stems almost exclusively from multijet events. The scale factor r_{QCD} is determined by sight to be satisfactory.

The process $Z \to ee$ was considered as a background category, but it was found that no such events pass the preselection criteria.

After the initial background estimation, there still seems to be some mismodelling of the $Z \to \tau\tau$ background. This is then scaled to fit data in a dedicated Z CR. The selections for this CR are again selected by cutting on the transverse masses in figure 9.2. The fit in the CR can be seen in figure 9.6. The scale factor is calculated as $0.78 \pm 0.03_{\text{stat}} \pm 0.15_{syst}$.

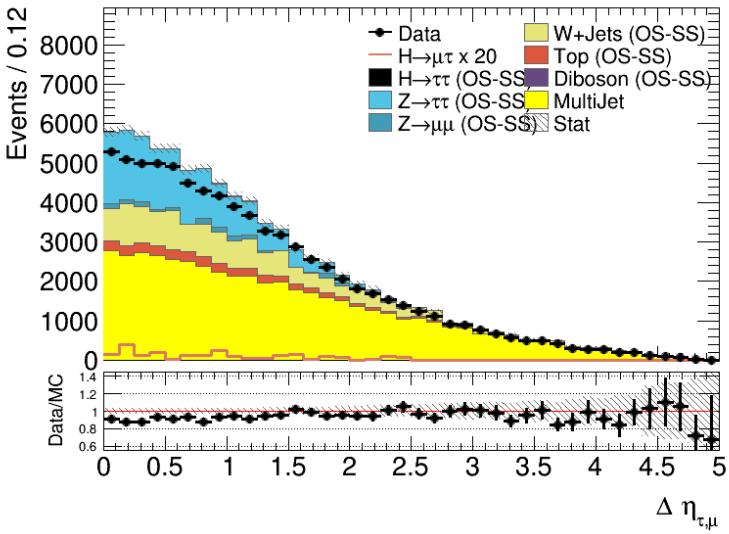

Figure 9.4: $\Delta\eta_{\mu,\tau_{had}}$ distribution after multijet background estimate. No scaling of Z. The $H\tau\mu$ branching ratio is set to 1% when plotting.

The background is now in good agreement with the data, as can be seen in figure 9.7.

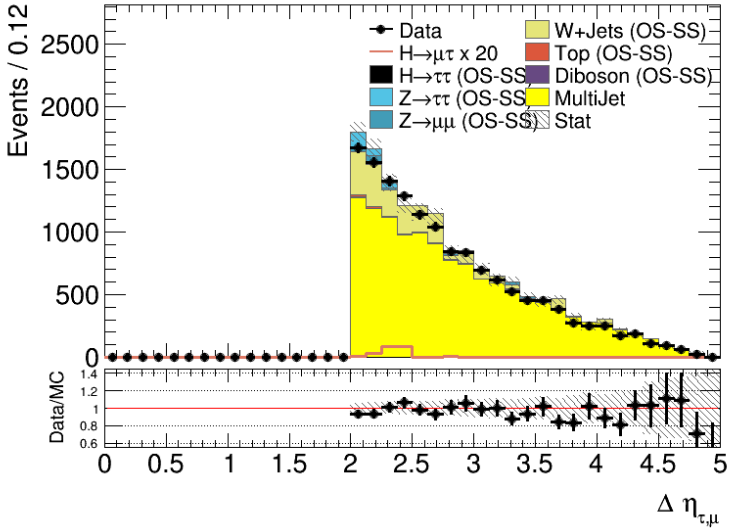

Figure 9.5: $\Delta\eta_{\mu,\tau_{had}}$ distribution in QCD CR

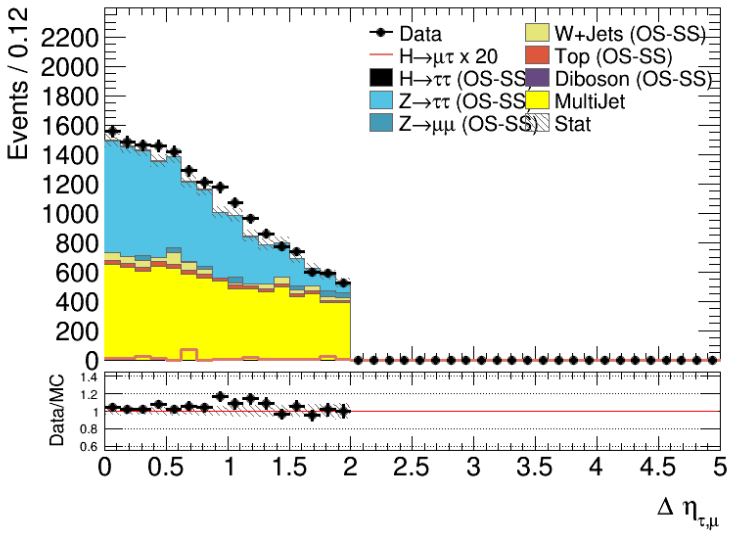

Figure 9.6: Background modelling in the Z enriched CR

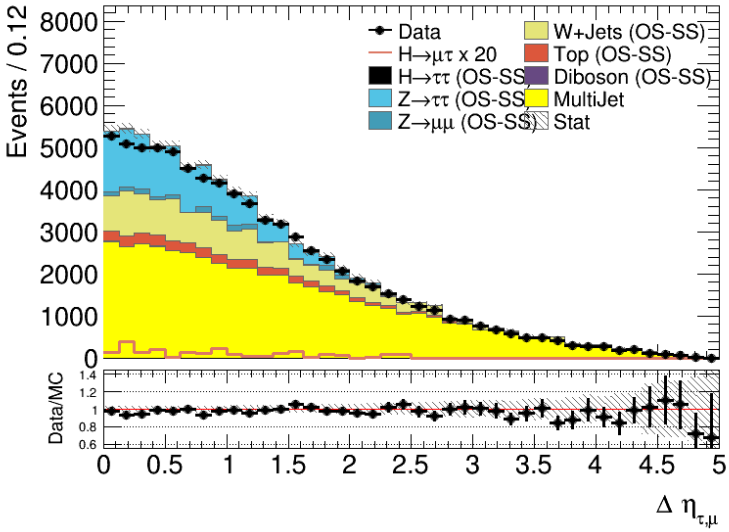

Figure 9.7: $\Delta\eta_{\mu,\tau_{had}}$ distribution after multijet and Z scale background modelling.

9.4 Optimisation

The SR should be defined such that it selects as many signal events as possible, while simultaneously discarding as many background events as possible. In addition to the selection made in section 9.2, tau and muon transverse momentum will be chosen in such a way as to achieve this. Other kinematic variables could be chosen for this optimisation, but they are all assumed to be correlated with the tau and muon p_T.

A metric is needed to determine what selections give the best background separation. For this we use the so called *significance*:

$$significance = \frac{S}{\sqrt{S+B}} \tag{9.4}$$

S (B) is the number of signal (background) events that survive the selection. Cuts on tau and muon transverse momentum were selected in such a way as to maximise the significance. Starting from the preselection p_T requirements and increasing the cuts in increments of 5 GeV up to a maximum of 50 GeV, the optimal cuts were found to be $p_T = 40$ GeV for both the tau and the muon. A table of the significance for all the cuts considered is found in table 9.3. The high p_T requirement for the muon should in principle do away with a lot of the $Z \to \tau\tau$ and $H \to \tau\tau$ background. The muons stemming from these background are produced in secondary decays, and are therefore expected to have softer momenta than the muons of the $H \to \mu\tau$ decay. The approach to optimisation employed here is called cut-based optimization. More advanced techniques can be applied. For example, some use selections made by BDTs, like the algorithm for tau identification mentioned in chapter 6.

Muon p_T \ Tau p_T	20	25	30	35	40	45	50
10	1.1	1.3	1.5	1.8	1.9	1.6	1.1
15	1.1	1.3	1.5	1.8	1.9	1.6	1.1
20	1.1	1.3	1.6	1.8	2.0	1.6	1.1
25	1.4	1.6	2.0	2.2	2.4	1.9	1.3
30	1.7	1.9	2.2	2.5	2.7	2.1	1.4
35	1.8	2.1	2.4	2.7	2.9	2.2	1.5
40	1.9	2.2	2.5	2.8	3.0	2.2	1.5
45	1.9	2.0	2.2	2.4	2.5	1.6	1.0
50	2.0	2.1	2.3	2.4	2.4	1.6	0.9

Table 9.3: Significance as a function of tau and muon p_T cuts. Momenta are in units of GeV.

Cut	Signal	Total Background
Preselection	11226.8±202	89548.1± 489
b-jet Veto	11049.8±201	83138.5 ± 483
Muon p_T	9237.9±184	27262.7 ± 300
Tau p_T	5279.0±142	8433.9 ± 104
$M_T(\tau, E_T^{miss})$	4159.1±128	5313.4 ± 65
$M_T(\mu, E_T^{miss})$	3632.9±119	4527.2 ± 57
$\Delta\eta(\mu, \tau)$	3632.9±119	4408.7 ± 53

Table 9.4: The events surviving the various selections in the signal region.

9.5 Systematic Uncertainty

Statistical uncertainty stems from randomness in the experiment and event counting. Take for instance the lifetime of a radioactive isotope. The time it takes for a nucleus to decay will not be the same each time, but scatter around the mean of a Poisson distribution.

Systematic uncertainty on the other hand, is due to the instruments or observers of an experiment. The uncertainty on the energy measured in a calorimeter shower is an example of a systematic uncertainty. Whereas statistical error can be reduced by taking more measurements, systematic error cannot.

A common way of calculating systematic uncertainties on a variable is to adjust its value up or down according to some predetermined values, and to measure its effect on the final discriminant. These variations then correspond to 1 sigma of systematic uncertainty.

The uncertainty in the integrated luminosity is ± 2.1 %. It is derived, following

a methodology similar to that detailed in [56], from a calibration of the luminosity scale using x-y beam-separation scans performed in August 2015. This mainly affects the normalization of signal and backgrounds. The systematic uncertainty of the Higgs production cross section and of the selection efficiency in the analysis are calculated and used in the next section.

The uncertainty in the background modelling, especially the normalization of the W+jets and $Z \to \tau\tau$ background categories, was found in **??** to be the greatest contributors to the systematic uncertainty of the analysis. The systematic uncertainty of the background scaling is taken as a 50% difference between the corrected and non-corrected cases. This has been adopted here to give the systematic uncertainty in the scaling of the $Z \to \tau\tau$ background.

Some of the other systematic efficiencies affecting the analysis are: Uncertainty in tau reconstruction efficiency, b-tagging efficiency, trigger uncertainty, the Tau Energy Scale (TES), and the Jet Energy Scale (JES). A more extensive treatment of the systematic uncertainty in the analysis beyond the scope of this thesis.

9.6 Expected Branching Ratio Limit

The branching fraction or ratio for a specific decay of a particle is defined as the probability for the particle, out of all possible decays, to decay into the wanted mode. This can be expressed as:

$$BR(i) = \frac{\Gamma_i}{\Gamma_{tot}} \tag{9.5}$$

where Γ_i is the width of the interesting process and Γ_{tot} is the total decay width of the particle, the space of all possible decays. If N_{tot} Higgs bosons are produced in the 2015 data considered for this analysis, the $H \to \mu\tau_{had}$ branching ratio is given as

$$BR(i) = \frac{N_{LFV}}{N_{tot}} \tag{9.6}$$

where N_{LFV} is the number of $H \to \mu\tau$ final states produced in the same period. The true number of these decays occuring in data is of course not known, and must be estimated. After selecting the SR a certain number of LFV *candidates* N_{cand} are chosen. N_{cand} will contain both signal and background events. The best estimate for N_{LFV} is

$$N_{LFV} = \frac{N_{cand} - B}{\epsilon} \tag{9.7}$$

ϵ is called the selection efficiency. It is a measure of how effective the analysis is at selecting signal events, and is defined as:

$$\epsilon = \frac{S}{S_0} \tag{9.8}$$

S_0 and S are the number of signal events before and after the event selection. A perfect selection is one in which $\epsilon = 1$. The error on the selection efficiency follow binomial statistics:

$$\sigma_\epsilon = \frac{1}{\sqrt{S_0}}\sqrt{\epsilon(1-\epsilon)} \tag{9.9}$$

The final expression for the estimated branching ratio now becomes:

$$BR_{LFV} = \frac{N_{cand} - B}{\epsilon N_{tot}} \tag{9.10}$$

The number of signal events in the final selection is simply the number of candidate events, minus the background events B, such that:

$$BR_{LFV} = \frac{S}{\epsilon N_{tot}} \tag{9.11}$$

To put a limit on the $H \to \mu\tau$ branching ratio an estimate for N_{tot} is needed. Using cross sections found by the LHC Higgs cross section working group [57], and the integrated luminosity previously calculated, the expected number of total Higgs can be calculated. The sections are listed in table 9.5. N_{tot} is given by $N_{tot} = \sigma_H \mathcal{L}_{int}$. [57] quotes several sources of uncertainty on the Higgs cross section, some of which are asymmetrical. To simplify calculations, the asymmetrical uncertainties are averaged. All sources of uncertainty are added in quadrature.

Process	Cross Section σ [pb]	Error [%]
ggF	44	± 9
VFB	3.8	± 3.0
VH	2.26	±2.77
TOTAL	50	±10

Table 9.5: Higgs cross sections at $\sqrt{s} = 13$ TeV for different production mechanisms.

It is customary to give the estimated branching ratio limit at a 95% confidence level confidence level (CL). This means that there is a 95% chance that the branching ratio is due to the signal being present, and a 5% chance that the background reproduces a signal by random chance. 95% CL equals about 1.96 sigma. The

observed branching ratio would have to have five sigma before a discovery could be claimed. A five sigma confidence level means that random fluctuations would recreate the signal only once in 3.5 million experiments.

The background is assumed to follow a Poisson distribution. The error on the number of background events is given by $\sqrt{B}$. To calculate the 95% CL on the branching ratio one need to find the number of candidate events needed to get 1.96 sigma away from the expected number of background events:

$$\frac{S}{\sqrt{S+B}} = 1.96 \tag{9.12}$$

Solving for S and substituting into 9.11, the upper limit on the branching ratio becomes:

$$BR_{LFV} \leq \frac{1.96\sqrt{S+B}}{\epsilon N_{tot}} \tag{9.13}$$

The error on the expected branching ratio is found by adding the errors that go into the formula in quadrature:

$$\left(\frac{\sigma_{BR}}{BR}\right)^2 = \left(\frac{\sigma_\epsilon}{\epsilon}\right)^2 + \left(\frac{\sigma_{\sigma_H}}{\sigma_H}\right)^2 + \left(\frac{\sigma_{\mathcal{L}}}{\mathcal{L}}\right)^2 \tag{9.14}$$

One of the problems of using this approach, based on event counting, is that it is very hard to include all the systematic uncertainties that need to be taken into account in a rigorous analysis.

9.7 Least Squares Method

The general procedure when setting a limit is to define two hypotheses, H_0 and H_1. H_0 is the background only hypothesis, while H_1, the signal-plus-background hypothesis, assumes the presence of some signal. When searching for BSM for example, H_0 is consistent with the SM, while H_1 includes some previously unknown process. One then defines a *test statistic*, which is a variable constructed from measurement. This variable is then used to test the agreement between hypotheses. For processes with large background, such as the one in this analysis, it is sufficient to use a so-called χ^2 test as the test-statistic. This can then be used to calculate the p-value of the hypothesis H. H is then discarded if the p-value falls below some predetermined value.

The choice of test test statistic varies with the measurement being taken. One possibility is to use a least squares method. For a set of measurements x_i, with

uncertainties σ_i, and an assumption on their distribution, μ_i, χ^2 is defined as:

$$\chi^2 = \sum_i^n \frac{(x_i - \mu_i)^2}{\sigma_i^2} \tag{9.15}$$

χ^2 helps determine the "goodness" of the fit μ_i to the points x_i.

The mass distribution for the final event selection can be seen in figure 9.8. Signal and background are binned in coarse 20 GeV bins due to the low number of events surviving the selection.

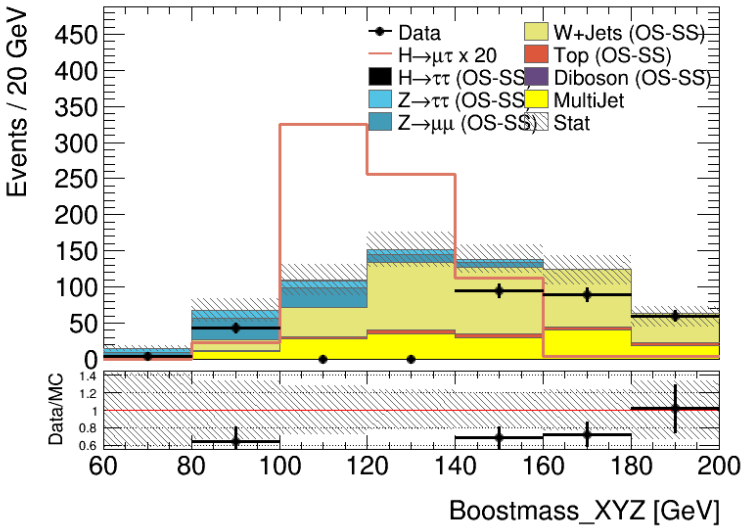

Figure 9.8: Boost Mass variable in signal region.

Scaling the number of signal event in each bin in the histogram using a scale factor c, the chi square test can be used to put an upper limit on the expected branching ratio. Taking the signal and background bin contents, S_i and B_i, the following χ^2

$$\chi^2 = \sum_i \frac{(cS_i)^2}{cS_i + B_i} \tag{9.16}$$

has a minimum value consistent with the background only hypothesis, $c = 0$. The upper limit on the branching ratio, at 95% CL is found by increasing c such that χ^2 is consistent with a 1.96 sigma discrepancy over the background. For a χ^2 distribution this number is 3.92 (2×1.96) [58]. If the branching ratio of $H \to \mu\tau$ is assumed to be one when normalising the signal samples to luminosity, the branching ratio limit is simply equal to the value of c corresponding to a χ^2

of 3.92. To calculate the correct Higgs cross section to scale the signal correctly the following formula is used:

$$\sigma_H = k \times \sigma_{prod} \times \epsilon_{GenFilt} \times BR(\tau_{had}) \tag{9.17}$$

The *k-factor*, which is different for ggF and VBF, is a constant aimed at correcting for differences in MC and data. σ_{prod} are the cross sections found in table 9.5. $\epsilon_{GenFilt}$ is the generator filter efficiency. At event generator level, some fraction of produced Higgs bosons are discarded due to unfavourable conditions, such as too high pseudorapidity. This needs to be accounted for. Finally, since the signal samples used only contain hadronically decaying taus, the cross section is multiplied with the branching ratio for such decays. The cross sections used to set the limit were $\sigma_{VBF} = 2.39$ and $\sigma_{ggF} = 41.6$. The resulting χ^2 can be seen in figure 9.9.

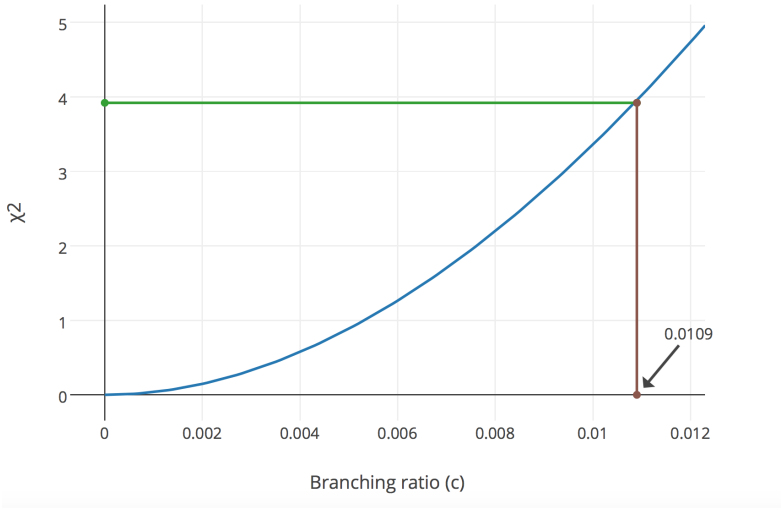

Figure 9.9: χ^2 distribution as a function of branching ratio.

9.8 Results

After scaling to luminosity, the number of LFV Higgs bosons in the signal sample is 29077. Combined with the number of signal events in the SR, 3632, this gives an efficiency of 0.125±0.002. The error is calculated using the binomial formula in equation 9.9. The total number of Higgs bosons produced in 2015 is estimated to be $N_{tot} = 159684$. This number must be adjusted somewhat. To adjust for the fact that this analysis is only sensitive to hadronic tau decays, N_{tot} is multiplied by the tau hadronic branching ratio. Event generator efficiencies must also be

accounted for. The number of Higgs boson produced in 2015, which could be feasibly detected in the analysis becomes $N'_{tot} = 46708$. Putting the number of signal and background events, as well as the adjusted number of produced Higgs bosons and the selection efficiency, into equation 9.13 yields the following upper limit on the branching ratio:

$$BR_{LFV} \leq 0.030 \pm 0.003 \tag{9.18}$$

The error is calculated using equation 9.14. Note that the systematic error on the generator filter efficiency is not known, and it is thus not included in the calculation. The error above is therefore a best-case scenario. The error on the hadronic tau branching ratio is assumed to be negligible.

The χ^2 test used in section 9.7 improved upon the simple method based solely on event counting. This method put the limit of the expected branching ratio to

$$BR_{LFV} \leq 0.011 \pm 0.001 \tag{9.19}$$

The branching ratio limits calculated here may seem a bit optimistic. This could be due to the missing treatment of systematic uncertainty. Its inclusion is expected to deteriorate the estimates.

10 Summary and Conclusion

This thesis has given a brief introduction to the SM, and to one of the signatures that might hint at BSM physics, LFV. Decays of the newly discovered Higgs particle has been singled out as particularly interesting channels for LFV searches. The LHC at CERN is the only particle accelerator in the world capable of producing the required number of Higgs particles to study these processes. A detailed explanation of one of the experiments at the LHC, the ATLAS detector, has been given.

Reconstructing the mass of a particle from its decay products and fitting some function to the resulting distribution is a common method in BSM seaches and in particle physics in general. Some common mass variables were outlined. A new mass variable, previously untested in LFV searches was introduced: The Boost Method. This method was tested on a simulated sample of $Z \to \mu\tau$ decays produced in $\sqrt{s} = 13TeV$ proton-proton collisions. It proved successful at reconstructing the Z rest frame, as well as the Z mass. The combination of the Boost Method with existing methods were discussed, as were corrections to combat deterioration of resolution at low E_T^{miss}. Two methods for LFV background separation were considered, and why it is of limited use to employ them both at the same time.

The expected limit on the branching ratio of the $H \to \mu\tau$ process was set using a simple event counting method to 0.030±0.003 at 95% CL. This limit was then improved upon using a least squares method, and a new expected limit set at 0.011±0.001. The background was modelled using both MC samples and a data driven method of estimating the QCD multijet background. The LFV signal was extracted from the background using a combination of cuts in the transverse mass og $\mu + E_T^{miss}$ and $\tau + E_T^{miss}$, as well as high transverse momentum cuts on both the muon and tau.

The analysis suffered from poor statistics in the signal MC samples. The fact that they were not validated and tested in any way is also problematic for the credibility of the results presented. The treatment of systematic uncertainties is also lacking.

Some improvements could be made to maximize the chance of observing LFV. The cut-based optimisation scheme is vary simple to use, but there are more powerful techniques available. A popular choice is to use BDT, like the algorithms for tau identification. The background modelling also has room for improvement.

The next step forward in the search for LFV in the Higgs sector is to unblind data to put a limit on the observed branching ratio. With new data being collected every day at the LHC, surely it is just a matter of time before a previously unknown process makes itself known.

Bibliography

[1] "The history of CERN." http://timeline.web.cern.ch/timelines/the-history-of-cern/overlay. Accessed: 22.01.2016.

[2] "CERN Annual report 2014," tech. rep., CERN, Geneva, 2015.

[3] T. Massam, T. Muller, B. Righini, M. Schneegans, and A. Zichichi, "Experimental observation of antideuteron production," *Il Nuovo Cimento A*, vol. 63, no. 1, pp. 10–14.

[4] "Antimatter." http://home.cern/topics/antimatter. Accessed: 24.01.2016.

[5] "The nobel prize in physics 1984." http://www.nobelprize.org/nobel_prizes/physics/laureates/1984/. Accessed: 24.01.2016.

[6] D. Wackeroth, "Cross section." High Energy Physics Made Painless. Fermilab Science Education Office. http://ed.fnal.gov/painless/pdfs/cross.pdf, 03 2009.

[7] E. M. Henley and A. Garcia, *Subatomic Physiscs*. World Scientific Publishing Co. Pte. Ltd., third edition ed., 2007.

[8] O. S. Brüning, P. Collier, P. Lebrun, S. Myers, R. Ostojic, J. Poole, and P. Proudlock, *LHC Design Report*. Geneva: CERN, 2004.

[9] Wikipedia, "Quadrupole magnet — Wikipedia, the free encyclopedia." https://en.wikipedia.org/wiki/Quadrupole_magnet, 2016. accessed 27.01.2016.

[10] "LHC, the guide." http://cds.cern.ch/record/1165534/files/CERN-Brochure-2009-003-Eng.pdf, February 2009.

[11] J. Pequenao, "Computer generated image of the whole ATLAS detector." https://cds.cern.ch/record/1095924, Mar 2008.

[12] Wikipedia, "Pseudorapidity — Wikipedia, the free encyclopedia." https://en.wikipedia.org/wiki/Pseudorapidity, 2016. accessed 31.01.2016.

[13] H. Spieler, *Semiconductor Detector Systems*. Series on Semiconductor Science and Technology, OUP Oxford, 2005.

[14] J. Pequenao, "Computer generated image of the ATLAS inner detector." `https://cds.cern.ch/record/1095926`, Mar 2008.

[15] C. Grupen and B. Shwartz, *Particle Detectors*. Cambridge Monographs on Particle Physics, Nuclear Physics and Cosmology, Cambridge University Press, 2008.

[16] J. Pequenao, "Computer generated image of the ATLAS Liquid Argon." `https://cds.cern.ch/record/1095928`, Mar 2008.

[17] J. Pequenao, "Computer Generated image of the ATLAS calorimeter." `https://cds.cern.ch/record/1095927`, Mar 2008.

[18] K. A. Olive *et al.*, "Review of Particle Physics," *Chin. Phys.*, vol. C38, p. 090001, 2014.

[19] J. Pequenao, "Computer generated image of the ATLAS Muons subsystem." `https://cds.cern.ch/record/1095929`, Mar 2008.

[20] G. Aad and Others, "The ATLAS Experiment at the CERN Large Hadron Collider," *J. Instrum.*, vol. 3, p. S08003. 437 p, 2008. Also published by CERN Geneva in 2010.

[21] *ATLAS level-1 trigger: Technical Design Report*. Technical Design Report ATLAS, Geneva: CERN, 1998.

[22] J. Pequenao and P. Schaffner, "An computer generated image representing how ATLAS detects particles." `https://cds.cern.ch/record/1505342`, Jan 2013.

[23] F. Mandl and G. Shaw, *Quantum Field Theory*. A Wiley-Interscience publication, John Wiley & Sons, 2010.

[24] P. A. M. Dirac, "The quantum theory of the emission and absorption of radiation," *Proceedings of the Royal Society of London A: Mathematical, Physical and Engineering Sciences*, vol. 114, no. 767, pp. 243–265, 1927.

[25] M. Peskin and D. Schroeder, *An Introduction to Quantum Field Theory*. Advanced book classics, Addison-Wesley Publishing Company, 1995.

[26] D. Hanneke, S. Fogwell Hoogerheide, and G. Gabrielse, "Cavity control of a single-electron quantum cyclotron: Measuring the electron magnetic moment," *Phys. Rev. A*, vol. 83, p. 052122, May 2011.

[27] J. Ellis, "Tikz-feynman: Feynman diagrams with tikz." arXiv:1601.05437, 2016.

[28] Wikipedia, "Higgs mechanism — wikipedia, the free encyclopedia," 2016. [accessed 27.05.2016].

[29] W. L. Freedman and M. S. Turner, "*Colloquium* : Measuring and understanding the universe," *Rev. Mod. Phys.*, vol. 75, pp. 1433–1447, Nov 2003.

[30] S. P. Martin, "A Supersymmetry primer," 1997. [Adv. Ser. Direct. High Energy Phys.18,1(1998)].

[31] F. Cei and D. Nicolò, "Lepton flavour violation experiments," *Advances in High Energy Physics*, 2014.

[32] S. L. Glashow, J. Iliopoulos, and L. Maiani, "Weak interactions with lepton-hadron symmetry," *Phys. Rev. D*, vol. 2, pp. 1285–1292, Oct 1970.

[33] A. M. Curiel, M. J. Herrero, W. Hollik, F. Merz, and S. Peñaranda, "Supersymmetric electroweak one-loop contributions to flavor-changing higgs-boson decays," *Phys. Rev. D*, vol. 69, p. 075009, Apr 2004.

[34] Y. Kuno, "Lepton flavor violation: Muon to electron conversion, COMET and PRISM/PRIME at J-PARC," *PoS*, vol. NUFACT08, p. 111, 2008.

[35] J. Adam, X. Bai, A. M. Baldini, E. Baracchini, C. Bemporad, G. Boca, P. W. Cattaneo, G. Cavoto, F. Cei, C. Cerri, A. de Bari, M. De Gerone, T. Doke, S. Dussoni, J. Egger, K. Fratini, Y. Fujii, L. Galli, G. Gallucci, F. Gatti, B. Golden, M. Grassi, D. N. Grigoriev, T. Haruyama, M. Hildebrandt, Y. Hisamatsu, F. Ignatov, T. Iwamoto, P.-R. Kettle, B. I. Khazin, O. Kiselev, A. Korenchenko, N. Kravchuk, A. Maki, S. Mihara, W. Molzon, T. Mori, D. Mzavia, H. Natori, D. Nicolò, H. Nishiguchi, Y. Nishimura, W. Ootani, M. Panareo, A. Papa, R. Pazzi, G. Piredda, A. Popov, F. Renga, S. Ritt, M. Rossella, R. Sawada, F. Sergiampietri, G. Signorelli, S. Suzuki, F. Tenchini, C. Topchyan, Y. Uchiyama, R. Valle, C. Voena, F. Xiao, S. Yamada, A. Yamamoto, S. Yamashita, Y. V. Yudin, and D. Zanello, "New limit on the lepton-flavor-violating decay $\mu^+ \to e^+\gamma$," *Phys. Rev. Lett.*, vol. 107, p. 171801, Oct 2011.

[36] M. Arana-Catania, E. Arganda, and M. J. Herrero, "Non-decoupling SUSY in LFV Higgs decays: a window to new physics at the LHC," *JHEP*, vol. 09, p. 160, 2013. [Erratum: JHEP10,192(2015)].

[37] H. Kamikado, T. Shindou, and E. Takasugi, "Froggatt-Nielsen hierarchy and the neutrino mass matrix," 2008.

[38] F. Feruglio, P. Paradisi, and A. Pattori, "Lepton flavour violation in composite higgs models," *The European Physical Journal C*, vol. 75, no. 12, pp. 1–26, 2015.

[39] E. O. Iltan and B. Korutlu, "Lepton flavor violating radion decays in the Randall-Sundrum scenario," *Phys. Scripta*, vol. 77, p. 065101, 2008.

[40] M. A. Dobbs *et al.*, "Les Houches guidebook to Monte Carlo generators for hadron collider physics," in *Physics at TeV colliders. Proceedings, Workshop, Les Houches, France, May 26-June 3, 2003*, pp. 411–459, 2004.

[41] S. Agostinelli *et al.*, "GEANT4: A Simulation toolkit," *Nucl. Instrum. Meth.*, vol. A506, pp. 250–303, 2003.

[42] *ATLAS detector and physics performance: Technical Design Report*. CERN, 1999.

[43] W. Lukas, "Fast Simulation for ATLAS: Atlfast-II and ISF," Tech. Rep. ATL-SOFT-PROC-2012-065, CERN, Geneva, Jun 2012.

[44] "Atlas computing work book." `https://twiki.cern.ch/twiki/bin/view/AtlasComputing/WorkBookFullChain`, 2007.

[45] C. O'Luanaigh, "The Worldwide LHC Computing Grid ." `http://cds.cern.ch/record/1997398`, Aug 2012.

[46] R. Brun and F. Rademakers, "{ROOT} — an object oriented data analysis framework," *Nuclear Instruments and Methods in Physics Research Section A: Accelerators, Spectrometers, Detectors and Associated Equipment*, vol. 389, no. 1–2, pp. 81 – 86, 1997. New Computing Techniques in Physics Research V.

[47] M. Cacciari, G. P. Salam, and G. Soyez, "The Anti-k(t) jet clustering algorithm," *JHEP*, vol. 04, p. 063, 2008.

[48] "Performance of the Reconstruction and Identification of Hadronic Tau Decays with ATLAS," Tech. Rep. ATLAS-CONF-2011-152, CERN, Geneva, Nov 2011.

[49] "Reconstruction, Energy Calibration, and Identification of Hadronically Decaying Tau Leptons," Tech. Rep. ATLAS-CONF-2011-077, CERN, Geneva, May 2011.

[50] B. P. Roe, H.-J. Yang, J. Zhu, Y. Liu, I. Stancu, and G. McGregor, "Boosted decision trees as an alternative to artificial neural networks for particle identification," 2004.

[51] A. Elagin, P. Murat, A. Pranko, and A. Safonov, "A new mass reconstruction technique for resonances decaying to di-tau." Nuclear Instruments and Methods in Physics Research Section A: Accelerators, Spectrometers, Detectors and Associated Equipment, Volume 654, Issue 1, 21 October 2011, Pages 481-489, 2010.

[52] P. L. Rosendahl, T. Burgess, and B. Stugu, "A Method to Estimate the Boson Mass and to Optimise Sensitivity to Helicity Correlations of tau+tau- Final States," *JHEP*, vol. 01, p. 043, 2012.

[53] G. Aad *et al.*, "Search for lepton-flavour-violating $h \to \mu\tau$ decays of the higgs boson with the atlas detector," *Journal of High Energy Physics*, vol. 2015, no. 11, pp. 1–33, 2015.

[54] "Atlas luminosity calculator." `https://atlas-lumicalc.cern.ch`. Accessed: 27.05.2016.

[55] G. Aad *et al.*, "Search for the Standard Model Higgs boson in the H to $\tau^+\tau^-$ decay mode in $\sqrt{s} = 7$ TeV pp collisions with ATLAS," *JHEP*, vol. 09, p. 070, 2012.

[56] A. Collaboration, "Improved luminosity determination in pp collisions at sqrt(s) = 7 tev using the atlas detector at the lhc," 2013.

[57] "SM higgs production cross sections at s = 13 TeV." `https://twiki.cern.ch/twiki/bin/view/LHCPhysics/CERNYellowReportPageAt13TeV`. Accessed: 29.05.2016.

[58] O. Behnke, K. Kröninger, G. schott, and T. Schörner-Sadenius, eds., *Data Analysis in High Energy Physics: A Practical Guide to Statistical Methods*. Wiley-VCH, 2013.

Acronyms and Abbreviations

b bottom quark. 88

t top quark. 88, 91

ALICE A Large Ion Collider Experiment. 9

ATLAS A Toroidal LHC AparatuS. 9

BDT Boosted Decision Tree. 55, 57–59, 88, 96, 105

BSM Beyond Standard Model. 1, 39, 40, 44, 105

CERN Conseil Européen pour la Recherche Nucléaire. 1, 3

CKM Cabbibo-Kobayashi-Maskawa. 32, 39

CL confidence level. 99, 105

CLFV Charged Lepton Flavour Violation. 39

CM center-of-mass. vii, 2, 5, 57, 61, 66, 70–72, 77, 85

CMS Compact Muon Solenoid. 9

CR Control Region. 89

CS Central Solenoid. 14

CSC cathode strip chamber. 15

DAOD Derived Analysis Object Data. 69

EF Event Filter. 16

EM electromagnetic. 14

eV electron volt. 21

FCNC Flavour Changing Neutral Current. 39

FWHM Full Width at Half Maximum. ix, 70–72, 77–79

G4 Geant4. 49, 69

ggF gluon-gluon fusion. 36, 51, 65, 85

GIM Glashow-Iliopoulos-Maiani. 39

GRL Good Run List. 87

HEPP High Energy Particle Physics. 4

HLT High Level Trigger. 17

ID Inner Detector. 9, 18

LAr liquid Argon. 14

LEP Large Electron-Positron Collider. 3, 5

LFV Lepton Flavour Violation. 1, 39–41, 43, 44, 69, 70, 105

LHC Large Hadron Collider. 1, 3, 5, 41, 69, 105

LINAC linear accelerator. 8

LVL1 Level-1 trigger. 16

LVL2 Level-2 trigger. 16

MC Monte Carlo. 47, 51, 69, 87

MDT monitored drift tube. 15

MMC Missing Mass Calculator. 64, 78, 84

MSSM Minimal Supersymmetric Standard Model. 42

OS opposite sign. 91, 92

PDF Parton Distribution Function. 48

PS Proton Synchrotron. 3

PSB Proton Synchrotron Booster. 8

QCD Quantum Chromodynamics. 29, 30, 80

QED Quantum Electrodynamics. 27, 29, 30

QFT Quantum Field Theory. 24

RF radiofrequency. 5, 8

ROIs Regions-of-Interest. 17

RPC resistive plate chamber. 15

SC Synchrocyclotron. 3

SCT Semiconductor Tracker. 11

SM Standard Model. 1, 4, 21, 22, 36–42, 45, 105

SPS Super Proton Synchrotron. 3

SR Signal Region. 88, 96

SS same sign. 91, 92

SUSY SUperSYmmetry. 38, 41, 43

TGC thin gap chamber. 16

TRT Transition Radiation Tracker. 11, 12

UiB the University of Bergen. xi

VBF vector boson fusion. 36, 51, 66, 85

VEV vacuum expectation value. 44

WIMP Weakly Interacting Massive Particle. 42

WWW World Wide Web. 4

xTauFW xTauFrameWork. 69